FABRICATION, CHARACTERISATION AND ANALYSIS OF CERIA THIN FILMS AND PATTERNED NANOSTRUCTURED DEPOSITS FOR ENHANCED SOLAR-DRIVEN THERMOCHEMICAL CONVERSION

BY

ASMAA ELTAYEB (B. ENG.)

A THESIS SUBMITTED IN PARTIAL FULFILMENT OF THE REQUIREMENT FOR THE DEGREE OF

DOCTOR OF PHILOSOPHY

PRIMARY SUPERVISOR: DR. STEPHEN DANIELS

SECONDARY SUPERVISOR: PROF. ENDA MCGLYNN

SCHOOL OF ELECTRONIC ENGINEERING

DUBLIN CITY UNIVERSITY

November 2016

Declaration

I hereby certify that this material, which I now submit for assessment on the programme of study leading to the award of Doctor of Philosophy is entirely my own work, and that I have exercised reasonable care to ensure that the work is original, and does not to the best of my knowledge breach any law of copyright, and has not been taken from the work of others save and to the extent that such work has been cited and acknowledged within the text of my work.

Signed: …… ID No.: ……
Asmaa Eltayeb

Date: ……

AFFECTIONATELY DEDICATED TO
THE LOVING MEMORY OF MY FATHER DR. ELTAYEB K. ELTAYEB
AND
MY BELOVED MOTHER NADIA AHMED

Acknowledgements

First and foremost, all praises to Allah for his continued blessing in my life; without it this thesis would not have been successful. Secondly, I would like to express my sincere and inestimable gratitude to my supervisors, Dr Stephen Daniels and Prof Enda McGlynn, for their endless support, guidance, patience, encouragement, care and affection throughout my studies. They have always made themselves available for help when I needed it and this thesis would have been far more challenging without their continuous direction. I would also like to sincerely thank Prof Patrick McNally for the valuable advice and comments provided during the initial course of my work and Dr Tony Cafolla for training and allowing me to use his AFM equipment. I am immensely grateful to the selfless effort and time given by Dr Rajani K. Vijayaraghavan and her constant help and valuable advice throughout my PhD journey. I am also very grateful to Billy Roarty for his continued technical and moral support for the duration of my PhD. He was always available to sort out problems with both the cryo-pump on the sputtering chamber and the XRD system. I would also like to acknowledge Gerard, Robert, Michael and Liam for their technical help at various stages of my work. Thanks to Dr Anthony McCoy for doing the XPS experiments, Dr Anita Venkatanarayanan for helping with the CV experimental set-up, Dr Joseph Cullen for carrying-out the PL measurements, Dr Daragh Byrne for helping with the wet chemical deposition and other chemical related issues and Dr Seamus Garry for helping with the nanospheres lithography. To Dr Aidan Cowley for training me to use the plasma system to etch the nanospheres, Dr Ciaran Gray for helping with ZnO Chemical bath deposition and Dr Jithin Cherunilam. Sincere thanks to Dr Aleksey Yaremchenko and Dr Rajesh Surendran for

helping with the TGA, thank you. I would also like to acknowledge Ms JoAnna Thompson for proof reading my thesis. Heartfelt gratitude to all my friends in DCU and abroad; your encouragement and friendship have been very meaningful to me, especially during this pivotal point in my life. To my husband, Loai, your support throughout all the difficult situations and your constructive advice has truly helped to enhance my work.

Acknowledgements are also due to the postgraduate funding from INSPIRE, supported under the framework of the Irish government's PRTLI Cycle 5, National Development Plan 2007–2013 with the assistance of the European Regional Development Fund, for funding this PhD work. I would also like to acknowledge Prof Liam Barry for assisting me with conference travel and other funding queries. Finally, but most importantly, I would like to express my thankfulness and appreciation to my great (late) father, mother and siblings: Ali, Mohammed and Khalaf. Their immeasurable love, support and prayer have moulded me into the person I am today.

List of Publications, Conference Contributions & Courses Undertaken

Publications:

The following publications stem from this research. All publications are full length papers and each describes a particular aspect of this research.

1) Eltayeb, A., Vijayaraghavan, R. K., McCoy, A., Venkatanarayanan, A., Yaremchenko, A. A., Surendran, R., McGlynn, E. and Daniels S. Control and enhancement of the oxygen storage capacity of ceria films by variation of the deposition gas atmosphere during pulsed DC magnetron sputtering. Accepted for journal publication with Journal of Power Sources 279 (2015) 94 - 99.

2) Eltayeb, A., Vijayaraghavan, R. K., McCoy, A. P., Cullen, J., Daniels, S. and McGlynn, E. Control of crystal structure, morphology and optical properties of ceria films by post deposition annealing treatments. Accepted for journal publication with Thin Solid Films 603 (2016) 363 - 370.

3) Eltayeb, A., Daniels, S. and McGlynn, E. Tailoring enhanced optical properties of ZnO and CeO_2-coated ZnO nanostructures via spherical nanoshells growth on a polystyrene template. Manuscript submitted for journal publication in Scientific Reports (August 2016).

Conference Contributions:

The following conference contributions stem from this research.

1) Eltayeb, A., Vijayaraghavan, R. K., McGlynn, E. and Daniels, S. Investigation of the structural, morphological, optical and redox properties of cerium oxide nanostructure deposited using pulsed DC magnetron sputtering. European Materials Research Society (EMRS 2015) Conference. Lille, France.

2) Eltayeb, A., Byrne, D.,McGlynn, E. and Daniels, S. Preparation of nanostructured spherical ceria nanoshells by wet chemical deposition on a polystyrene template. European Materials Research Society (E-MRS 2015) Conference. Lille, France.

3) Eltayeb, A., Rajani, K. V., McCoy, A., Venkatanarayanan, A., Byrne, D., McGlynn, E. and Daniels, S. Enhanced two-step solar-driven thermochemical cycling using low-quality whispering gallery modes in ceria spherical nanoshells. Conference of Photonics Ireland 2013. Belfast, United Kingdom.

4) Eltayeb, A. Rajani, K. V., McGlynn, E. and Daniels, S. Enhanced two-step solar-driven thermochemical cycling using low-quality whispering gallery modes in ceria spherical nanoshells. China- Ireland International Conference on Information and Communications Technologies (CIICT 2012), Dublin, Ireland.

5) Eltayeb, A., Rajani, K. V., McGlynn, E. and Daniels, S. Growth and characterisation of cerium oxide thin films by pulsed DC magnetron sputtering: influence of oxygen partial pressure and post deposition annealing. Material research society (MRS 2012) symposium. Boston, Massachusetts, United States of America.

Courses Undertaken:

The following courses were completed and incorporated in the research and writing of this project.

1) Introduction to Nanoscience course, PH5094, October 2011, Materials and Surface Science Institute (MSSI), University of Limerick, Limerick, Ireland. (5 Credits)

2) Entrepreneurship for Engineers course, EE507, January 2012, School of Electronic Engineering, Dublin City University, Dublin, Ireland. (7.5 Credits)

3) Characterisation Technology for Nanomaterials course, EE550, May 2012, School of Electronic Engineering, Dublin City University, Dublin, Ireland. (7.5 Credits)

4) Research Practice & Methodology course, MM503, January 2013, School of Mechanical & Manufacturing Engineering, Dublin City University, Dublin, Ireland. (7.5 Credits)

5) LabVIEW, Data Acquisition, Analysis and Control course, MM600, April 2013, School of Mechanical & Manufacturing Engineering, Dublin City University, Dublin, Ireland. (7.5 Credits)

6) Surface Engineering & Tribology course, MM530, May 2013, School of Mechanical & Manufacturing Engineering, Dublin City University, Dublin, Ireland. (7.5 Credits – Attendance only)

7) Writing Science & Engineering, PH6022, April 2013, Department of Physics and Energy, University of Limerick, Ireland. (5 Credits – Attendance only)

Table of Contents

Declaration **II**

Dedications **III**

Acknowledgments **IV**

List of Publications, Conferences Contributions & Courses Undertaken **VI**

List of Figures **XIV**

List of Tables **XXI**

Acronyms **XXII**

Chemicals **XXIII**

Abstract **XXVI**

CHAPTER 1 – INTRODUCTION **1**

1.1 INTRODUCTION …… 1

1.2 SOLAR ENERGY & FUEL GENERATION …….…….... 2

1.3 TWO-STEP THERMOCHEMICAL CYLCE ……. 7

1.4 REDOX PAIR METAL OXIDES ……. 9

1.5 CERIA ……. 11
1.5.1 CERIA NANOPARTICLES ……..... 12
1.5.2 CERIA OXYGEN STORAGE CAPACITY..…… 13
1.5.3 CERIA IN THERMOCHEMICAL CYCLES ……... 15
1.6 WHISPERING GALLERY MODES ……. 16
1.7 THESIS SCIENTIFIC QUESTIONS …… 19
1.8 THESIS OVERVIEW …….. 20

CHAPTER 2 – GROWTH AND CHARACTERISATION TECHNIQUES **23**

2.1 INTRODUCTION ….…… 23
2.2 FILM GROWTH TECHNIQUES …….. 24
2.2.1 SPUTTERING ……. 24
2.2.1.1 MAGNETRON SPUTTERING …….. 25
2.2.1.2 PULSED DC MAGNETRON SPUTTERING ……... 27
2.2.2 SPIN COATING DEPOSITION ……..…….. 31
2.3 CHARACTERISATION TECHNIQUES ……. 32
2.3.1 X-RAY DIFFRACTION ……. 32
2.3.2 SCANNING ELECTRON MICROSCOPY ……..…… 34
2.3.3 ENERGY DISPERSIVE X-RAY SPECTROSCOPY ……..…… 37
2.3.4 SPECTROSCOPIC ELLIPSOMETRY ……..…….. 38
2.3.5 ATOMIC FORCE MICROSCOPY ……..……... 40
2.3.6 X-RAY PHOTOELECTRON SPECTRSCOPY ……..……... 41
2.3.7 SECONDARY ION MASS SPECTROMETRY ……..…….. 43
2.3.8 THERMOGRAVIMETRIC ANALYSIS ……....…….. 44
2.3.9 ELECTOCHEMICAL CYCLIC VOLTAMMETRY ……..……... 45
2.3.10 ULTRAVIOLET-VISIBLE SPECTRSCOPY ……..…… 47
2.3.11 PHOTOLUMINESCENCE ……..……... 48

CHAPTER 3 – MAGNETRON SPUTTERING GROWTH AND CHARACTERISATION **50**

3.1 INTRODUCTION …. 50

3.2 EXPERIMENTAL METHODS …….. 53

3.3 RESULTS AND DISCUSSION …… 54

3.3.1 STRUCTURAL & MORPHOLOGICAL STUDIES ……..……. 55

3.3.2 FILM COMPOSITION – SIMS ……...……. 58

3.3.3 CHEMICAL ANALYSIS – XPS ……...……. 59

3.3.4 ELECTROCHEMISTRY –CV …… 61

3.3.5 OSC MEASUREMENTS – TGA …….……... 64

3.4 CONCLUSIONS …… 65

CHAPTER 4 – FILM ANNEALING TREATMENTS AND CHARACTERISATION **67**

4.1 INTRODUCTION …….. 67

4.2 EXPERIMENTAL METHODS …….…… 69

4.2.1 ANNEALING …….. 70

4.2.2 CHARACTERISATION ….…… 70

4.3 RESULTS AND DISCUSSION ……..……... 71

4.3.1 STRUCTURE AND MORPHOLOGY ……..… 72

4.3.2 CHEMICAL COMPOSITION –XPS ……..… 81

4.3.3 UV-VIS ABSORPTION AND BANDGAP ENERGY ……..… 85

4.3.4 LOW-TEMPERATURE PHOTOLUMINESCENCE ……... 86

4.4 CONCLUSIONS …… 87

CHAPTER 5 – NANOSPHERE LITHOGRAPHY OF CERIA NANOSTRUCTURES **89**

5.1 INTRODUCTION ……... 89

5.2 GENERATING NANOSPHERES MONOLAYER ……..... 91

5.3 NANOSPHERE OXYGEN PLASMA ETCH ……..… 92

5.4 STRUCTURE FORMATION …… 93

5.5 RESULTS AND DISCUSSION ……..... 97

5.5.1 STRUCTRAL OBSERVATIONS ……..……... 98

5.5.2 CHEMICAL COMPOSITION ……..……... 99

5.5.3 UV-VIS ABSORPTION …...……..... 101

5.6 MATHEMATICAL MODELING ……... 104

5.6.1 MODEL 1: DOME-SHAPED STRUCTURES …… 104

5.6.2 MODEL 2: SPHERICAL NANOSHELL STRUCTURES ……. 106

5.7 CONCLUSIONS ……... 108

CHAPTER 6 – ENHANCED OPTICAL ABSORPTION VIA SPHERICAL NANOSHELLS **109**

6.1 INTRODUCTION …… 109

6.2 FILM SYNTHESIS …… 112

6.3 PATTERNED NANOSHELL SYNTHESIS …...…… 114

6.4 RESULTS AND DISCUSSION ..…… 117

6.4.1 XRD OBSERVATIONS ……..... 117

6.4.2 SEM OBSERVATIONS …… 121

6.4.3 CHEMICAL COMPOSITION …… 122

6.4.4 UV-VIS ABSORPTION AND BANDGAP ENERGY ……..…. 125

6.4.4.1 DIRECTIONALITY STUDIES …… 130

6.4.5 PHOTOLUMINESCENCE ……. 131

6.5 CONCLUSIONS ……... 133

CHAPTER 7 – CERIA WET CHEMICAL GROWTH AND CHARACTERISATION **135**

7.1 INTRODUCTION …… 135

7.2 SUBSTRATE PREPARATION …… 136

7.3 CHEMICAL SOLUTION PREPARATION …….. 137

7.4 DEPOSITION PROCESS …… 137

7.5 RESULTS AND DISCUSSION ……... 139

7.5.1 STRUCTURAL STUDIES ……..... 142

7.5.2 COMPOSITION ANALYSIS …….. 144

7.5.3 OPTICAL PROPERTIES …… 147

7.6 CONCLUSIONS ……... 150

CHAPTER 8 – CONCLUSIONS AND FUTURE WORK **152**

8.1 CONCLUSIONS ……... 152

8.2 FUTURE WORK ……... 156

Appendix …….. 158

A.1 ZnO Chemical Analysis – XPS ……... 158

References …… 161

List of Figures

Figure 1.1: A schematic diagram of the earth's solar energy distribution ….. 3
Figure 1.2: The five thermochemical routes for solar hydrogen production [14] …….. 7
Figure 1.3: Crystal structure of the cubic fluorite lattice of CeO_2. Here Ce and O atoms are shown by grey and white circles, respectively [2] …….. 11
Figure 1.4: Schematic electronic structures of (a) stoichiometric CeO_2, (b) partially reduced $CeO_{2-\delta}$ and (c) Ce_2O_3. Filled bands are drawn as filled boxes and empty bands are drawn as empty boxes [46] ……. 14
Figure 1.5: Formation of an OVD in CeO_2. OVD formation follows the basic step of O diffusion through the lattice. When an O encounters another O atom, a bond is formed and the O_2 molecule is able to diffuse away from the surface of the crystal. Each O atom that diffuses away from the surface leaves behind two electrons to be shared between three cerium atoms. This results in a partially reduced cerium atom to a valency between 3+ and 4+ states. [52] …… 15
Figure 1.6: Photograph of the reticulated porous ceramic made of ceria. Inset: SEM micrograph of a break plane of its struts. [63] …….. 18
Figure 1.7: Nanocrystalline Si spherical nanoshell morphology and optical absorption. (a) SEM cross-sectional image of a monolayer of Si spherical nanoshells on a quartz substrate. Scale bar equals 300nm. (b) Electron diffraction pattern showing the nanocrystalline nature of Si nanoshells. (c) Integrating sphere measurement of absorption spectra under normal incidence for the thin film sample (black line) and nanoshell sample (red line). (d) Integrated absorption over the global solar spectrum (ASTM G173-03) for different incidence angles relative to normal incidence. [59] …….. 19
Figure 2.1: Schematic of the magnetron cathode and the sputtering deposition process ……. 26

Figure 2.2: Photograph of the sputtering system used for the experiment: A) Magnetron, B) Sputtering chamber, C) Loading chamber and, D) Transfer valve ……. 29
Figure 2.3: Photograph of the asymmetric bipolar pulsed power supply (ENI RPG-100) used for the deposition …… 29
Figure 2.4: Schematic of the asymmetric bipolar pulsed DC signal used for the deposition. The deposition by sputtering of the target on the substrates takes place during the pulse-on time of the pulse …… 30
Figure 2.5: Schematic of the chemical solution spin coating process ……. 31
Figure 2.6: Illustration of Bragg's law. The figure indicates the conditions for the occurrence of Bragg diffraction. Planes of atoms are indicated using the black solid lines …….. 33
Figure 2.7: Photograph of Bruker AXS Advance D8 XRD system …….. 34
Figure 2.8: Schematic of a SEM system. The electron gun and the lensing system to focus the electron beam on to the sample surface are illustrated 36
Figure 2.9: Illustration of the different signals generated by the electron beam-specimen interaction in SEM and the regions from which the signals can be detected [74] …… 36
Figure 2.10: Photograph of the Zeiss EVO LS-15 SEM system …… 37
Figure 2.11: Schematic of the spectroscopic ellipsometry system ……... 39
Figure 2.12: (a) Schematic representation of a typical AFM instrument, (b) a schematic representation of the effect of bending the cantilever on the laser beam path during tapping mode oscillations [76] …… 41
Figure 2.13: Photograph of dedicated three chambered XPS system ……. 42
Figure 2.14: Schematic of the SIMS analysis …….. 43
Figure 2.15: The Millbrook MiniSIMS Alpha system ……... 44
Figure 2.16: Scan rate and rate constant dependence of the I-V curves [81] . 46
Figure 2.17: Schematic of the cyclic voltammetry three-electrode cell configuration ……... 47
Figure 2.18: Photograph of the Perkin Elmer Lambda 40 UV-Vis spectrometer …… 48
Figure 2.19: Schematic of the PL experimental set-up …….. 49
Figure 3.1: XRD pattern of CeO_2 thin films deposited on Si (100) substrates by PDCMS under two different gas conditions, Ar (blue) and Ar/O_2 (red) ….. 56
Figure 3.2: 2 ×2 μm^2 top and 3D view AFM images of CeO_2 thin films sputtered in a) pure Ar and b) an Ar/O_2 gas mixture …….. 57

Figure 3.3: SIMS spectra in the range from 100 to 200 amu/e measured from CeO_2 thin films sputtered in a) Ar and b) Ar/O_2 …….. 59
Figure 3.4: Ce 3d core level photoemission spectra from CeO_2 thin films sputtered in a) Ar and b) Ar/O_2 gas atmospheres …… 60
Figure 3.5: O 1s core level photoemission spectra from CeO_2 thin films sputtered in a) Ar and b) Ar/O_2 gas atmospheres. The component labelled '(i)' is attributed to O^{2-} ions. The component labelled '(ii)' is assigned to $O^{\delta-}$ species or OH groups …… 61
Figure 3.6: CV scan of 50 nm thick nanostructured CeO_2 films deposited by PDCMS technique in a) a pure Ar environment and in b) an Ar/O_2 mixture environment in anhydrous DMF solution with 1 M LiClO4 as supporting electrolyte and a scan rate of 0.1 Vs^{-1} ……... 62
Figure 3.7: Relationship between capacitive current (i_a) and scan rate for CeO_2 films deposited in a) pure Ar and b) Ar/O_2 ambients ……... 63
Figure 3.8: TGA curves of CeO_2 films deposited in a pure Ar ambient and in Ar/O_2 mixed ambient, on reduction in 10%H_2-N_2 flow at 600°C …….. 65
Figure 4.1: XRD θ-2θ patterns of (a) the CeO_2 sputtering target and (b) the CeO_2 films (i) as-deposited and post-deposition annealed at temperatures of (ii) 500 °C, (iii) 800 °C and (iv) 1000 °C in an air ambient ……... 75
Figure 4.2: Rietveld analysis of three diffraction patterns of CeO_2 annealed samples. a) 500 ^oC anneal, b) 800 ^oC anneal and c) 1000 ^oC anneal. The refinement of data is obtained using three different phases (CeO_2, Ce_2O_3; order corresponds to indicated Bragg peak positions from first to second line and we note that no evidence of the CeO phase is seen) ……. 76
Figure 4.3: XRD patterns of nanostructured CeO_2 thin films grown on Si(100) substrates. The films are annealed at 800 °C, with various OFRs (a) 0 sccm, (b) 1 sccm, (c) 20 sccm, (d) 30 sccm, (e) 40 sccm and (f) 50 sccm. The AFR is kept constant at 50 sccm for all samples ……. 77
Figure 4.4: Influence of OFR during post-deposition annealing on the out of plane coherence length of the CeO_2 films ……... 78
Figure 4.5: 2 x 2 μm^2 plan-view AFM images of nanostructured CeO_2 films post-deposition annealed at 800 °C in an OFR of (a) 0 sccm, (b) 20 sccm, (c) 30 sccm and (d) 50 sccm. The AFR is kept constant at 50 sccm for all samples …… 80
Figure 4.6: XPS Ce3d core level spectra for a) as-deposited CeO_2 and 800 °C annealed CeO_2 samples with OFRs of b) 0 sccm and c) 50 sccm …… 82
Figure 4.7: O 1s XPS spectra of CeO_2 samples: a) as-deposited, and annealed at 800 °C in b) an OFR of 0 sccm and c) an OFR of 50 sccm ……. 83

Figure 4.8: O 1s XPS spectra of 800 °C thermal annealed CeO_2 sample (the data shown is from a sample annealed at an OFR value of 50 sccm, but essentially the same spectra and behaviour are seen regardless of OFR value for all samples annealed at 800 °C), normal emission and off-normal emission …… 84
Figure 4.9: UV-Vis absorption spectra of CeO_2 sputtered films, as-deposited and post-deposition annealed at temperatures of 500 °C, 800 °C and 1000 °C in an air ambient …… 85
Figure 4.10: Tauc plot of $(\alpha h\nu)^2$ vs. hv for nanostructured CeO_2 sputtered films, as-deposited and post-deposition annealed at temperatures of 500 °C, 800 °C and 1000 °C in an air ambient ……... 86
Figure 4.11: LPL spectra of a nanocrystalline CeO_2 thin film annealed at 800 ^oC at an OFR of 50 sccm, measured at 10, 15, 18 and 22 Kelvin (K) ……... 87
Figure 5.1: A schematic of the equipment and procedures used to obtain nanosphere monolayers on CeO_2 thin films deposited on Si(100), glass and quartz substrates; a) the nanosphere solution is applied to the glass slide just above the DI water surface, b) a self-assembled nanosphere monolayer is created and then lifted off the DI water surface and onto the substrate, c) this results in a nanosphere monolayer deposited on the substrate sample [76] …… 92
Figure 5.2: a) A graph of PS nanosphere diameters versus O_2 etch time and SEM images of PS nanosphere monolayer samples etched for different times; b) unetched, c) 60s exposure and d) 120s exposure …….. 94
Figure 5.3: SEM images of the PS spheres monolayer deposited on a Si (100) substrate a) before and b) after O_2 plasma treatment. The spheres diameter reduced from ca. 600 nm to 520 nm when exposed to O_2 plasma for 25 seconds …… 95
Figure 5.4: 3D images of a) O_2 plasma treated PS nanosphere monolayer deposited on a substrate and b) CeO_2 coated PS nanospheres ……... 96
Figure 5.5: SEM images of the dome-shaped CeO_2 nanostructures after the removal of the PS nanospheres (i.e. annealed at 500 °C for 30 minutes in air). The SEM images show a) plan view, b) 45°view, c) and d) 60° view of the dome-shaped structure with a clear evidence of the voids in image d ……. 97
Figure 5.6: XRD θ-2θ pattern (locked coupled) of CeO_2 film (top) and dome-shaped (bottom) nanostructures grown on Si (100) substrates, as-deposited and annealed at 500 °C for 30 minutes. XRD peak located at ~ 28.5° corresponds to the predominant CeO_2 (111) peak …… 99

Figure 5.7: EDX spectrum for the CeO_2 dome-shaped before (top) and after (bottom) the removal of the PS nanospheres ……... 100
Figure 5.8: Room temperature UV-Vis absorption spectra of CeO_2 film, CeO_2 coated PS nanospheres and CeO_2 dome-shaped structures samples, under normal incidence, with a clear indication of absorption increase (ΔA) as a result of the dome-shaped structure geometry ……... 102
Figure 5.9: Integrated absorption for different incidence angles relative to the normal incidence for the CeO_2 dome-shaped structures sample deposited on quartz substrate …… 103
Figure 5.10: SEM image of dome-shaped metal-oxide nanostructures …… 106
Figure 5.11: SEM image of hollow spherical metal-oxide nanostructures [59] ……... 107
Figure 5.12: Representation of the distance (d) separating two adjacent spheres ……... 107
Figure 6.1: Morphologies used in this study: a) CeO_2, b) ZnO and c) CeO_2-coated ZnO films, and; d) ZnO and e) CeO_2-coated ZnO spherical nanoshell structures. All samples were deposited on both Si (100) and quartz substrates and have the same physical thickness of 120 ± 10 nm ……... 112
Figure 6.2: Flow chart of the overall process in the fabrication of ZnO, CeO_2, and CeO_2-coated ZnO films …… 114
Figure 6.3: Flow chart of the overall process in the fabrication of ZnO and CeO_2-coated ZnO spherical nanoshell structures by zinc acetate drop coating and PDCMS deposition methods on bare substrates ……. 116
Figure 6.4: 3D images of a) a monolayer of the PS spheres deposited on the substrate surface, b) O_2 plasma etched PS spheres, c) ZnO spherical nanoshells and d) CeO_2-coated ZnO spherical nanoshells …… 116
Figure 6.5: XRD $\theta/2\theta$ scan (locked coupled) of Z_F (top) and Z_NS (bottom) structures grown on Si (100) substrates. The samples are as-deposited and annealed at 500 °C and 800 °C for 30 minutes. The dominant XRD peaks located at 34.4° correspond to the ZnO (002) ……... 118
Figure 6.6: XRD $\theta/2\theta$ scan (locked coupled) of C_Z_F (top) and C_Z_NS (bottom) structures grown on Si (100) substrates. The samples are a) as-deposited and annealed at b) 500 °C and c) 800 °C for 30 minutes. The dominant XRD peaks located at 34.4° and 28.5° correspond to the ZnO (002) and CeO_2 (111), respectively ……... 120
Figure 6.7: Plan view SEM image of the spherical ZnO nanoshells before complete removal of PS nanospheres i.e. simply heated at 350 °C for 30 minutes to decompose the zinc acetate into zinc oxide …….. 122

Figure 6.8: SEM images of the spherical nanoshell structures after the removal of the PS spheres (i.e. annealed at 500 °C for 30 minutes in air). The samples are deposited on both Si (100) and quartz substrates. The SEM images show the a) and d) plan view, b) and e) 60° view, c) and f) zoomed 60° view of the Z_NS (right) and C_Z_NS (left) structures with a clear evidence of the internal voids following PS sphere removal …… 123
Figure 6.9: SIMS spectra of positive secondary ions at the boundary of the C_Z_F and C_Z_NS structures. Increasing spectrum number indicates increased overall sputtering time, as discussed in the main text …….. 124
Figure 6.10: Relative secondary ion emission yields for Zn, Ce, CeO and CeO_2 positive ions as a function of depth at the boundary of the composite C_Z_F structure grown on a Si (100) substrate …… 125
Figure 6.11: Room temperature UV-Vis absorbance spectra of Z_F, C_F and C_Z_F (thickness ~ 120 ± 10 nm) on quartz substrates …….. 126
Figure 6.12: Tauc plot of $(\alpha h\nu)^2$ as a function of photon energy ($h\nu$) for C_F, Z_F (top) and C_Z_F (bottom) samples ……... 128
Figure 6.13: Room temperature UV-Vis absorption spectra of Z_F, C_Z_F, Z_NS and C_Z_NS samples, under normal incidence, with a clear indication of an increase in the absorption (ΔA) as a result of the nanoshell structure geometry …… 130
Figure 6.14: Integrated relative absorbance for different incidence angles relative to normal incidence for samples Z_NS and C_Z_NS …….. 131
Figure 6.15: Room-temperature PL spectra of Z_F, C_Z_F, Z_NS and C_Z_NS samples …….. 132
Figure 6.16: Room-temperature PL spectra of the short wavelength emission region for metal-oxide films in the range of 3.6 – 3.75 eV, compared to the emission seen from a bare Si wafer under identical conditions …… 132
Figure 7.1: A schematic representation of the annealing furnace and annealing parameters used to decompose the chemical solution to yield pure nanocrystalline CeO_2 films …….. 139
Figure 7.2: The impact of spin acceleration (a) on the average thickness and thickness uniformity of the 400 °C – 500 °C CeO_2 film, $v_{constant}$ = 3000 rpm and $T_{constant}$ = 40s …….. 140
Figure 7.3: The impact of spin speed (v) on the average thickness and thickness uniformity of the 400 °C – 500 °C CeO_2 film, $a_{constant}$ = 540 rpm/s and $T_{constant}$ = 40s ……... 141

Figure 7.4: Plan view SEM image of the decomposed 400 °C -500 °C CeO_2 film deposited by spin coating using cerium nitrate as a starting material to yield CeO_2 ……...……... 142
Figure 7.5: XRD θ-2θ patterns of decomposed CeO_2 film deposited by a spin coater and annealed at a) 400 °C- 500 °C and b) 400 °C -800 °C for 30 minutes at each temperature …….…… 143
Figure 7.6: EDX spectrum for the 400 °C -500 °C CeO_2 film ……..... 144
Figure 7.7: XPS Ce 3d core level spectra for spin coated a) 400 °C-500 °C CeO_2 and b) 400 °C-800 °C CeO_2 films ……..…….. 145
Figure 7.8: O 1s XPS spectra of spin coated 400 °C-500 °C and 400 °C-800 °C CeO_2 …….……146
Figure 7.9: Room temperature UV-Vis absorption spectra of CeO_2 film deposited by a spin coater on quartz substrates a) 400 °C-500 °C and b) 400 °C-800 °C ……... 147
Figure 7.10: Tauc plot of $(\alpha hv)^2$ vs. hv for the CeO_2 films deposited by a spin coater on quartz substrates a) 400 °C-500 °C sample and b) 400 °C-800 °C sample …… 148
Figure 7.11: SEM images (top and 60° views) of the 400 °C-500 °C CeO_2 nanostructures after the decomposition of the residual cerium salt into CeO_2 and the removal of the PVA binder (0.2 g) and PS nanospheres ……. 149
Figure A.1: XPS Zn 2p spectra of ZnO seed layer film deposited on Si (100) substrate using zinc acetate as a starting material …….. 158
Figure A.2: XPS survey spectrum on ZnO seed layer film deposited on Si (100) substrate ……... 159
Figure A.3: O 1s XPS spectrum of ZnO seed layer film deposited on Si(100) substrate ……... 159
Figure A.4: C 1s XPS spectrum of ZnO seed layer film deposited on Si(100) substrate …….……... 160

List of Tables

Table 3.1: m/q values of different observed CeO_δ ion clusters …….. 58
Table 4.1 Rietveld refinement 'goodness of fit' values and out of plane coherence length for the CeO_2 films annealed at 500 °C, 800 °C and 1000 °C …… 74
Table 4.2: Summary of post-deposition annealing AFM and XRD results with variation in OFR. Samples are annealed at 800 ^oC for 1 hour ……. 79
Table 5.1: EDX atomic percentage ratios of the various elements on the CeO_2 dome-shaped nanostructures, before and after the removal of the PS nanospheres …….. 101
Table 6.1: Associated labels for sample structures used in this study ……. 117
Table 6.2: Summary of the FWHM values of the ZnO(002) XRD peaks of the various samples …… 121
Table 7.1: Summary of decomposed CeO_2 thin film deposits, with their associated labels ……... 139
Table 7.2: Optimised spin coating parameters to obtain the decomposed CeO_2 films with uniform thicknesses of 40 $\pm$ 5 nm, after ten distinct coating layers …….. 142
Table 7.3: EDX atomic percentage ratios of the various elements on the 400 °C -500 °C CeO_2 film …….. 144

Acronyms

AFM	Atomic Force Microscopy
AFR	Argon Flow Rate
CV	Cyclic Voltammetry
CSC	Charge Storage Capacity
DC	Direct Current
DI	Deionised or Distilled
EDS	Energy Dispersive X-Ray Spectroscopy
EDX	Energy Dispersive X-Ray Spectroscopy
fcc	Face Centred Cubic
FWHM	Full Width at Half Maximum
JCPDS	Joint Committee on Powder Diffraction Standards
LPL	Low-Temperature Photoluminescence
OFR	Oxygen Flow Rate
OSC	Oxygen Storage Capacity
OVD	Oxygen Vacancy Defects
PDCMS	Pulsed DC Magnetron Sputtering
PDF	Powder Diffraction File
PL	Photoluminescence
PS	Polystyrene
PVD	Physical Vapour Deposition
RF	Radio Frequency
RT	Room Temperature
SCE	Saturated Calomel Electrode
SEM	Scanning Electron Microscopy
SIMS	Secondary Ion Mass Spectrometry
SOFC	Solid Oxide Fuel Cells
STM	Scanning Tunnel Microscope
TGA	Thermogravimetric Analysis
UHU	Ultra-High Vacuum
UV	Ultra Violet
UV-Vis	Ultra Violet and Visual Absorption Spectroscopy
WGM	Whispering Gallery Mode
XPS	X-Ray Photoelectron Spectroscopy
XRD	X-Ray Diffraction

Chemicals

Ar	Argon
Cd	Cadmium
CdO	Cadmium Oxide
Ce	Cerium
$CeCl_3$	Cerium Chloride
$Ce(NO_3)_3$	Cerium Nitrate
CeO	Cerium Monoxide
$Ce(OH)_3$	Cerium (III) Hydroxide
CeO_2	Cerium Oxide, Ceria, Cerium (III) Oxide, Cerium Dioxide
Ce_2O_3	Cerium (IV) Oxide
$Ce_2(SO_4)_4$	Cerium Sulphate
$(C_8H_8)_n$	Polystyrene
DMF	N,N-Dimethylformamide
EtOH	bsolute Ethanol
Fe	Iron
FeO	Iron (II) Oxide
Fe_3O_4	Iron (II, III) Oxide
Ga	Gallium
GeO	Germanium Monoxide
GeO_2	Germanium Dioxide
H_2	Hydrogen
H_2O	Water
H_2O_2	Hydrogen Peroxide
NbO_2	Niobium (IV) Oxide
Nb_2O_5	Niobium (V) Oxide
$NH_4Ce(NO_3)_4$	Ammonium Cerium Nitrate
In	Indium
In_2O_3	Indium Oxide
ITO	Indium Tin Oxide
$LiClO_4$	Lithium Perchlorate
Mg	Magnesium
MgO	Magnesium Oxide
Mn	Manganese
MnO	Manganese (II) Oxide
Mn_3O_4	Manganese (II, III) Oxide
NH_4OH	Ammonium Hydroxide

Ni	Nickel
O_2	Oxygen
PVA	Poly Vinyl Alcohol
Si	Silicon
SiO_2	Silicon Oxide
SnO	Stannous Oxide or Tin Oxide
SnO_2	Stannic Oxide or Tin (II) Oxide
TiO_2	Titanium Oxide
W	Tungsten or Wolfram
WO_3	Tungsten Trioxide
Xe	Xenon
Zn	Zinc
ZnO	Zinc Oxide
ZrO_2	Zirconium Oxide or Zirconium Dioxide
$Zn(O_2CCH_3)_2$	Zinc Acetate

Abstract

Ceria-based solar-driven thermochemical conversion is a promising solution for efficient and sustainable hydrogen production. This is mainly due to the oxygen storage capacity (OSC) property of ceria (CeO_2), which results from the fact that CeO_2 can oxidise and reduce molecules. Oxygen vacancy defects can be rapidly formed and eliminated, giving CeO_2 its high OSC. The ability to combine this unique material property with improvements in optical absorption, through the use of a novel light management structure geometry based on low-quality factor whispering-gallery resonant modes inside a spherical nanoshell structure, is a matter of great interest. The growth of spherical ceria nanoshells will support whispering-gallery resonant modes with enhanced light absorption, enabling an efficient solar thermal-driven process, while the nanostructure morphology will also lead to enhanced redox activity due to the large surface to volume ratio. These features will both lead to efficient solar-driven thermochemical hydrogen production. In this work, nanostructured CeO_2 thin films are deposited by pulsed DC magnetron sputtering (PDCMS) and wet chemical techniques. The influences of using various gas ambients in the sputtering chamber on the films during deposition are studied. The film compositions, OSC, electrochemical and optical properties are characterised using several characterization techniques including: scanning electron microscopy (SEM), atomic force microscopy (AFM), x-ray diffraction (XRD), x-ray photoelectron spectroscopy (XPS), secondary ion mass spectrometry (SIMS), photoluminescence (PL) and ultra-violet and visible (UV-Vis) absorption spectroscopy. The film composition spectra shows a phase transition related to the transformation of Ce^{4+} to Ce^{3+} and indicates a chemically reduced state of CeO_2. This transformation is due to both the sputtering process and gas ambient. TGA and electrochemical CV studies show that films deposited in an Ar atmosphere have a higher oxygen storage compared to films deposited in the presence of O_2. Moreover, the effects of oxygen partial pressure and temperature during post-deposition annealing on the properties of PDCMS CeO_2 thin films including crystalline structure, grain size and, shape and optical properties are investigated and it is shown that these quantities play important roles influencing the size and shape of the nanocrystals. Finally ZnO and CeO_2 coated ZnO spherical nanoshell structures were successfully engineered and their optical absorption properties are extensively studied.

Chapter 1

INTRODUCTION

1.1 INTRODUCTION

Nowadays, there are several challenges facing the world. They include a transition away from fossil fuel-based energy, reducing harmful side-effects caused by manufacturing and transportation, preventing future pollution, remediating environmental issues, and producing safe pharmaceuticals. However, energy shortages and environmental pollution are the two crucial challenges that need to be resolved; which can be achieved by developing new sources of fuel and energy and new environmental friendly technologies. An alternative energy carrier such as hydrogen (H_2) must be developed to face problems linked to the continuous rising of oil prices and to the global warming issue due to greenhouse effects [1]; as well as the fact that fossil fuels draw on finite resources that will eventually dwindle. Therefore, employing conversion systems based on renewable energies such as a solar energy for the production of H_2, which is a promising solar fuel, is one very viable potential solution to the problem [2, 3]. Correspondingly,

new materials could help to develop new energy sources and treat pollution. The literature shows promising materials for such applications to be mostly metal-oxide based. This implies that metal-oxide based conversion systems, such as cerium-oxide based water-splitting thermochemical cycles coupled to a solar energy source, constitute one favourable option for H_2 production (and solar energy storage) since this pathway does not use fossil fuels [4-6].

1. 2 SOLAR ENERGY & FUEL GENERATION

Energy in thermodynamics is defined as the capacity to do work but from a more practical point of view energy is the mainstay of any industrial society and it exists in a variety of forms including electrical, chemical, thermal, mechanical and radiative. It has a S. I. unit of Joules ($J = kg\ m^2\ s^{-2}$). The energy unit watt-hour (Wh) is used extensively in metering of electrical energy from the grid as a commercial electricity unit of energy. In terms of power, the S. I. unit is the watt (W=J/s). This unit is applied for measures of power or the rate of energy generation/demand. In Ireland, energy is currently provided by several primary sources: oil, natural gas, coal, petroleum, peat, hydroelectric, wind energy, biomass and other renewable energy sources [7]. Ninety percent of these fuels are imported and the remainder are mainly based on renewable energy. The first four sources are fossil fuels which are used so rapidly that they soon will be depleted. To maintain Ireland's present social structure and prevent non-renewable energy environmental impacts, it is desirable that Ireland supply an increasing portion of its energy from renewable sources. Currently, the target for renewable energy in Ireland is 16% by 2020.

The radiation solar energy reaching the earth during each month is approximately equivalent to the entire world supply of fossil fuels.

Therefore, the global potential of solar energy is many times larger than the current energy consumption. Approximately 30% of the solar energy striking the earth is reflected out into space. The remaining 70% (approximately 120,000 terawatts [1 terawatt is equal to 10^{12} watts]) is absorbed by the earth and its atmosphere. The solar radiation reaching the earth degrades in several ways. Some of the radiation is directly absorbed as heat by the atmosphere, the ocean and the ground. Other components produce atmospheric and oceanic circulation, while some evaporates, circulates and precipitates water in the hydrologic cycle. Finally, a very small fraction is captured by green plants and drives the photosynthetic process [8]. The earth's solar energy distribution is represented schematically in Figure 1.1.

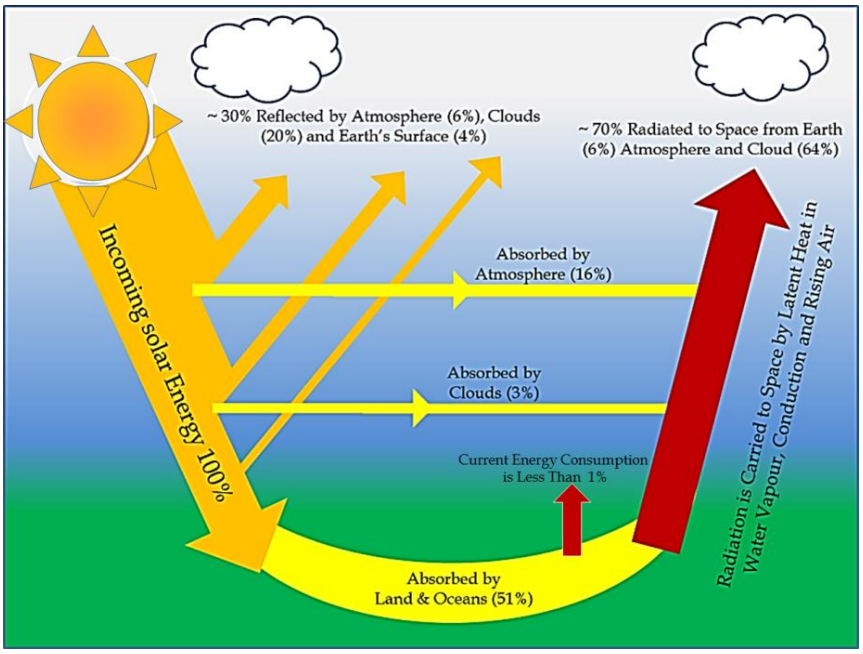

Figure 1.1: A schematic diagram of the earth's solar energy distribution.

Currently, and in the past several decades, most of the proposed applications of solar energy are based on collection and conversion of sunlight into a usable energy such as heat for example, which is used directly in space and water heating, or electricity by means of a Carnot engine [9]. Some applications allow for the direct conversion of sunlight to electricity as

in the silicon solar cell [10]. However, additional steps are then required for energy storage and distribution. As fossil fuels are presently being depleted quite rapidly, it is highly desirable to have an efficient and economical way of directly converting and storing solar energy as a chemical fuel [9]. This is mainly because there is a high demand for chemical fuel as a result of the dramatic increase in the worldwide annual motor vehicular production; as well as the huge negative impact that automobiles are having on the environment. For that reason, H_2 energy is one of the most promising solutions to store and transport renewable energy in a chemical form. It can be efficiently converted into electricity through fuel cells and it is also useful in resolving the issue of greenhouse gas emissions since H_2 is environmentally friendly, and is produced by a clean process involving renewable energy.

To utilise the abundant solar energy referred to above, large-scale H_2 production from solar energy is an appealing route. This is particularly the case as among all the thermochemical and photochemical energy storage reactions proposed in literature, the production of H_2 and oxygen (O_2) from water (H_2O) is certainly the most attractive:

$$H_20 \rightarrow H_2 + \frac{1}{2}0_2 \qquad (1.1)$$

H_2 is an almost ideal form of fuel and the starting material (H_2O) is certainly cheap and abundant. H_2O is transparent to solar radiation in the ultraviolet and visible regions. It does not begin to absorb until below 200 nm. Therefore, the direct photolysis of H_2O with solar radiation is not possible and as a consequence, the reaction must be sensitised by oxidation reduction catalysts in cyclic reactions.

Presently, three main pathways (and some combinations) are developed with solar energy for H_2 production; electrochemical, photochemical and thermochemical. A well-known electrochemical

technology, water electrolysis, has already been investigated for many years, whereby an electrical current passes through two electrodes, submerged in an electrolyte. The process can occur at both ambient and high temperatures. At high temperature, steam is the raw material instead of water. For electrolysis at high temperatures, the most used technology is based on solid oxide cells. These consist of a solid electrolyte, a cathode (where hydrogen is produced) and an anode (where oxygen is released). Water is heated with solar energy before entering the electrolysis cell as steam. The steam is supplied to the cathode, where it decomposes into oxygen ions and hydrogen. The hydrogen is then separated as one decomposition product and oxygen ions move through the solid electrolyte to the anode, where oxygen is obtained as the other decomposition product [11, 12]. Photochemical processes, on the other hand, use solar light to produce hydrolysis of water. These may require an electrical energy to aid the hydrolysis process; such procedures are known as photoelectrochemical. In the photoelectrochemical process, water is split into hydrogen and oxygen in a single step on a single device. In a photoelectrochemical device, a photovoltaic cell can transform solar energy and be used as one of the electrodes. The photovoltaic device has to generate enough voltage to chemically split water (at least 1.6 V) and its surface has to conduct electricity, as well as resist the corrosion produced by the electrolyte and catalyse the electrochemical reactions [12, 13].

This thesis concentrates on the thermochemical approach which is based on the use of concentrated solar radiation as the driving force to split the H_2O molecules for H_2 production. This approach represents a very promising technology for sustainable H_2 production in support of the future energy system as it uses the full solar spectrum unlike the electrochemical and photochemical approaches. There are five different thermochemical routes for solar H_2 production which are illustrated in Figure 1.2. These

routes differ in the chemical source of H_2: H_2O for the solar thermolysis and solar thermochemical cycles; fossil fuels for the solar cracking; and a combination of fossil fuels and H_2O for the solar reforming and solar gasification. All these routes involves endothermic reaction through the use of concentrated solar radiation as the energy source of high-temperature process heat [14]. The overall motivation for moving to renewable energies is to avoid using fossil fuels and therefore, the only two routes that use the abundant raw material water as the main source for H_2 production are solar thermolysis and solar thermochemical cycles. Ideally single-step thermal dissociation of H_2O (also known as water thermolysis) is the most simple conceptual process (Equation 1.1) which directly concentrates solar energy into a chemical reactor that performs the decomposition of H_2O into H_2 and O_2. However, due to the need of a high-temperature heat source at above 2500 K to obtain a significant H_2 and O_2 conversion yield and the necessity for an effective technique for H_2/O_2 separation to avoid recombination or an explosive mixture, the development of direct water splitting has been very challenging [15-17]. On the other hand, H_2 production by water-splitting thermochemical cycles bypass the problem of H_2/O_2 separation and further allow operating at a lower temperature than the water thermolysis process [14]. Therefore, the development of water-splitting thermochemical cycles has been extensively explored in recent times.

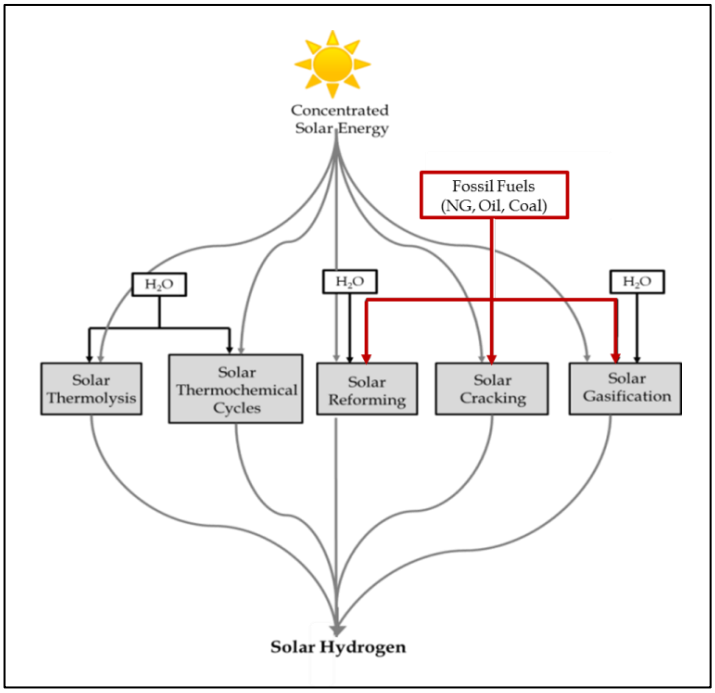

Figure 1.2: The five thermochemical routes for solar hydrogen production [14].

1. 3 TWO-STEP THERMOCHEMICAL CYCLE

As mentioned above, two-step solar-driven water-splitting thermochemical cycles appear to be very attractive among the different H_2 production methods because the resources, solar energy and water, are abundant and clean and also require a lower temperature than the water thermolysis process. Additionally, they are potentially more efficient than electrolysis because the intermediate conversion of heat to electricity does not limit the global solar energy to H_2 energy efficiency [2, 5]. Water-splitting thermochemical cycles are processes in which H_2O is decomposed into H_2 and O_2 by chemical reactions using intermediate reactions and substances. All of these intermediate substances are recycled within the processes i.e. the sum of all the reactions is equivalent to the dissociation of the water molecule [18]. Theoretically, it only requires heat to process these chemical steps.

There have been several significant works that have reviewed thermochemical cycles for the production of H_2 [19, 20]. One of the earliest investigations for multistep thermochemical H_2 production from H_2O was by Funk and Reinstorm in the 1960s [21]. These authors evaluated the energy requirements and possibility of employing two-step processes for H_2O dissociation and H_2 production by oxides and hydrides. The research interest in thermochemical H_2O-splitting cycle grew further in the later 1970s and early 1980s with the oil crisis and since then many research papers regarding these cycles have been published [22-24]. Previous studies performed on water-splitting thermochemical cycles for H_2 production are mostly characterised by using process heat temperatures below 1200 K using nuclear and other thermal sources. These cycles required multiple steps, usually more than two, which lead to inherent inefficiencies associated with heat transfer and product separation at each step [14]. However in recent years, a significant progress in the development of large-scale optical systems capable of achieving mean solar concentration ratios exceeding 5000 suns (1 sun = 1 kW/m^2, equivalent to stagnation temperatures exceeding 3000 K) has been accomplished. This allows the conversion of concentrated solar radiation to thermal reservoirs at 2000 K and above. This has created the opportunity for the exploration of a more efficient two-step water-splitting thermochemical cycle for H_2 production using solar energy [20].

In a two-step water-splitting thermochemical cycle over a nonstoichiometric oxide, the first step is the thermal reduction of the metal oxide into the metal or the lower-valence metal oxide. This is achieved using concentrated solar radiation (endothermic reaction) as the source of high-temperature process heat (Equation 1.3) and as a result oxygen is released. The second step is non-solar (exothermic), where the metal or lower-valence of the metal oxide is oxidised by the H_2O (hydrolysis) to produce H_2 and the corresponding metal oxide (Equation 1.4).

Higher temperature, T_H – solar-driven endothermic step

$$MO_x \rightarrow MO_{x-\delta} + \frac{\delta}{2} O_2(g) \quad (1.3)$$

Lower temperature, T_L – non-solar, exothermic step (hydrolysis)

$$MO_{x-\delta} + \delta H_2O(g) \rightarrow MO_x + \delta H_2(g) \quad (1.4)$$

Net H_2 dissociation

$$H_2O(g) \rightarrow \frac{1}{2} O_2(g) + H_2(g) \quad (1.5)$$

In the above equations, M denotes a metal. The net reaction (H_2) dissociation is presented in Equation 1.5, but since H_2 and O_2 are formed in different steps, the need for high-temperature gas separation is thereby eliminated. This cycle was originally proposed by Nakamura [25] using the redox pair Fe_3O_4/FeO. This method required a high temperature above 2500 K for the thermal reduction process. This extremely high temperature resulted in severe sintering and melting as well as the thermal decomposition of Fe_3O_4 due to vaporisation, thereby making the cycle impracticable. Nevertheless, this introduced the notion of metal oxides as thermochemical reaction media and a new materials strategy for thermochemical fuel production. In order to lower the temperature of the first step, further work was carried out including substituting Fe in Fe_3O_4 by other metals, such as Mn and Ni, to form mixed metal oxides. These new combinations can be reduced at lower temperatures than those required for the reduction of Fe_3O_4, while the reduced phase of the mixed oxide remains capable of splitting water [26, 27].

1. 4 REDOX PAIR METAL OXIDES

The most promising reactions involved in thermochemical cycles are based on metal compounds such as iodine, chlorine and bromine as well as metal oxides. Most of the cycles have either increased complexity or involve

management of highly toxic and corrosive reactants. However, in the two-step solar thermochemical H_2O-splitting cycle, the redox pair of metal oxides aids the process, allowing for less complex chemical steps and involvement of noncorrosive materials [28]. The concept behind the redox pair metal oxides is the utilisation of metals with multiple oxidation states for the removal/storage of oxygen from water during the exothermic step.

Apart from the originally proposed cycle by Nakamura using the redox pair Fe_3O_4/FeO, a number of other redox pairs such as WO_3/W, ZnO/Zn, CdO/Cd, Mn_3O_4/MnO, Nb_2O_5/NbO_2, Co_3O_4/CoO, In_2O_3/In, etc. have been studied. Lundberg for example did thermodynamic calculations for the redox pairs of Co_3O_4/CoO, Mn_3O_4/MnO, and Nb_2O_5/NbO_2, in addition to Fe_3O_4/FeO [29]. Results showed that Mn_3O_4 and Co_3O_4 could be thermally decomposed in air at 1810 K and 1175 K, respectively. However, the H_2 yields are only 2×10^{-3}% and 4×10^{-7}% at 900 K for Mn_3O_4/MnO and Co_3O_4/CO, respectively. The H_2 yield at 900 K reached 99.7% for Nb_2O_5/NbO_2, but the thermal decomposition temperature of 3600 K in air is extremely high and is much higher than their melting points [29]. For the In_2O_3/In, WO_3/W etc. redox pairs, higher thermal reduction temperatures than that of Fe_3O_4/FeO are required. The thermal reduction of CdO is at a low enough temperature, below 1600 K, but melting restricted the hydrolysis of Cd [30]. Among all these redox pairs ZnO/Zn is a potential candidate and most promising redox pair in two-step thermochemical water splitting and this system has been extensively examined [31]. However, more newly proposed redox pairs, such as SnO_2/SnO, CeO_2/Ce_2O_3, GeO_2/GeO, MgO/Mg etc., have been demonstrated in the most recent period. But CeO_2/Ce_2O_3 in particular has emerged as an attractive redox active material because of its ability to rapidly conduct O^{2-} contributing to fast redox kinetics [2, 32], as compared to ferrite-based and other non-volatile metal oxides [33, 34]. CeO_2/Ce_2O_3 was first demonstrated by Abanades and Flamant as a new

cycle for H_2 production and the feasibility of the new thermochemical two – step cycle has been experimentally investigated at lab-scale [4]. This allowed researchers to explore CeO_2 and CeO_2–based metal oxides in relation to their applicability as reactive intermediates in solar thermochemical redox cycles [35, 36].

1. 5 CERIA

Cerium oxide or ceria (CeO_2) is an oxide of the rare earth element cerium (Ce), which is a member of the fourteen lanthanides, and is one of the most abundant rare earth elements that is present at about 64-66 parts per million (ppm) as a free metal or oxide in the earth's upper crust. Stoichiometric CeO_2 has a cubic fluorite lattice (Figure 1.3), a face centred cubic (fcc) crystal structure, with four cerium and eight oxygen (O) atoms per unit cell. CeO_2 can be synthesized directly from cerium metals or from salts/precursors of cerium such as cerium sulphate [$Ce_2(SO_4)_4$], cerium nitrate [$Ce(NO_3)_3$], ammonium cerium nitrate [$NH_4Ce(NO_3)_4$] and cerium chloride ($CeCl_3$).

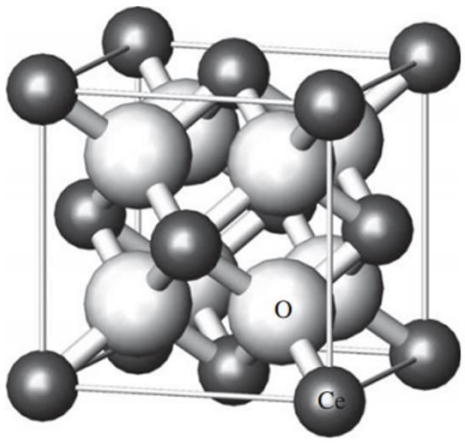

Figure 1.3: Crystal structure of the cubic fluorite lattice of CeO_2. Here Ce and O atoms are shown by grey and white circles, respectively [2].

1.5.1 CERIA NANOPARTICLES

Nanomaterials have recently become one of the most active research fields in the areas of solid state physics, chemistry and engineering [37]. Nanostructured materials are defined as being assembled of ultra-fine particles with a dimension below 100 nm. They exhibit properties that are usually somewhat different to those of bulk materials. The local solid-state structure of nanomaterials is often of prime importance. The prospective impact of nanomaterials in science and technology is high and stems from their unique property that deviates from bulk solid properties [38]. These properties include novel mechanical and magnetic properties, high surface to volume ratio, ordered self-assembly of nanocrystals, size and shape dependent catalytic properties [38, 39]. Recent technological developments in instrumentation for production and characterisation of nanostructures, in combination with increased computing power for quantum chemical calculations and development of theoretical models have meant ever greater ranges of applications and expected applications, for these materials.

In particular, CeO_2 nanoparticles have been used efficiently in various advanced technologies, such as catalytic materials [40], solid-oxide fuel cells [41], and as a high-temperature oxidation protection material in an O_2 sensor [42], solar cells [43] and two-step thermochemical cycling [2]. The remarkable catalytic chemistry involved with nanostructured CeO_2 is mainly due to its high mobility of surface O vacancies. This feature results from the material's ability to easily and repeatedly switch between its oxidation and reduction states (Ce^{3+} and Ce^{4+}) [44]. From room temperature to the melting point and under ambient pressures, fully oxidized CeO_2 adopts the ideal cubic fluorite crystal structure shown in Figure 1.3 above. However, under reducing conditions, some of the Ce converts to the Ce 3+ oxidation state. These reduced species are charge-balanced by O vacancies, where δ in the stoichiometry formula $CeO_{2-\delta}$ represents the vacancy concentration. A

remarkable feature of CeO_2 is that, particularly at high temperatures, exceptionally high vacancy concentrations can be accommodated without a change in crystallographic structure (or phase) [2]. Among native defects in CeO_2, the O vacancy is by far the most extensively studied and the most stable defect under a wide range of conditions. As previously mentioned, the formation of neutral O vacancies in CeO_2 involves a reversible change in the oxidation state of two cerium ions from Ce(IV) to Ce(III). This process can be written as:

$$O^{2-} + 2Ce^{4+} \rightarrow 2Ce^{3+} + \frac{1}{2}O_2(g) \tag{1.6}$$

or in Kröger-Vink notation:

$$O_o^x + 2Ce_{Ce}^x \rightarrow V_o^{\bullet\bullet} + 2Ce'_{Ce} + \frac{1}{2}O_2(g) \tag{1.7}$$

Where an O ion (formally O^{2-}) leaves the lattice as a neutral species ($\frac{1}{2}O_2(g)$), the two electrons left behind in the process get trapped at two cerium sites. At each cerium site, the electron occupies an empty Ce4f-state and the Ce4f band in CeO_2 is split into two bands: an occupied $Ce4f_{Full}$ band and an empty $Ce4f_{Empty}$ band (see Figure 1.4b). In CeO_2, a number of higher oxides of cerium with composition $CeO_{2-\delta}$ ($0 \leq \delta \leq 0.5$) exist and the practical reduction limit of nonstoichiometic CeO_2 is Ce_2O_3, where all cerium ions are found in a Ce(III) oxidation state [45].

1.5.2 CERIA OXYGEN STORAGE CAPACITY

As mentioned earlier, the literature often attributes the catalytic activity of CeO_2 to its high oxygen storage capacity (OSC), which is largely due to the multi-valence nature of cerium and the high mobility of oxygen vacancies at the surface of materials. The shift between the Ce^{3+} and Ce^{4+} states leads to a

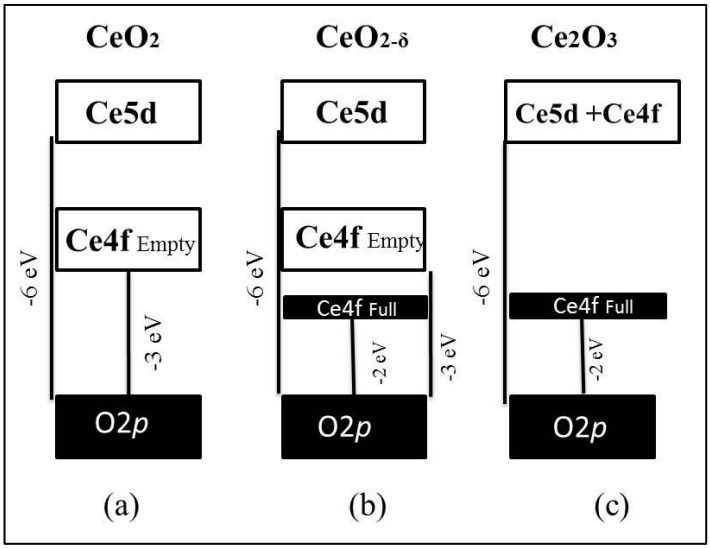

Figure 1.4: Schematic electronic structures of (a) stoichiometric CeO_2, (b) partially reduced $CeO_{2-\delta}$ and (c) Ce_2O_3. Filled bands are drawn as filled boxes and empty bands are drawn as empty boxes [46].

high oxygen mobility in the CeO_2 lattice that in turn leads to a strong catalytic potential [47]. However, the degree of oxygen mobility in the CeO_2 lattice can be attributed to the size, dispersion, and quantity of oxygen vacancy defects (OVD) [48, 49]. These phenomena can be explained by the synthetic method and conditions and by post processing methods used to deliberately introduce defects into the crystal structure. It is important to note that ceria with a significant concentration of OVD is the most stable configuration under a range of conditions. Figure 1.5 shows the formation of OVD in the ceria lattice.

The process of oxygen storage and transport in ceria can be described by the defect mechanism and there are two types of defects: intrinsic and extrinsic [50, 51]. The former is due to the oxygen anion vacancies created upon the reduction of ceria, and; the extrinsic defects are due to the oxygen anion vacancies created by the charge compensation effect of foreign cations, which have a valence lower than that of the host Ce ions they substitute.

Both of these vacancies are believed to provide a practical way to increase the OSC of CeO_2.

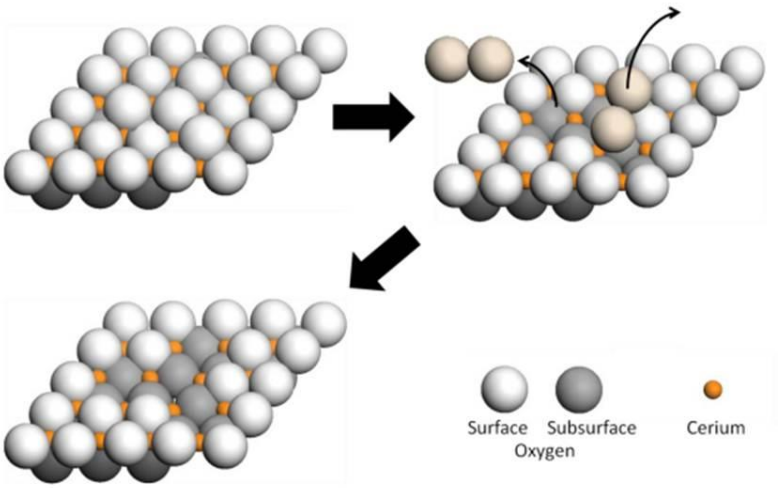

Figure 1.5: Formation of an OVD in CeO_2. OVD formation follows the basic step of O diffusion through the lattice. When an O encounters another O atom, a bond is formed and the O_2 molecule is able to diffuse away from the surface of the crystal. Each O atom that diffuses away from the surface leaves behind two electrons to be shared between three cerium atoms. This results in a partially reduced cerium atom to a valency between 3+ and 4+ states. [52]

1.5.3 CERIA IN THERMOCHEMICAL CYCLES

As mentioned above, CeO_2 and CeO_2-based materials are capable of achieving remarkably high vacancy concentrations at elevated temperatures and as a result, CeO_2 is attractive as a reactive intermediate in thermochemical redox cycles for the production of solar fuels [50, 53]. The CeO_2 splitting cycle consist of two separate thermochemical reactions, similar to the reactions described in section 1.3, a high temperature endothermic reduction and a low temperature exothermic oxidation, as represented in Equation (1.8) and (1.9), respectively.

$$CeO_2 \rightarrow CeO_{2-\delta} + \frac{\delta}{2}O_2(g) \qquad (1.8)$$

$$CeO_{2-\delta} + \delta H_2O\ (g) \rightarrow CeO_2 + \delta H_2(g) \qquad (1.9)$$

As the reduction proceeds, oxygen vacancies are formed and O_2 gas is released resulting in the subsequent change in stoichiometry (δ). Oxidation proceeds with H_2O, thereby releasing H_2 and reincorporating oxygen into the lattice. As a result, the number of oxygen vacancies created during reduction is directly related to the yield of fuel production that can be achieved. As ceria is recycled, the net reaction is simply the splitting of H_2O, whose products can be used directly as a fuel [36].

A number of dopants have been used successfully in thermochemical redox cycles to promote the reduction of CeO_2 to a nonstoichiometric state at moderate temperatures. In particular, zirconium oxide [6, 54] and chromium oxide [55] doped CeO_2 have exhibited remarkably lower thermal reduction temperatures than CeO_2 that has not been doped. Additionally, Fe, Ni, Mn, and Cu oxide based dopants have been investigated with various degrees of success [56]. The thermodynamics of nonstoichiometric ZrO_2−CeO_2 have been studied at elevated temperature, but experimental data is limited to much higher ZrO_2 mole fractions than are feasible for thermochemical redox cycles [57]. Several dopants have been thermodynamically examined based on O_2 nonstoichiometry data. Most of these studies are conducted at temperatures much lower than those required for solar thermochemical fuel production. The motivation for most of the thesis work has arisen from the application of CeO_2 as a solid electrolyte in solid oxide fuel cells and two-step thermochemical cycles.

1. 6 WHISPERING GALLERY MODES

In the thermochemical cycle process and in order to increase the H_2 production, it is important that the surface area is maximised. In the majority of previously completed research, this is done through the formation of porous structures (see Figure 1.6) [58]. In the context of this thesis, the aim is

to increase the surface area through the engineering of spherical nanoshell structures of the materials. This type of structure will also support whispering-gallery mode (WGM) resonances with enhanced light absorption, enabling an efficient solar thermal-driven processes and efficient H_2 production. The term "whispering gallery" refers to a round room designed in such a way that sound is carried around its perimeter. This allows a person standing on one side to hear words whispered by a person on the other. Recently, scientists from Stanford University have developed a new type of photovoltaic material that essentially does for sunlight what whispering galleries do for sound. Not only does the material have a structure that circulates light entering it, but it could also result in cheaper, less fragile and less angle-sensitive solar panels [59]. This discovery of enhanced broadband light absorption is specifically described by Yao et al. [59] and it is considered an important new design parameter for high performance solar cells and photodetectors. This new method of light management using low-quality factor WGM resonances inside a spherical nanoshell structure is demonstrated by Yao et al., where the geometry of the structure dramatically improves absorption and reduces adverse directionality effects due to the substantial enhancement of the effective light path in the active material. Figure 1.7 highlights some results obtained by Yao et al. on the effectiveness of the spherical geometry on enhancing light absorption.

WGM resonators operating at optical frequencies have been successfully used to build filters [60], laser cavities [61], wave mixers [59] and sensors [62]. These applications require resonators with a quality factor ranging from 10^5 to 10^9 or even higher. This is because high-Q resonators have very little energy leakage and high-frequency selectivity at the expense of a low coupling efficiency of light into the resonator. In comparison, the application of WGMs to broadband absorbers requires the opposite resonator

characteristics, such as high absorption, low frequency selectivity and strong in-coupling, which favour low-quality resonators ($Q < 10^5$). In the optical region, the quality factor of a resonant is defined by

$$Q = 2\pi f_o \frac{E}{P} \tag{1.10}$$

where f_o is the resonant frequency, E is the stored energy in the resonant cavity and $P = -\frac{dE}{dt}$ is the power dissipated.

Yao et al. takes advantage of low-quality WGMs in spherical nanoshells to dramatically enhance broadband absorption, where most of the incoming light couples into the WGMs in the spherical nanoshells and circulates in the active materials with a considerably longer path length than the same material in the form of planar film thereby substantially reducing the amount of material required for significant light absorption.

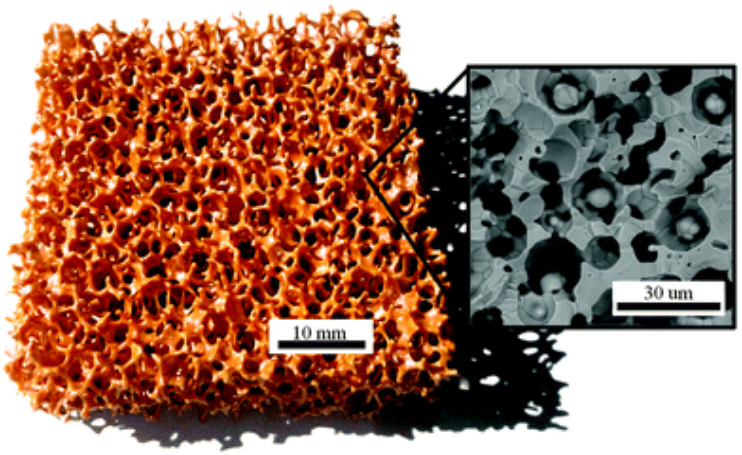

Figure 1.6: Photograph of the reticulated porous ceramic made of ceria. Inset: SEM micrograph of a break plane of its struts. [63]

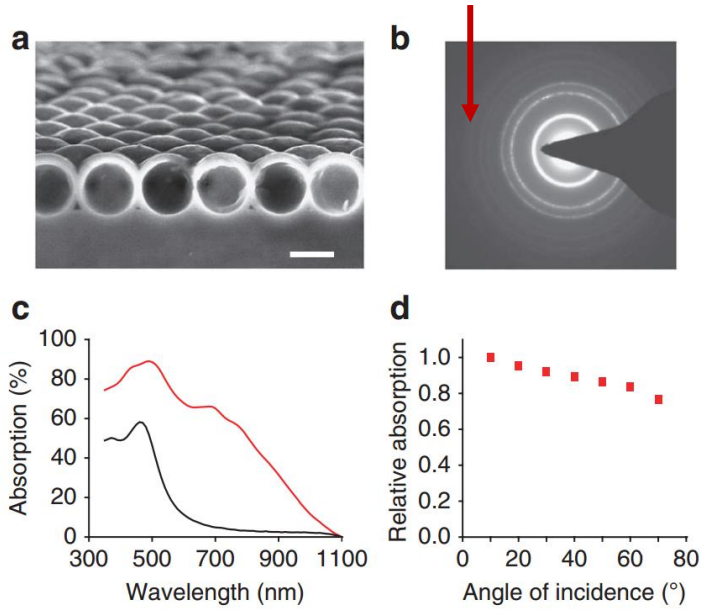

Figure 1.7: Nanocrystalline Si spherical nanoshell morphology and optical absorption. (**a**) SEM cross-sectional image of a monolayer of Si spherical nanoshells on a quartz substrate. Scale bar equals 300nm. (**b**) Electron diffraction pattern showing the nanocrystalline nature of Si nanoshells. (**c**) Integrating sphere measurement of absorption spectra under normal incidence for the thin film sample (black line) and nanoshell sample (red line). (**d**) Integrated absorption over the global solar spectrum (ASTM G173-03) for different incidence angles relative to normal incidence. [59].

1. 7 THESIS SCIENTIFIC QUESTIONS

In the context of the brief introduction above about the importance of hydrogen production and the great potential of the redox active ceria for the future two-step thermochemical cycles in mind, the thesis seeks to address several scientific questions. They are as follows:

1. How can we develop optimal ceria thin films and nanostructures, and what are the properties of these materials?
2. How does the oxygen storage property of ceria deposits vary with the change of the deposition gas ambient?

3. What effects do different temperatures and gas ambients have on the structure, morphological and optical properties of the ceria deposits?
4. How can we effectively increase the surface area of the ceria nanostructures?
5. Is it possible to engineer spherical ceria nanoshell structures?
6. Do the spherical ceria nanoshell structures enhance the desired optical properties of the materials?

This thesis reports methods of growing ceria thin films and nanostructures and the characteristics of the resulting deposits. It also examines the engineering of spherical ZnO and CeO_2 coated ZnO nanoshells for enhanced light absorption, which is absolutely essential for the future research and solar thermal-driven applications based on these materials.

1.8 THESIS OVERVIEW

The work addressed in this thesis is part of a broader project; its ultimate goal is the development and testing of an enhanced solar-driven thermochemical cycling using low-quality whispering gallery modes in spherical CeO_2 and CeO_2 coated ZnO nanoshells. This thesis is concerned with the initial results obtained to date. We present results on the deposition, characterisation and optimization of CeO_2 nanocrystalline thin films required for the engineering of the two-step thermochemical cycling and the engineering of spherical ZnO and CeO_2 coated ZnO nanoshells. The following is an overview of the thesis structure:

- **Chapter 2** provides a description of the various experimental techniques used for the deposition of the thin films and the characterisation techniques used for their analysis. It contains detailed information about the two growth techniques: pulsed DC magnetron

sputtering and spin coating deposition; as well as the characterisation techniques such as XRD, XPS, AFM, SEM, SIMS, UV-Vis, PL, TGA and CV.

- **Chapter 3** addresses the development of nanostructured CeO_2 thin films by pulsed DC magnetron sputtering. It also concentrates on the control and enhancement of the oxygen storage capacity of CeO_2 films by facile tuning of the deposition gas ambient in the deposition chamber. The influence of the deposition gas atmosphere on the film stoichiometry and surface topography is also highlighted.

- **Chapter 4** concentrates on the crystal structure, morphology and optical properties of post-deposition annealed CeO_2 thin films deposited by pulsed DC magnetron sputtering. There is a detailed account of the effect of post-deposition annealing temperature and gas atmosphere on film crystalline structure and morphology, with clear evidence for variation of the RMS roughness and grain size and shape due to varying the oxygen flow rates during the post-deposition annealing. It also calls attention to the effect of post-deposition annealing on the film stoichiometry and optical properties.

- **Chapter 5** describes the development of high surface to volume ratio by the growth of hollow domed-shaped CeO_2 nanostructured on a polystyrene monolayer template using pulsed DC magnetron sputtering. It also contains a study on the optical properties resulting from the hollow dome-shaped nanostructures.

- **Chapter 6** demonstrates a simple and reproducible wet chemical method to fabricate ZnO and CeO_2 coated ZnO nanostructures. It also

describes the preparation of spherical structures of ZnO and CeO_2 coated ZnO nanoshells using polystyrene sphere monolayer templates. Within this chapter is a detailed account of structural, morphological and compositional properties of the deposited materials. It also underlines the significant enhancement in the ultra violet (UV) and visible light absorption, through the engineering of spherical nanoshells, due to the whispering gallery modes in such nanoshell cavities as well as the addition of the CeO_2 layer.

- **Chapter 7** focuses on a novel wet chemical-spin coating technique that consists of the growth of CeO_2 on amorphous substrates using a $Ce(NO_3)_3$/PVA aqueous solution. It also covers the initial characterisation of the deposit.

- **Chapter 8** concludes the thesis and highlights future work to be considered for the further development of CeO_2 nanoshell structures for light trapping and efficient energy production and testing devices for H_2 production.

Chapter 2

GROWTH AND CHARACTERISATION TECHNIQUES

2.1 INTRODUCTION

Numerous techniques are available for the deposition of thin films. Among these, pulsed DC magnetron sputtering and chemical deposition methods have become widely used in thin film technology [64, 65] for the production of thin, uniform films on planar substrates. This thesis explores the development of high surface to volume ratio CeO_2 nanocrystalline thin films using pulsed DC magnetron sputtering and chemical deposition methods. The structural, morphological, optical and electrochemical characterisation of the deposited films are investigated using a number of different techniques, including x-ray diffraction (XRD), spectroscopic ellipsometry, atomic force microscopy (AFM), scanning electron microscopy (SEM), energy dispersive x-ray (EDX), ultra violet and visible absorption spectroscopy (UV-Vis), x-ray photoelectron spectroscopy (XPS), thermogravimetric analysis (TGA) and

cyclic voltammetry (CV). The details of the growth processes and characterisation methods used in the study of these CeO_2 samples are explained briefly in this chapter.

2.2 FILM GROWTH TECHNIQUES

2.2.1 SPUTTERING

Sputtering is one of the most commonly used physical vapour deposition (PVD) techniques for the deposition of thin films [64, 66]. Sputtering is the ejection of atoms and/or molecules of a material from the target (or cathode) due to the bombardment of energetic ions on a surface generated in glow discharge plasma, located in front of the target. The energy transfer resulting from the bombardment process creates a collision cascade in the target material leading to the removal of target atoms, ions, molecules, secondary electrons and photons. The released target atoms and/or molecules may then deposit on the substrates as a thin film whereas the secondary electrons, emitted from the target as a result of bombardment, contribute to the stability and maintainability of the plasma discharge for the sputtering process.

To begin a sputtering process, inert gas such as argon (Ar) is introduced into the vacuum chamber (sputtering chamber) to provide an operating pressure in the mTorr range and a sufficiently high operating voltage is applied to the cathode to ionise the inert gas and initiate the plasma. This results in the bombardment process that causes the removal of target atoms and/or molecules, followed by the deposition of same on to the substrate. During the sputtering process (and due to the lower collision cross-section for electrons at lower gas operating pressures) the probability

for electrons to escape without colliding with gas increases. Therefore to obtain the required thin film deposition, the energetic ion bombardment should have sufficient energy to knock-off (sputter) the material atoms from the target surface and the emitted material atoms should move with minimal gas collisions toward the substrates. These conditions can be achieved by producing efficient ionization at lower pressures using magnetron designs. Furthermore, sputtering at low operating pressure results in more reproducible characteristics of thin films with minimal contamination [67].

2.2.1.1 MAGNETRON SPUTTERING

Magnetron sputtering has advanced rapidly over the last decade, to a point where it has become popular in many diverse market sectors due to advantageous features such as ease of technical adjustment and high-quality functional films. Magnetrons have been routinely used to rapidly deposit thin metal films for a broad range of applications from architectural glass and food packaging to thin films microelectronics [68] and solid oxide fuel cells [69]. In many cases, magnetron sputtered films now outperform films deposited by other PVD processes, and can offer the same functionality as much thicker films produced by other surface coating techniques. Consequently, magnetron sputtering now makes a significant impact in application areas including hard, wear-resistant coatings, low friction coatings, corrosion-resistant coatings, decorative coatings and coatings with specific optical or electrical properties [64].

The basic sputtering process has been known for many years and many materials have been successfully deposited using this technique. However, the process is limited by low deposition rates, low ionization efficiencies in the plasma even at lower pressures, a large number of electrons escaping in the vicinity of the cathode, and high substrate heating

effects. These limitations have been overcome by the development of magnetron sputtering and, more recently, unbalanced magnetron sputtering. In order to overcome limitations such as lower deposition rate and gas ionization efficiencies associated with the basic sputtering process, normally magnets are placed behind the target and the field is configured parallel to the target surface. The magnets are arranged in such a way that one pole is positioned at the central axis of the target and the second pole is formed by a ring of magnets around the outer edge of the target, which creates crossed electric and magnetic fields. The schematic of arrangement of the magnetron cathode and the sputtering deposition process is illustrated in Figure 2.1.

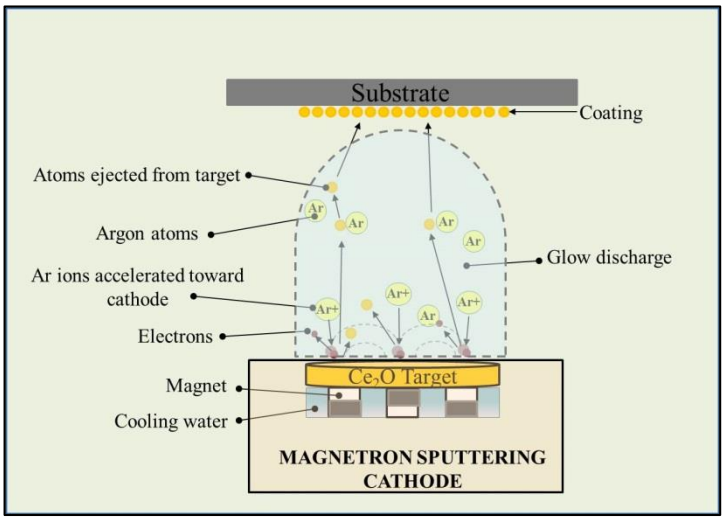

Figure 2.1: Schematic of the magnetron cathode and the sputtering deposition process.

If the electrons have a velocity component perpendicular to the magnetic field, they can spiral around the magnetic field (i.e. electrons become trapped) with a well-defined frequency and radius, which is a function of the strength of the magnetic field [70]. The increased ionisation efficiency due to this method leads to increased ion bombardment on the target and thereby an increased sputtering rate. This also causes a decrease of the plasma impedance which can help magnetrons to operate at much lower voltages than diode/DC systems. Permanent magnets are commonly used in

magnetrons, with several different possible geometries. In addition to the conventional (balanced) type of magnetron assembly, there is another configuration available, known as an unbalanced magnetron. In balanced magnetrons, the plasma is closely confined to the target, up to ~ 60 mm from the target surface. Hence, films deposited within this region will undergo ion bombardment, which can strongly influence the structure and properties of the growing film. Substrates placed out of this region will be in the lower plasma density region, and hence not be affected by sufficient ion bombardment. Contrary to the conventional balanced magnetron type, in an unbalanced system some of the electrons are deliberately allowed to escape from the target surface, by adjusting the magnetic field. Hence, these electrons create plasma closer to the substrate, which helps the reactive gases to reach the substrate surface for reactive sputtering or for ion plating [70]. Depending on the nature of the power supply that is used to drive the magnetron, sputtering includes different types, such as DC sputtering, RF sputtering, pulsed DC sputtering etc.

2.2.1.2 PULSED DC MAGNETRON SPUTTERING

Pulsed DC magnetron sputtering (PDCMS) is a well-developed deposition technique widely used for coating and thin film deposition in industrial applications and has received increased attention in the last number of decades [71, 72]. This development combines the benefits of both DC and RF magnetron sputtering. Even though RF sputtering can make good quality films, the deposition rate is very low (~µm/h range). Moreover, RF sputtering systems are complex and difficult to scale up for industrial applications. Correspondingly, the problems associated with the DC sputtering are intricacy of the deposition process for insulating layers and poor long term stability of non-metallic processes [64]. Furthermore, during

the DC reactive sputtering of an insulating material using a metal target and a reactive gas in Ar plasma, a film of the insulating material will deposit on the surface of the metallic target itself. As the deposition progresses, this insulating layer will charge up positively due to the accumulation of positive ions from plasma, until breakdown occurs in the form of an arc. These arc events can create an ejection of droplets of materials from the target, which is detrimental to the required properties of the growing film.

Additionally, arcing can make rapid changes to the deposition parameters, and thereby change the stoichiometry of the film; it can even damage the magnetron power supply. The problem due to the accumulation of charge can happen in the case of the DC sputtering of insulating targets as well. A photograph of the sputtering system used for the deposition process in this study is presented in Figure 2.2. It consists of a magnetron (A) connected to the sputtering chamber (B), which is separated from a loading chamber (C) by a transfer valve (D). Pulsed magnetron sputtering can be a better choice to overcome many of the problems one comes across with the deposition of the insulating films. It has been reported that pulsing the magnetron discharge in the medium frequency range (20-250 kHz) can significantly reduce the arcing and hence reduce the formation of defects in the film [73]. In addition, it can increase the deposition rate to a value of the order of tens of microns per hour, which is similar to that for pure metal films.

A pulsed magnetron sputtering process usually employs pulsed DC power. It can generate a condition by applying a short positive pulse in between pulses by disrupting the negative voltage to the target to eliminate the chances of arcing. An ENI RPG-100 asymmetric bipolar pulsed power supply is used for the film deposition in this work (Figure 2.3).

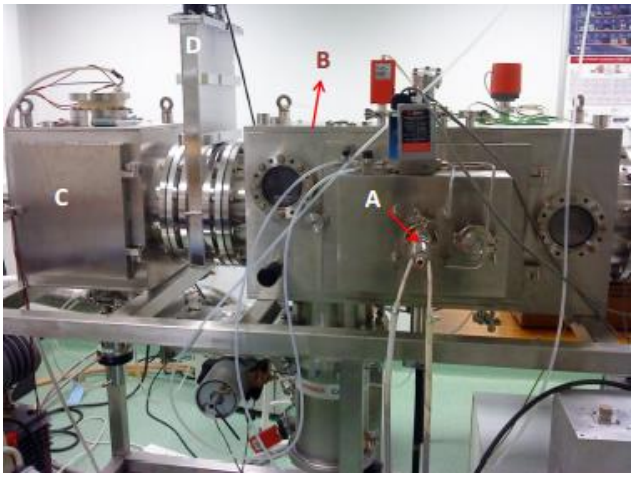

Figure 2.2: Photograph of the sputtering system used for the experiment: A) Magnetron, B) Sputtering chamber, C) Loading chamber and, D) Transfer valve.

It is possible to dissipate the accumulated charges on the insulating layer on the target, completely or partially, through the plasma during the pulse-off period by switching the target voltage to a more positive value. There are two modes of operation: unipolar pulsed sputtering and bipolar pulsed sputtering. In the former, the target is operated between the normal voltage and ground and in the latter; the target voltage is reversed and becomes positive during the pulse-off period. As the mobility of the electrons in the plasma is much higher than the ions, it is usually only essential to reverse the target voltage to between 10% and 20% of the negative operating voltage in order to fully discharge the charged regions and avoid arcing [64].

Figure 2.3: Photograph of the asymmetric bipolar pulsed power supply (ENI RPG-100) used for the deposition.

The bipolar pulsed DC power generates either a bipolar symmetric or a bipolar asymmetric pulse. The schematic of the illustration of the target voltage waveform for a pulsed DC power supply operating in the asymmetric bipolar pulse mode is as shown in Figure 2.4. Pulse parameters, like pulse frequency and pulse duty cycle, have significant influence on the properties of the deposited films.

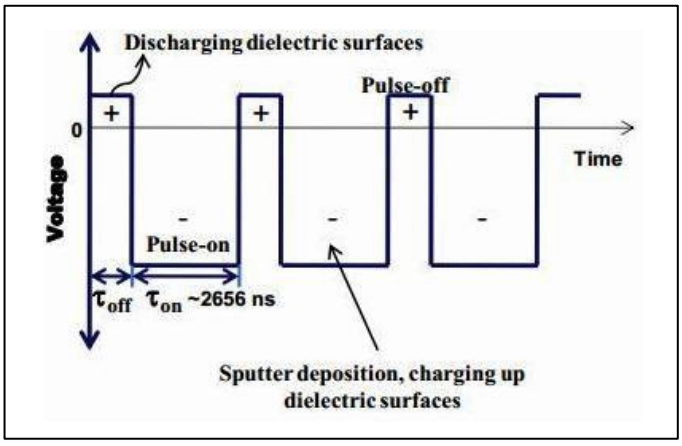

Figure 2.4: Schematic of the asymmetric bipolar pulsed DC signal used for the deposition. The deposition by sputtering of the target on the substrates takes place during the pulse-on time of the pulse.

The pulse duty cycle (δ) can be defined as the relative duration of the pulse on time (τ):

$$\delta = \frac{\tau_{on}}{\tau_{on} + \tau_{off}} \tag{2.1}$$

The duration of the negative polarity to the cathode is represented as the pulse-on time (τ_{on}) and that of the positive polarity is indicated as pulse-off time (τ_{off}). Thus, sputtering of the target material occurs during the pulse-on time and the discharging of the accumulated charge through the plasma takes place during pulse-off time [74].

In this thesis, the sputtered CeO_2 films were prepared in a PDCMS system fitted with a CeO_2 target (99.99% purity, Kurt J. Lesker Company). The sputtering process was performed under pure argon (Ar) ambient

(unless otherwise stated) with a working pressure of 0.7 Pa for the duration of 60 minutes. A sputtering power of 65 W at 150 kHz without intentional heating, with a target to substrate distance of 60 mm, was used to deposit uniform CeO_2 films of thickness 50 ± 10 nm.

2.2.2 SPIN COATING DEPOSITION

The spin coating process is a very useful technique owing to its versatility, effectiveness, and practicality. It has been used for several decades for the realisation of thin films. The operation can be done in ambient conditions and thus a vacuum system is not required. A typical spin coating process involves depositing a small puddle of a chemical solution resin onto the centre of a substrate followed by spinning the substrate at high speed, typically 3000 rpm. The centripetal acceleration will cause the chemical solution resin to spread to, and eventually off, the edge of the substrate. As the spin process continues, evaporation of the chemical solution takes place leaving behind a thin film on the substrate surface (see Figure 2.5).

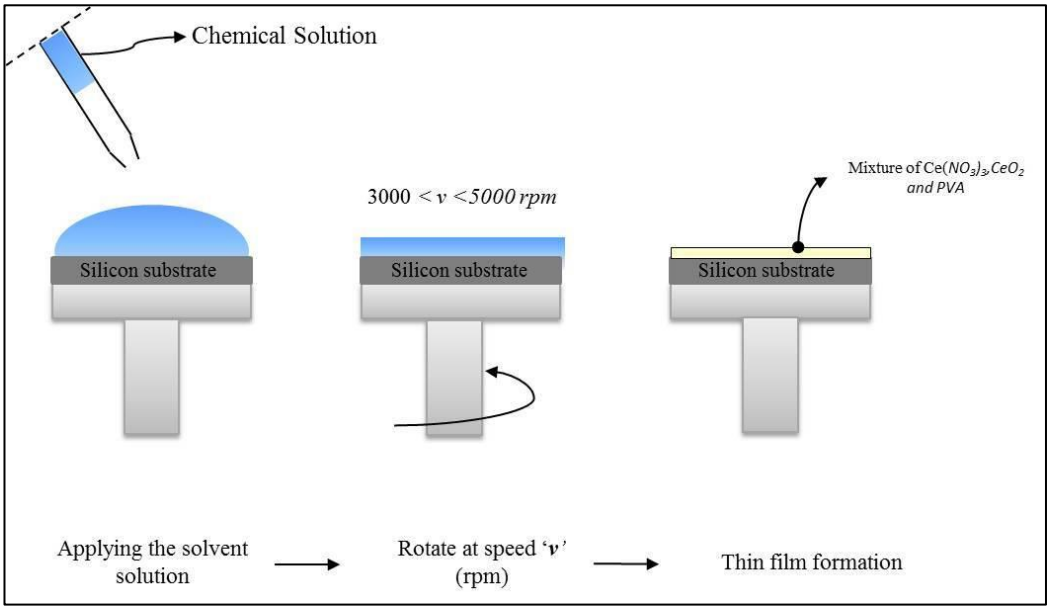

Figure 2.5: Schematic of the chemical solution spin coating process.

In many chemical solutions used for spin coating, rapid solvent evaporation is a problem; therefore, accelerating the substrate from rest to the final spinning speed is highly important. Moreover, the final film thickness and other film properties depend on the nature of the chemical solution (viscosity, drying rate, surface tension, etc.) and the parameters (rotational speed, acceleration and fume exhaust) chosen for the spin coating process. The chemical solution used for the spin-coating deposition to obtain the CeO_2 films is prepared by placing 2g of cerium (III) nitrate hexahydrate ($Ce(NO_3)_3.6H_2O$, 99% purity, purchased from Sigma-Aldrich) and 0.2g of 10% polyvinyl alcohol (PVA) in 20 ml de-ionised water (DI H_2O). The solution is then stirred, using a magnetic stirrer, for three hours to ensure a complete dissolution. This fully dissolved chemical solution is then used to deposit a small puddle (~ 1 ml) onto the centre of the clean Si (100) substrates prior to spin coating deposition of CeO_2 films. The spin coating deposition system used to fabricate the CeO_2 is from the Laurell Technologies Corporation.

2.3 CHARACTERISATION TECHNIQUES

2.3.1 X-RAY DIFFRACTION

X-ray diffraction (XRD) is a versatile, non-destructive technique widely used to analyse the crystal structure of materials. It is also an indispensable method for obtaining valuable information about the material such as phase analysis, texture analysis and grain size which assist in understanding sample quality.

XRD passes a beam of x-ray of a known wavelength through a sample. When the beam of x-ray is incident on a crystalline sample, it is scattered by atomic planes in all directions. The three dimensional lattice of a crystalline

material consists of repeated planes of atoms arranged in a regular manner. Inter atomic distances in crystalline solids are of the order of a few Ångstroms and the wavelength of the x-ray is also of the same order. When a beam of x-ray interacts with these atomic planes, it gets scattered. In some of these directions, the scattering beams from the planes, with a distance of separation (d) analogous to the known wavelength of the x-ray, of the sample are completely in phase and these beams constructively interfere and reinforce one another to form diffracted beams. The variation of the scattered signal with x-ray angle forms a diffraction pattern. These diffraction patterns act as a fingerprint for that particular material under examination.

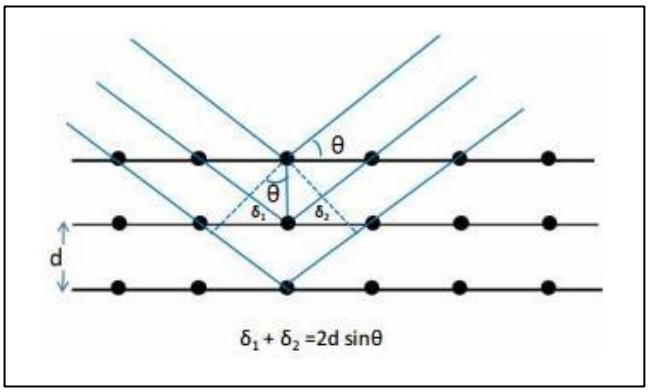

Figure 2.6: Illustration of Bragg's law. The figure indicates the conditions for the occurrence of Bragg diffraction. Planes of atoms are indicated using the black solid lines.

The essential condition for the occurrence of diffraction pattern (Figure 2.6) is developed by English physicists Sir W.H. Bragg and his son Sir W.L. Bragg. It is given by:

$$n\lambda = 2d\sin\theta \tag{2.2}$$

n is the order of reflection, λ is the wavelength of the x-ray used, d is the inter-planar distance and θ is the angle of incidence and reflection of x-ray. The structure of the CeO_2 thin films are examined using a Bruker Advance D8 XRD instrument (see Figure 2.7) with a CuKα monochromatic

radiation beam (λ = 1.54 Å) produced in an x-ray tube operated at 40 kV and 40 mA. The scanning range (2θ) is performed from 20^{o} to 60^{o} with a step size of 0.1°.

In this present work, XRD is used to assess the quality of the CeO_2 samples by reviewing the crystallinity and phase purity of CeO_2 thin films as well as the sample crystallographic properties, such as crystallite size and lattice parameters.

Figure 2.7: Photograph of Bruker AXS Advance D8 XRD system.

2.3.2 SCANNING ELECTRON MICROSCOPY

Scanning Electron Microscopy (SEM) is one of the most adaptable types of electron microscopy for the investigation of surface topography and chemical composition of materials. The SEM is developed to overcome the limitations of the optical microscope such as resolution of ~ 2000 Å. The crucial advantage of SEM over the ordinary optical microscope is its significantly higher magnification (>100,000X) and resolution of ~ 100 Å, which results from the use of an electron beam for imaging as opposed to visible light.

In SEM (Figure 2.8), a high energy beam of electrons produced by an electron gun is focused in high vacuum into a fine probe that is raster scanned over the surface to be examined. This electron beam passes through objective lenses and scan coils that deflect the beam vertically and horizontally so that the electron beam can scan the sample surface. As the electrons interact with the sample surface, a number of interactions occur which results in the emission of electrons (or photons) from (or through) the surface. These emissions are detected and analysed to give point by point information about the surface which is then built up to form the sample image. Secondary electrons are ejected from the surface atoms by inelastic scattering with the beam electrons and these are the main emission signal, which can then be collected by appropriate detectors to yield information about the topography, composition and crystallography of the material under investigation. These emitted electrons are detected and analysed to give an image of the surface. The resolution of the SEM is dependent on the beam spot size, which depends on the wavelength of the electron and the lenses and aberrations in the electro-optic system that produces the electron beam. The samples need to be conductive to be imaged in the SEM because of the combined effects of the incident electron beam and the loss of electrons from the sample and the consequent potential for charging effects for non-conductive samples.

Figure 2.9 shows the generation of various signals as a result of the interaction of the sample atoms with the incoming electron beam. These consist of secondary electrons (used to form images of the sample surface and visualise topography), back scattered electrons (used to identify regions of the sample that differ in atomic composition, as this difference shows up as a variation in the contrast of the sample image during the SEM's raster scan.), transmitted electrons (which can be used in a scanning transmission electron microscope), x-ray, heat, photons etc. As stated above, the creation

of secondary electrons is strongly related to the topography of the sample. Similarly, the creation of the backscattered electrons varies with sample's atomic number.

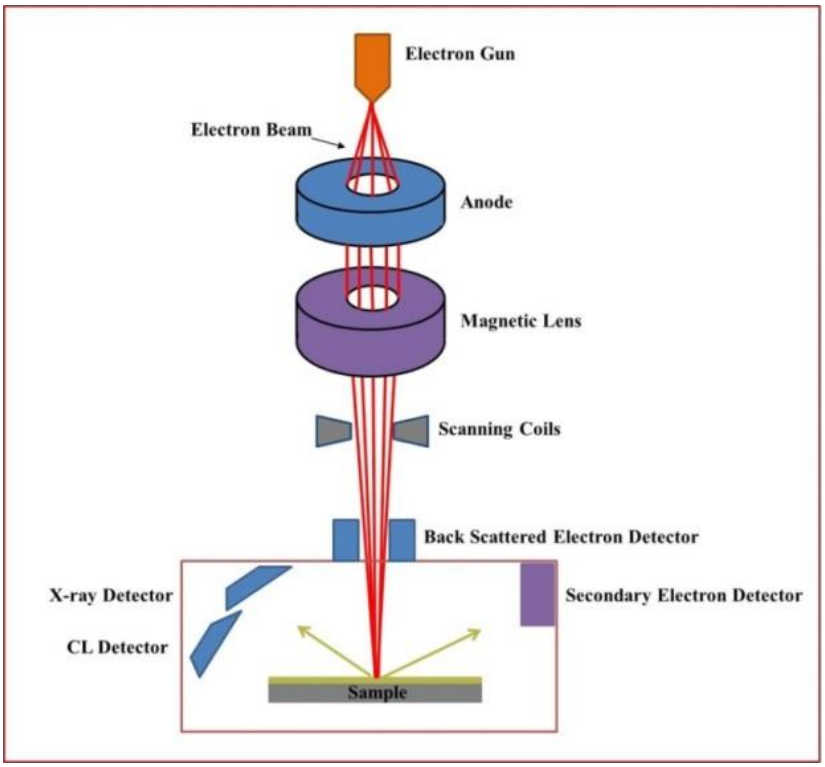

Figure 2.8: Schematic of a SEM system. The electron gun and the lensing system to focus the electron beam on to the sample surface are illustrated.

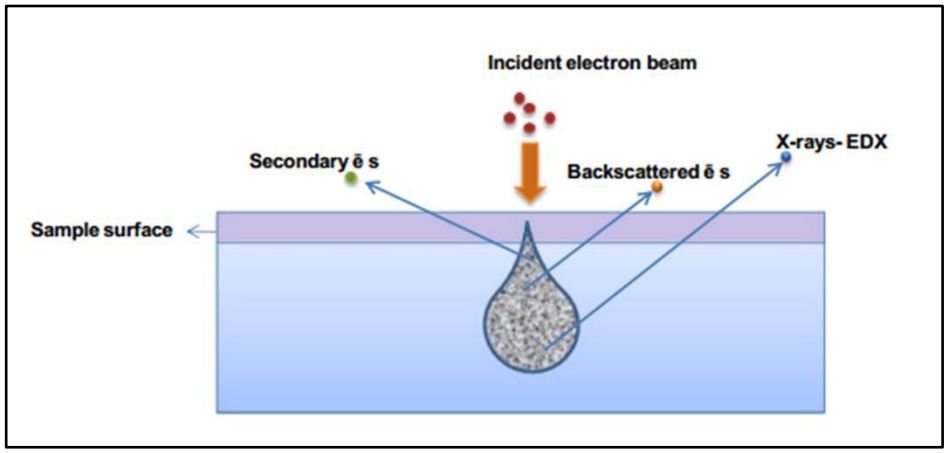

Figure 2.9: Illustration of the different signals generated by the electron beam-specimen interaction in SEM and the regions from which the signals can be detected [74].

The SEM used to analyse the CeO_2 thin films and nanostructures in this study is a Carl Zeiss EVO LS-15 SEM system (see Figure 2.10) fitted with secondary electron, backscattered electron and EDX (further described in section 2.3.3) detectors. This system consists of two chambers under vacuum, **i**) the upper chamber containing the electron gun column, and **ii**) the lower chamber consisting of the sample holder, stage and stage control, where the lower chamber can be brought to atmosphere without breaking vacuum in the upper chamber. This is done by using a differential pumping system with pressure limiting apertures.

Figure 2.10: Photograph of the Zeiss EVO LS-15 SEM system.

2.3.3 ENERGY DISPERSIVE X-RAY SPECTROSCOPY

Energy dispersive x-ray spectroscopy (EDX or EDS), generally called micro analysis, is an analytical technique used for elemental analysis of the sample material. As described in section 2.3.2, electrons are emitted due to the interaction of the electron beam with the sample surface during the SEM analysis. These interactions of the primary beam electrons on the sample surface can give rise to the ejection of the inner shell electrons of the sample,

and transitions of the outer electrons to fill up these vacancies in the inner shells causing the production of characteristic x-rays. The x-ray signals form a finger print of the elements present in the sample which are then collected by the EDX spectrometer to provide an elemental analysis using the x-ray peak intensity and spectral position information with the help of the software associated with the system. The elemental analysis of the CeO_2 samples is investigated using INCAx-act detector attached to the Carl Zeiss EVO LS-15 SEM system.

2.3.4 SPECTROSCOPIC ELLIPSOMETRY

Spectroscopic ellipsometry is a non-destructive, optical analysis technique used to characterise thin films. It determines optical constants (refractive index, extinction coefficient, etc.), surface and interfacial roughness and thin film thickness (for single or multiple layers). Ellipsometry means measuring an ellipse. Linearly polarised light reflecting from a flat surface generally becomes elliptically polarised after reflection. As the light reflects from the material surface, it is polarised in two directions, parallel and perpendicular to the plane of incidence. These are denoted as p-polarised and s-polarised, respectively. This change in the polarisation state of the light reflected from the sample surface is measured as the complex ratio (ρ) of s- and p-polarised reflectances (r_s and r_p respectively) and can be analysed to obtain various information about the material of the sample. The measured value is expressed in terms of the ellipsometric angles Ψ (psi) and Δ (delta), where the angles Ψ and Δ represent the change in phase and amplitude, respectively, between the s- and p-polarised that occur upon reflection and, are related to the ratio (ρ) of the Fresnel reflection coefficients r_s and r_p in Equation 2.3. In Equation 2.5, δ_s and δ_p refer to the relative phase of these components.

$$\rho = \frac{r_p}{r_s} = \tan(\Psi)\, e^{i\Delta} \tag{2.3}$$

where

$$\tan(\Psi) = \frac{|r_p|}{|r_s|} = |p| \tag{2.4}$$

and

$$\Delta = \delta_p - \delta_s \tag{2.5}$$

Since ellipsometry measures the ratio of two values, this technique provides highly accurate, very reproducible measurements that are not dependent on the incident beam intensity. In this work, the average layer thickness of the CeO_2 thin films on Si (100) wafers is measured with a J. A. Woollam Co., Inc. M-2000UI ellipsometer, Model XLS - 100 and controlled by EASE™ (version 1.16). A schematic of the ellipsometry system used is shown in Figure 2.11.

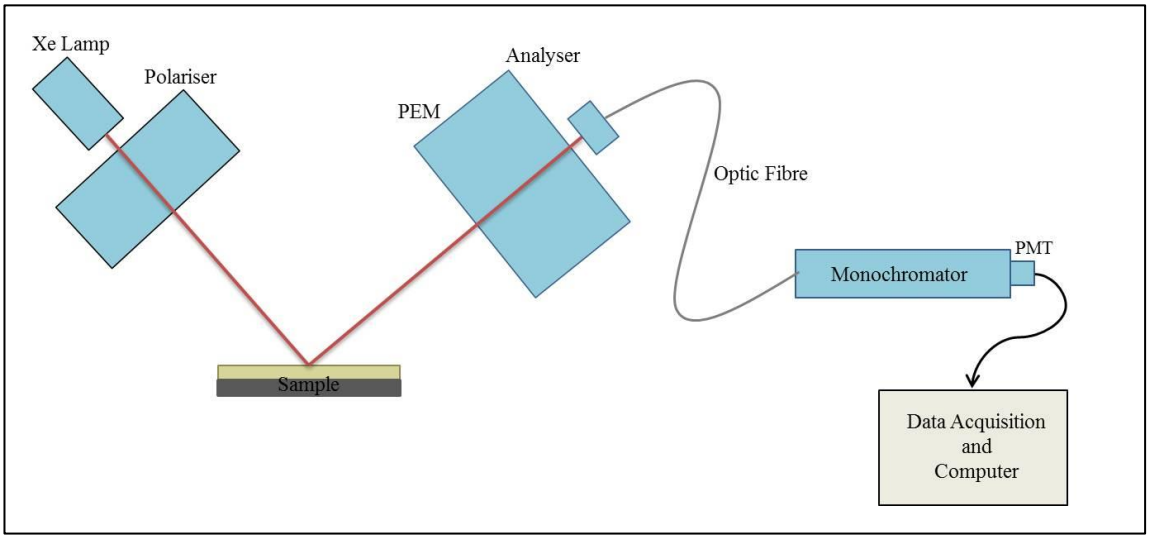

Figure 2.11: Schematic of the spectroscopic ellipsometry system.

2.3.5 ATOMIC FORCE MICROSCOPY

An atomic force microscope (AFM) is optimized for measuring surface features that are extremely small, such as that of a carbon atom (approximately 0.25 nm). It was developed by Gerd Binnig in 1986 as a method to overcome the serious limitations of the scanning tunnel microscope (STM) [75]. An AFM can be used to image any material's surface and unlike a STM it does not require the surface to be conductive. During the scanning of a sample using the atomic force microscope a constant force is applied to the surface. This force is controlled by the probe at the end of the cantilever. When performing the scanning, measuring the force with the cantilever in the AFM is achieved by two techniques. In the first technique the deflection of the cantilever is directly measured, while the second technique vibrates the cantilever and the changes in the vibration properties are measured.

A standard AFM instrument consists of a laser focused onto the upper surface of a small cantilever. The cantilever in turn is mounted on piezo crystals in a tripod configuration that allows the cantilever to be moved in the X, Y and Z directions. The laser spot focused on the cantilever is reflected towards a mirror which then directs the beam to a split photodiode detector. Movement of the cantilever is then detected as a shift in the detection signal from the split photodiode. Figure 2.12(a) shows a typical AFM configuration while Figure 2.12(b) shows the effect of the cantilever movement on the laser beam path during measurement.

In this thesis work, the surface morphology and surface roughness of the CeO_2 films, prepared under different conditions, are investigated using a Veeco Nanoscope Dimension 3100 AFM instrument operating in tapping mode using aluminium-coated silicon (Si) AFM probes (Tap300Al-G, purchased from Budget Sensors), for all the AFM imaging. These probes

operated at a resonant frequency and force constant of 300 kHz and 40 N/m, respectively.

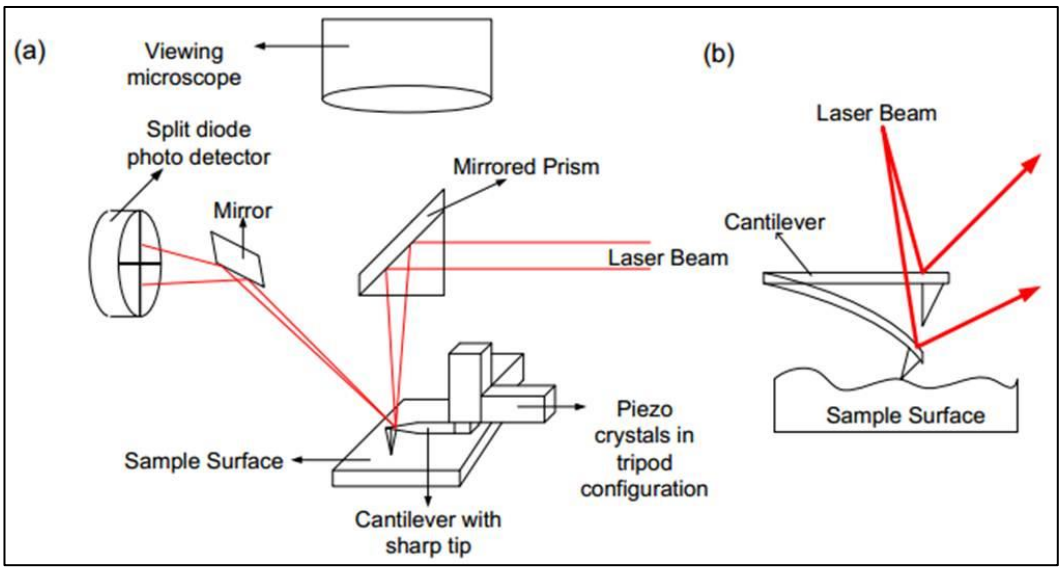

Figure 2.12: (a) Schematic representation of a typical AFM instrument, (b) a schematic representation of the effect of bending the cantilever on the laser beam path during tapping mode oscillations [76].

2.3.6 X-RAY PHOTOELECTRON SPECTROSCOPY

Photoelectron spectroscopy (photoemission spectroscopy, XPS) is a characterisation technique that is extremely sensitive to surface chemistry, allowing surface chemical state information to be examined. It is a well-known method used for the investigation of the electronic structure of atoms and molecules. It is developed by Kai Siegbahn and his group in the 1960's [77]. Surface analysis using XPS can be realised by the irradiation of the samples with mono-energetic soft x-rays followed by the analysis of the kinetic energy of the electrons directly ejected (without subsequent scattering or energy loss) as a result of the photoelectric effect, and the deduction of the electron binding energy in the material from the kinetic energy using the Einstein equation. A typical XPS spectrum is a plot of the electron binding

energy as determined from the kinetic energy of the emitted electron versus the number of electrons detected at this energy.

In order to accurately measure the kinetic energy of the photoemitted electrons from a chemically stable surface, as well as ensuring the detection of a significant number of the photoemitted electrons, experiments are performed under ultra-high vacuum (UHV) environments; where UHV is defined as pressures lower than 10^{-9} mbar. Another reason for the importance of UHV is to minimise sample contamination. As XPS is limited to an approximate sampling depth of 4 to 7 nm [78], depending on material, it is important to ensure the sample being measured has minimal environmental contamination, such as the presence of environmental carbon on the surface. Since the surfaces are the prime region of investigation by XPS, the surface reconstruction can be altered by the adsorption of contaminants. Surface contamination also complicates controlled systematic investigations such as anneal or deposition studies. Therefore a UHV environment ensures that the surface under investigation remains chemically stable during the photoemission experiment.

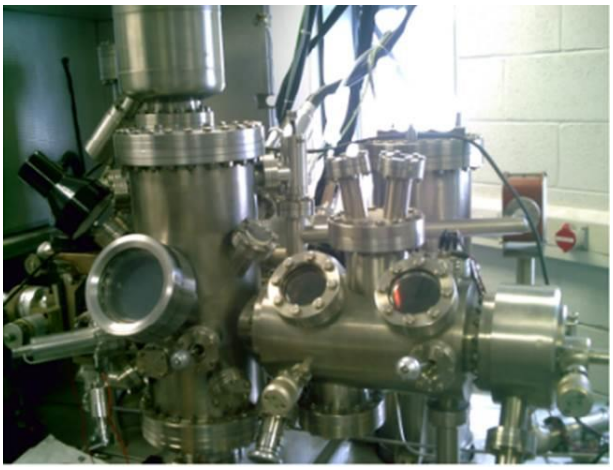

Figure 2.13: Photograph of dedicated three chambered XPS system.

In this work, a detailed chemical analysis of the CeO_2 film surfaces is carried out using the VG Microtech electron spectrometer (see Figure 2.13) at

a base pressure of 10^{-9} mbar. The photoelectrons are excited with a conventional Mg Kα (hv = 1253.6 eV) x-ray source and an electron energy analyser operating at a 20 eV pass energy, yielding an overall resolution of 1.2 eV. The samples are subjected to a mild degassing procedure in UHV at 300 °C in order to eliminate any surface contamination (this treatment is at too low a temperature to affect the properties being studied as a function of post deposition annealing), which may have arisen as a result of the transfer in atmosphere between the deposition and analysis chambers. All XPS spectra are collected and peak fitted by Dr Anthony McCoy in the School of Physical Science, Dublin City University, Ireland.

2.3.7 SECONDARY ION MASS SPECTROMETRY

Secondary ion mass spectrometry (SIMS) is one of the most appealing physical methods used to provide specific chemical information about solid surfaces and thin films. The surface of the samples is bombarded using a high energy focused ion beam, which causes sputtering of the sample (see Figure 2.14). The ejected secondary ions are then collected and analysed using a mass spectrometer. The composition of the sample can be extracted from the information on the count rate of different secondary ion species ejected from the sample. It is a very sensitive technique and allows measurements of trace elements at very low concentration (ppb).

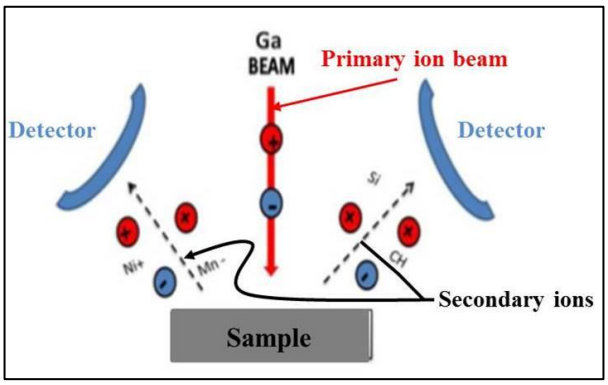

Figure 2.14: Schematic of the SIMS analysis.

The CeO_2 sample studies are carried out using a bench-top secondary ion mass spectrometer fitted with a quadrupole mass analyser apparatus called the Millbrook MiniSIMS Alpha and developed by Millbrook Instruments Ltd (Figure 2.15). It incorporates a raster scanned gallium (Ga) liquid metal ion gun for the primary beam and low-energy optics for secondary ion extraction into a 300 Dalton (Da) quadrupole mass spectrometer. Ga^+ ions (6 keV) are focussed perpendicularly to the sample. As the CeO_2 samples charge up when it is being studied without charge neutralisation, an electron gun charge neutralisation was used during all the measurements. SIMS needs a high vacuum of the order of 10^{-5} Pa in order to minimise both the collision of the ejected secondary ions with the background gas and surface contamination of the samples due to the adsorption of the background gas during the measurements. The operating pressure used is 3.1×10^{-5} Pa.

Figure 2.15: The Millbrook MiniSIMS Alpha system.

2.3.8 THERMOGRAVIMETRIC ANALYSIS

Thermogravimetric Analysis (TGA) is a technique in which the mass of a substance is monitored as a function of temperature or time as the sample specimen is subjected to a controlled temperature program in a controlled atmosphere. A TGA consists of a sample holder that is supported by a

precision balance. That sample holder resides in a furnace and is heated or cooled during the experiment. The mass of the sample is monitored during the experiment and a purge gas controls the sample environment. This gas may be inert or a reactive gas that flows over the sample and exits through an exhaust.

In this thesis work, TGA is performed using Setaram SetSys 16/18 instrument (sensitivity 0.4 μg). Each TGA sample consisted of several pieces of CeO_2 film covered substrate placed in an alumina crucible. The initial total masses of the samples are in the range 140 - 210 mg. The experimental procedure included heating the sample in air to 600 °C, equilibration at this temperature with air for 3 hours, flushing with Ar for 1 hour, and then reduction in a flow of 10% H_2 – N_2 mixture for 5 h. The thermogravimetric data are corrected for buoyancy effects by subtracting a baseline recorded under identical conditions using an inert alumina reference sample. The O_2 partial pressure in the 10% H_2 – N_2 mixture at 600 °C corresponded to ~10^{-21} Pa. Thermogravimetric data are performed by Dr Aleksey A. Yaremchenko and Dr Rajesh Surendran in the Department of Materials and Ceramic Engineering, CICECO, University of Aveiro, Portugal.

2.3.9 ELECTROCHEMICAL CYCLIC VOLTAMMETRY

Cyclic voltammetry (CV), also known as linear sweep voltammetry, is one of the most versatile techniques available for acquiring qualitative information about electrochemical reactions. This technique is first introduced by Matheson and Nichols in 1938, and independently advanced and theoretically described by Randles and Sevcik ten years later [79]. Cyclic voltammetry has become a powerful technique due to its ability to provide substantial information promptly on the thermodynamics of redox processes, both on the kinetic of heterogeneous electron-transfer reactions and on the

coupled chemical reactions and adsorption processes [80]. A typical cyclic voltammogram for a reversible single electrode transfer reaction is shown in Figure 2.16, with a solution containing only a single electrochemical reactant. The cyclic voltammogram shows the influence of voltage scan rate on the current for a reversible electron transfer reaction.

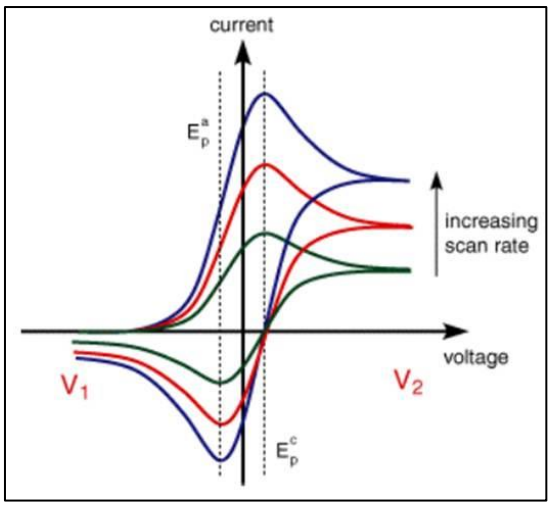

Figure 2.16: Scan rate and rate constant dependence of the I-V curves [81].

In this thesis electrochemical measurements are conducted using CH Instruments 660 potentiostat in anhydrous N,N-Dimethylformamide (DMF) solution with 1 M $LiClO_4$ as a supporting electrolyte, unless otherwise stated. A typical three-electrode cell configuration is used with cerium oxide (CeO_2) coated ITO glass as the working electrode and two platinum electrodes, one acting as counter electrode and the other as a pseudo reference electrode (see Figure 2.17). The active area of the working electrode is maintained constant at 1.44 cm^2 (1.2 cm x 1.2 cm). All potentials have been standardized and quoted versus the SCE reference electrode. All chemical and solvents used for electrochemical measurements are purchased from Sigma-Aldrich and are of analytical grade. All solutions are deoxygenated for 30 minutes using nitrogen gas prior to use. All measurements are carried out at room temperature, 22 ± 2 °C. Electrochemical cyclic voltammetry is completed

with the help of Dr Anita Venkatanarayanan from the Biomedical Diagnostics Institute, School of Chemical Sciences, Dublin City University, Ireland.

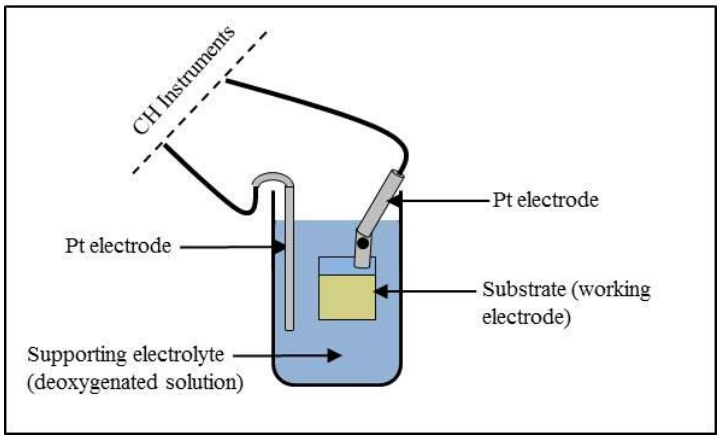

Figure 2.17: Schematic of the cyclic voltammetry three-electrode cell configuration.

2.3.10 ULTRAVIOLET-VISIBLE SPECTROSCOPY

Ultraviolet-visible absorption spectroscopy (UV-Vis) is a technique used to perform optical absorption measurement as a function of wavelength due to its interaction with a material. It examines the optical absorption of radiation and it is one of the most common methods for investigating the energy level structure of materials. From the semiconductor point of view, it is a simple method for the determination of the bandgap value of the material. Here, the optical absorption properties of the CeO_2 and CeO_2-coated ZnO samples are studied at room temperature using a Perkin Elmer Lambda 40 UV–Vis spectrometer (see Figure 2.18) in the wavelength range from 400 to 800 nm with a resolution of 4 nm.

Figure 2.18: Photograph of the Perkin Elmer Lambda 40 UV-Vis spectrometer.

2.3.11 PHOTOLUMINESCENCE

The emission of radiation from a material by providing some form of energy for excitation is generally referred to as luminescence. Photoluminescence (PL) is an extremely sensitive technique used to characterise optoelectronic semiconductor materials. During PL measurements, luminescence happens due to excitation produced by the absorption of photons. It is an extensively used method to examine the electronic structure, photochemical and optical properties of semiconductor materials. PL involves the impingement on the sample by photons of an energy value greater than the bandgap value (E_g) of the sample material. The irradiation of photons with sufficient energy can create electrons in the conduction band and holes in the valence band. If the relaxation of these excited electrons is radiative, then the process is called photoluminescence. In this study, the following two PL spectroscopies are used:

1) Temperature dependent PL measurements are carried out on CeO_2 samples using a closed cycle helium cryostat and a 325 nm line of a HeCd laser operating at a power less than 200 mW. The luminescence is analysed using a 1m grating spectrometer (SPEX 1704) with a photomultiplier tube (Hamamatsu model R3310-02) in

photon counting mode and cooled to 20°C by a Peltier system EMI FACT50 Cooler (see Figure 2.19).

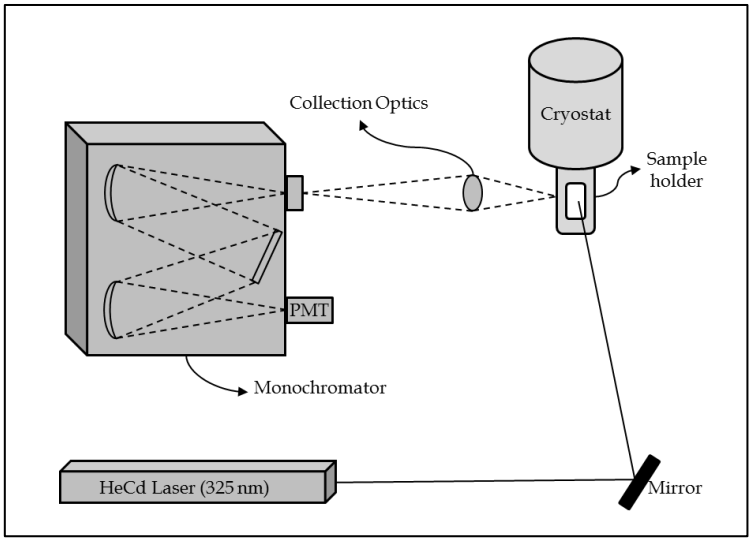

Figure 2.19: Schematic of the PL experimental set-up.

2) Room temperature PL measurements are carried out on CeO_2 and CeO_2-coated ZnO samples using a 244 nm (~ 5.1 eV) excitation produced by an Ar ion Innova laser from 20K to room temperature. The luminescence is recorded using TRIAX 190 Jobin Yvon-Horiba spectrometer with a resolution of 0.3 nm.

Chapter 3

MAGNETRON SPUTTERING GROWTH AND CHARACTERISATION

3.1 INTRODUCTION

As mentioned previously, CeO_2 and CeO_2-based materials have attracted enormous interest industrially; in particular for their OSC. This is due to the fact that CeO_2 can oxidise and reduce molecules which interact with its surfaces and thus oxygen vacancy defects can be rapidly formed and eliminated, giving CeO_2 its high OSC [82]. This capacity makes various modern devices containing CeO_2 much more effective than their predecessors without CeO_2. The presence of CeO_2 contributes significantly to the effectiveness of three-way catalysts [83], catalysts for H_2 production from fuel [84], optical films [85], oxygen sensors [42] and thermochemical two-step water-splitting cycle [2]. Apart from the ability of CeO_2 to easily and repeatedly switch between oxidation states and accommodate different levels of surface and bulk oxygen vacancies [44], the abundance of metallic

Ce on earth makes CeO_2 a low-cost and highly attractive material for applications in solar cells and photocatalysis. CeO_2 has a cubic fluorite-type crystal structure, with a lattice spacing of 0.5411 nm, and unique material properties such as high dielectric constant, high refractive index and excellent stability at high temperatures [86, 87]. The valence of the Ce ion is very important in determining the structure of cerium oxides; trivalent Ce forms the sesquioxide Ce_2O_3, which has a hexagonal lattice ($P\bar{3}m1$ space group), while tetravalent Ce forms CeO_2, which has a cubic fluorite lattice (Fm3m space group) [45, 89, 90]. Thin films of CeO_2 (the most common form of oxidised cerium) exhibit unique physical properties, such as a lattice constant similar to that of Si (α = 0.541 nm), a high refractive index and dielectric constant [87, 91]. Hence, CeO_2 films are also appropriate for many applications in optical devices [92, 93], microelectronic devices [94, 95], optoelectronic devices [96] and sensors [42]. In addition CeO_2 is a non-toxic and stable material with a wide band gap and can demonstrate high ionic conductivity if doped with aliovalent cations [88].

CeO_2 in bulky and porous structures are widely used in many applications related to the material's enhanced catalytic behaviour and redox properties as mentioned above. Likewise, thin films can be incorporated in the same catalytic activities through the creation of thick porous CeO_2 structures by effectively incorporating porosity between intermediate thin film layers [97, 98], where an understanding and enhancement of the oxygen storage properties of the thin films are essential. Therefore, using thin films with higher OSC to create the bulk porous structures would effectively enhance the performance of the final structure. Additionally, since the physical and chemical properties of CeO_2 can be tuned by doping, these CeO_2 thin films can be doped with materials such as SiO_2, TiO_2 or ZrO_2 in order to improve and further support the thermal stability and oxygen storage (redox) properties of CeO_2 [44].

Since CeO_2 is stable, even in sub-stoichiometric form ($CeO_{2-\delta}$), it has been produced by several growth techniques including sol-gel deposition [99], electron-beam evaporation [100], laser ablation [101], molecular beam epitaxy [102], chemical vapour deposition [95], ion-beam-assisted deposition [103, 104], pulsed laser deposition [105] and reactive and non-reactive magnetron sputtering [91, 106], which is one of the best methods for the preparation of CeO_2 films due to its many advantages [91, 107]. These include low substrate temperature, good surface roughness characteristics and scalability, as well as being a well-established and relatively low cost industrial technique. The bipolar PDCMS process has recently attracted a great deal of attention because it shows higher deposition rates of defect-free ceramic films than the more conventional RF magnetron sputtering process (as mentioned in Chapter 2). In particular it can alleviate the occurrence of arcing events at the oxide targets involved in the continuous DC sputtering process. The creation of pulses in the magnetron discharge in the mid-frequency range has been found to prevent arc events and stabilise the reactive sputtering process. Thus, PDCMS is a commercially suitable method for large-area deposition of good quality ceramic films with high yield under various processing conditions.

Many reports have addressed the electrochemical, redox and oxygen storage properties of CeO_2 [108-110]. For example, Wang et al. [111] introduced a simple OSC measurement technique using cyclic thermogravimetric analysis where the mass changes of the CeO_2 samples, using extra low-temperature, are measured and correlated to OSC. Other groups have also reported on the electrochemical properties and charge storage of CeO_2 such as Brezesinski et al.'s report [97] on enhancement in the electrochemical charge storage capacity of the mesoporous ceria compared to bulk ceria and on the oxidation state of Ce in CeO_2 using XPS [108, 112, 113]. Park et al. [114] reported the first studies of CeO_2 films deposited by PDCMS

where comparative studies of the microstructure and mechanical properties of deposited films are carried out.

In this chapter, a reliable method for the deposition of stable CeO_2 thin films using PDCMS has been successfully demonstrated. A uniform film thickness of 50 ±10 nm is obtained for all the deposited samples. The effect of two sputtering gas ambients on the electrochemical and oxygen storage properties has been studied and the following key conclusions have been reached on the basis of our results. Firstly, deposition of nanostructured CeO_2 thin films by PDCMS is successfully achieved. Secondly, the deposition gas ambient influenced the film stoichiometry, surface morphology and crystallinity of the CeO_2 films. Thirdly, a relative oxygen deficiency in the sample sputtered in Ar has been confirmed by AFM, SIMS, XPS, CV and TGA. Finally, electrochemical measurements and TGA analysis both indicate that CeO_2 samples sputtered in Ar have a higher CSC and OSC than those deposited in the presence of O_2, making CeO_2 samples sputtered in Ar better suited for many applications.

3.2 EXPERIMENTAL METHODS

Nanostructured CeO_2 thin films are prepared on Si(100) and ITO coated glass substrates by PDCMS from CeO_2 target (99.99% purity). The sputtering target was supplied by the Kurt J. Lesker Company. Prior to growth, the substrates were cleaned using acetone and decontamination foam followed by deionised (DI) water (obtained from a Millipore filtration system) to remove surface impurities. An ENI RPF-100 pulse generator is used to drive a planar magnetron fitted with the target in the power regulation mode. The chamber is first pumped down to a base pressure of 2×10^{-7} mbar (2×10^{-5} Pa) by cryogenic pumping. The target is pre-sputtered for about 10 minutes prior to deposition in order to eliminate target surface contamination and to

obtain a stable plasma density. Sputtering is then performed under either pure Ar ambient or an Ar/O_2 mixed ambient and the working pressure is adjusted and kept at 7×10^{-3} mbar (0.7 Pa) for the duration of deposition in both cases. The Ar:O_2 partial pressure ratio in the Ar/O_2 mixed ambient is 2:1.The target to substrate distance is adjusted to 60 mm. The sputtering is completed with a power of 65 W at 150 kHz without intentional heating. The substrates are held at floating potential and the sputtering time is adjusted to 60 minutes to obtain a uniform film thickness of 50 ± 10 nm for all the samples grown (thicknesses are measured using spectroscopic ellipsometry post film growth).

The crystallographic structure of the deposited CeO_2 films is determined using XRD. The surface morphology and roughness of the CeO_2 films were studied by AFM operating in tapping mode with a tip radius of < 10 nm. Detailed chemical analyses of the CeO_2 films is performed using XPS while the elemental nature of the films are investigated using SIMS. Electrochemical measurements are conducted using CV in anhydrous N, N-Dimethylformamide solution with 1 M $LiClO_4$ as the supporting electrolyte unless otherwise stated. The OSC of the CeO_2 films is investigated using TGA. Further details on these characterisation techniques are provided in Chapter 2.

3.3 RESULTS AND DISCUSSION

As discussed in chapter 2, the freedom to freely vary the sputtering parameters to improve the quality of the deposited films is very wide in the case of PDCMS, compared to other types of sputtering methods. The selection of suitable sputtering parameters for the development of good quality CeO_2 films was performed after several repetitions of the experiments, with varying sputtering parameters. The optimisation of the

process conditions was established by observing the structural, morphological and optical properties of the films. The pulse duty cycle and other variables such as sputtering pressure, target power and target substrate distance etc. had to be optimised. An optimised pulsed power of 65 W was used for the preparation of the films due to the fact that, as the power increases to the range of 70-75 W, the deposition rate increases, but there is significant target heating. This even caused the CeO_2 target sides to crack after repeated sputtering as a result of the uneven heat through the ceramic target.

The working gas pressure of the sputtering chamber also had an effect on the scattering of the sputtered species from the target and thereby on the properties of the deposited films. The sputtering pressure was optimised to a value of 7×10^{-3} mbar (as mentioned above), by observing the structural, morphological and optical properties of the deposited films. Once the sputtering parameters were optimised, two distinct studies were carried out:

1) Control and enhancement of the oxygen storage capacity of CeO_2 films by variation of the deposition gas atmosphere during PDCMS (described and discussed in this chapter).

2) Control of crystal structure, morphology and optical properties of the CeO_2 films by post-deposition annealing temperatures (a detailed account of this study is given in Chapter 4).

3.3.1 STRUCTURAL & MORPHOLOGICAL STUDIES

Figure 3.1 shows the θ-2θ XRD patterns in a locked-coupled (θ-2θ) mode of the as-deposited nanostructured CeO_2 films deposited in a pure Ar and Ar/O_2 mixed ambients, in a 2θ range from 25° to 60°. The sample deposited in a pure Ar ambient is clearly amorphous and shows no presence of any

CeO_2 peaks. On the other hand, the sample deposited in an Ar/O_2 mixed ambient shows a polycrystalline structured CeO_2 film (cubic fluorite, JCPDS No.: 34-0394) that clearly exhibits the presence of CeO_2 (111), (200), (220) and (311) reflections, with predominant texture along the [111] direction and with no indication of other phases. These diffraction peaks are in good agreement with the standard CeO_2 patterns [115-117]. There is also a single weak peak at $2\theta = 46.6°$ that is assigned to the hexagonal Ce_2O_3 phase (JCPDS No.: 23-1048).

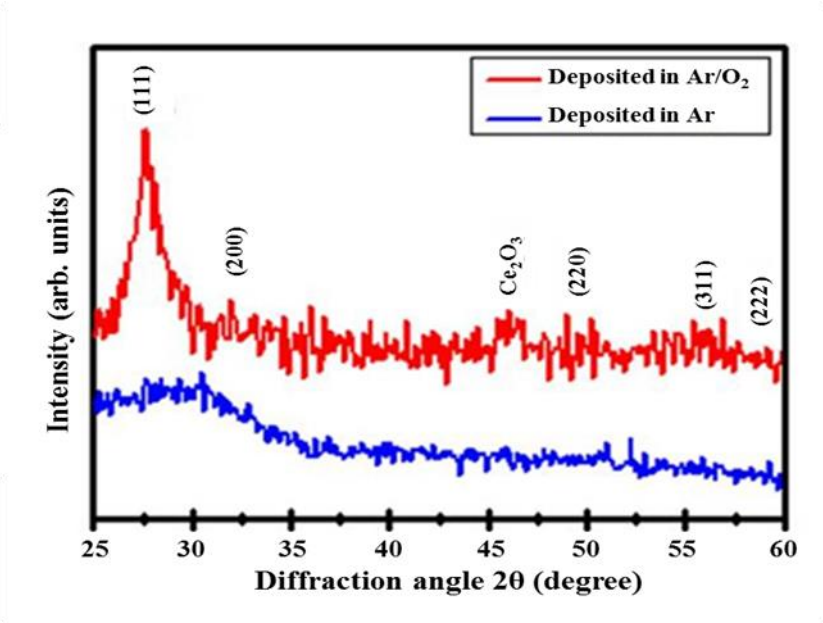

Figure 3.1: XRD pattern of CeO_2 thin films deposited on Si (100) substrates by PDCMS under two different gas conditions, Ar (blue) and Ar/O_2 (red).

The surface morphologies of the CeO_2 sputtered films are shown in Figure 3.2. The root mean square (RMS) value (R_q) of the deposited CeO_2 films are measured from the AFM topography images and R_q values of 0.06 nm and 0.19 nm have been observed for the Ar and Ar/O_2 sputtered samples, respectively. Films sputtered in pure Ar show a smooth surface morphology, whereas the films sputtered in an Ar/O_2 mixture show evidence of a rougher surface, albeit with some isolated larger grains. These isolated grains of different sizes are observed throughout the Ar/O_2 samples possibly due to the formation of polycrystalline CeO_2 as a result of

introducing oxygen in the plasma. Suchea et al. [118] reported that the introduction of oxygen in the plasma is generally believed to support the formation of grains in metal-oxide films due to the impact or presence of high-energy neutral oxygen atoms [118]. Furthermore, oxygen in the plasma could enhance the formation of stoichiometric CeO_2 films [119]. These results can be correlated to the XRD pattern shown in Figure 3.1, where the polycrystalline XRD patterns observed in Figure 3.1 can be correlated to the isolated grains detected in the AFM topography image and similarly for the amorphous film deposited in pure Ar ambient.

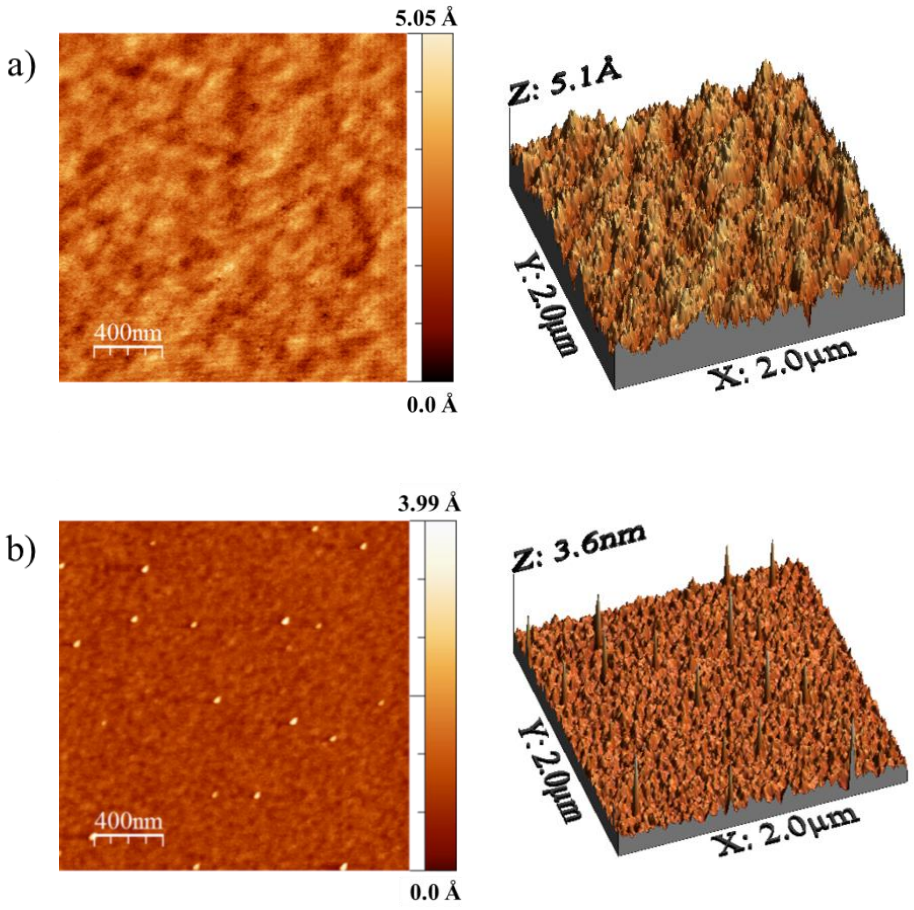

Figure 3.2: 2 ×2 µm² top and 3D view AFM images of CeO_2 thin films sputtered in a) pure Ar and b) an Ar/O_2 gas mixture.

3.3.2 FILM COMPOSITION – SIMS

To provide information on the elemental composition of the bulk material deposited by the PDCMS, SIMS measurements were undertaken at different locations throughout the deposited films. Figure 3.3 shows the SIMS spectra of the sputtered CeO_2 films, grown in Ar and Ar/O_2 ambient, for the mass region from 110 to 200 amu/e. The most intense secondary ion peaks detected are CeO^+ for Ar and CeO_2^+ for Ar/O_2 samples. As more scans are performed and the probing depth increased due to surface sputtering by the Ga ion beam, the secondary ions from both samples displayed similar peaks to that shown in Figure 3.3, with a constant intensity for all CeO_δ peaks throughout the samples. It is important to note that although the intensity of the CeO_2^+ secondary ion peak is the highest for the Ar/O_2 sample, the intensity value of this peak is much lower than the intense peak (CeO^+) detected for the Ar sample. The usual cerium-oxygen molecular ions that can be seen include CeO^+, CeO_2^+, Ce_2O^+, $Ce_2O_2^+$ and $Ce_2O_3^+$ ions. However, the three typical secondary ions most commonly seen in CeO_δ mixed oxide spectra, as reported in the literature, are summarised in Table 3.1 together with their corresponding m/q values [120]. In the case of CeO^+ and $CeOH^+$, there is mass interference and/or overlapping hence multiple peaks are detected between 155.4 amu/e and 157.9 amu/e with a higher $CeOH^+$ intensity observed for the Ar/O_2 sputtered sample.

Table 3.1: m/q values of different observed CeO_δ ion clusters.

Ion	m/q (amu/e)
Ce^+	140
CeO^+	156
CeO_2^+	172

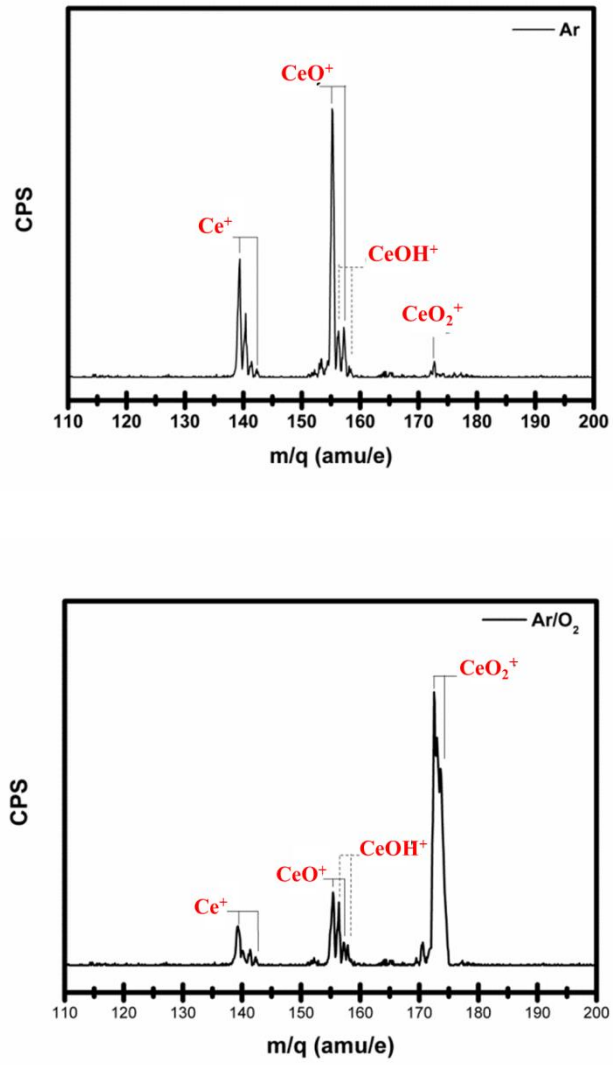

Figure 3.3: SIMS spectra in the range from 100 to 200 amu/e measured from CeO_2 thin films sputtered in a) Ar and b) Ar/O_2.

3.3.3 CHEMICAL ANALYSIS – XPS

The CeO_2 film surface chemical compositions have been studied by XPS to probe the presence of Ce in the Ce^{4+} and Ce^{3+} charge states in the material. CeO_2 films in a chemically reduced state should display XPS peaks corresponding to the Ce^{3+} state [121] while oxidised CeO_2 films should show XPS peaks corresponding to the Ce^{4+} state. XPS scans show the Ce3d peaks

(Figure 3.4) and characteristic O1s peak (Figure 3.5) from which the film stoichiometry and bonding type can be determined. Figure 3.4 displays the core Ce3d levels of the two CeO_2 sputtered films, deposited in Ar and Ar/O_2 atmospheres. The XPS spectrum from the CeO_2 is complex and split into $Ce3d_{3/2}$ and $Ce3d_{5/2}$ peaks, due to spin-orbit coupling effects. The peaks in the region 875-895 eV correspond to the $Ce3d_{5/2}$ while peaks in the region 895-910 eV correspond to the $Ce3d_{3/2}$ levels [108, 122]. The characteristic peak energies associated with different Ce charge states are indicated by the vertical dotted lines. The spectra clearly show the greater concentration of Ce in the Ce^{3+} oxidation state in the sample grown in Ar, indicating a chemically reduced state of CeO_2. This greater concentration of the Ce^{3+} oxidation state in the sample grown in Ar is easily seen by virtue of the peaks at 886.5 ± 0.3, 901.2 ± 0.5 and 904.5 ± 0.3 eV [112]. The Ce^{3+}/Ce^{4+} ratio of CeO_2 samples sputtered in Ar and Ar/O_2 are 4.29 and 1.92, respectively. These values are calculated by comparing the integrated area of the fitted Ce^{3+} and Ce^{4+} peaks.

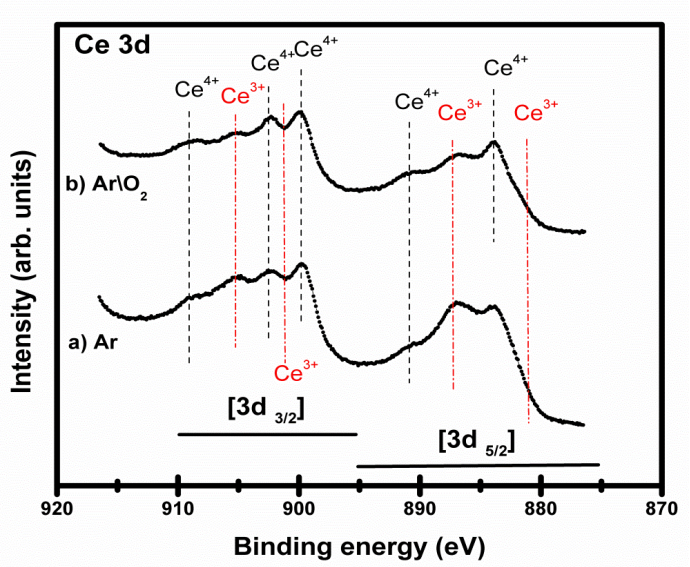

Figure 3.4: Ce 3d core level photoemission spectra from CeO_2 thin films sputtered in a) Ar and b) Ar/O_2 gas atmospheres.

Figure 3.5 shows an O 1s spectrum fitted with two Voigt functions. The main component labelled 'i' has a binding energy of 529.4 eV and is due

to O^{2-} ions [113]. At the high-binding-energy side there is an additional peak labelled 'ii'. Based on the fitting used, the binding energy is 531.1 eV, but the exact value is difficult to determine. Due to the fact that the peaks are rather broad and feature 'ii' is not very pronounced, the formation of $O^{\delta-}$ species and the presence of OH groups or carbon contamination at the surface, have been discussed as possible explanations for this component [108, 113].

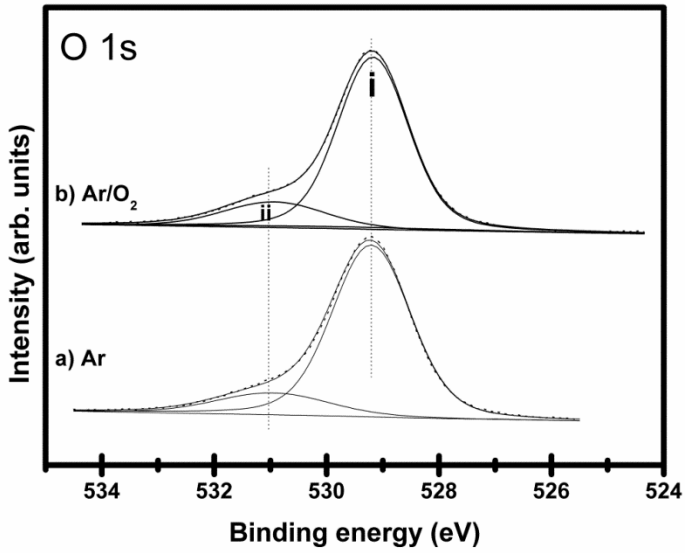

Figure 3.5: O 1s core level photoemission spectra from CeO_2 thin films sputtered in a) Ar and b) Ar/O_2 gas atmospheres. The component labelled '(i)' is attributed to O^{2-} ions. The component labelled '(ii)' is assigned to $O^{\delta-}$ species or OH groups.

3.3.4 ELECTROCHEMISTRY – CV

It is widely known that oxygen vacancies contribute to and enhance the charge storage capacitance of metal-oxides such as MnO_2 [123], ZnO [124], SiO_2 [125] and TiO_2 [126]. It is also known that ceria is a suitable material for charge storage due to the ability of Ce to cycle between Ce^{4+}/Ce^{3+} redox states [127]. Therefore, oxygen vacancies can be correlated directly to the charge storage capacity (CSC) since these may act as a charge carrier [126]. Here, CV of the sputtered CeO_2 films (shown in Figure 3.6) is recorded at various scan rates ranging from 10 to 800 mVs^{-1}. This is done to examine the

redox process present in DC sputtered CeO_2 thin films and to determine the CSC of the films. Figure 3.6 shows CV curves of the sputtered CeO_2 films grown in Ar and Ar/O_2 gas atmospheres in 1 M $LiClO_4$. CeO_2 films sputtered in Ar display two peaks at 0.5 V and 1.2 V where partial oxidation of CeO_2 may occur. These peaks only appear on the CeO_2 films sputtered in Ar, as opposed to CeO_2 films sputtered in Ar/O_2. The negative currents observed during the negative scan suggest a reduction process, which can most likely be attributed to the reduction of oxygen ions [110]. Equation 3.1 is used to determine the double layer capacitance, i.e. the CSC of the films for different scan rates.

$$i = vC_{dl} \tag{3.1}$$

where, i is the charging current, v is the scan rate and C_{dl} is the electrochemical double layer capacitance [128]. Charge storage in CeO_2 results from the ability of cerium to cycle between different redox states and therefore this can be correlated to the OSC of the films [97].

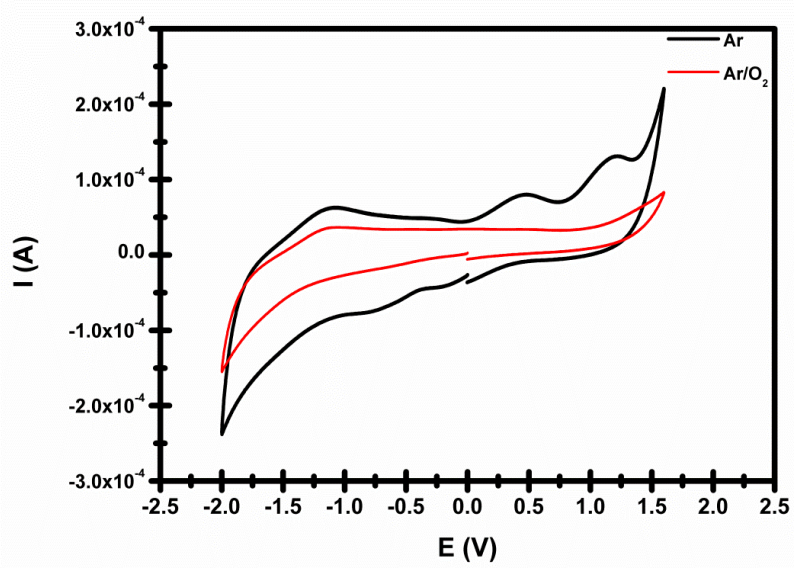

Figure 3.6: CV scan of 50 nm thick nanostructured CeO_2 films deposited by PDCMS technique in a) a pure Ar environment and in b) an Ar/O_2 mixture environment in anhydrous DMF solution with 1 M LiClO4 as supporting electrolyte and a scan rate of 0.1 Vs^{-1}.

The current is measured at -0.1 V for the CeO_2 films sputtered in Ar/O_2 and at -0.2 V for the CeO_2 films sputtered in Ar, in order to avoid inclusion of any Faradaic current or pseudo capacitance effects. Significantly, the peak anodic currents (capacitive current, i_a) for both the films varied linearly with scan rate as shown in Figure 3.7. Double layer capacitance (C_{dl}) values are calculated as $(1.6 \pm 0.2) \times 10^{-4}$ F for the CeO_2 films sputtered in Ar/O_2 and as $(4.3 \pm 0.5) \times 10^{-4}$ F for the CeO_2 films sputtered in Ar. These values show that there is a more than a two fold increase in the CSC when the film is deposited in Ar compared to the sample deposited in the presence of Ar/O_2. The reason for this increase in CSC is thought to be due to absence of oxygen atoms within the deposition chamber, which does aid the oxygen diffusion process through the lattices. It is important to note that the active surface area of both the films is maintained constant at 1.44 cm^2. Thus, these results demonstrate that CeO_2 films grown using a pure Ar sputtering ambient significantly enhances the electrochemical charge storage properties.

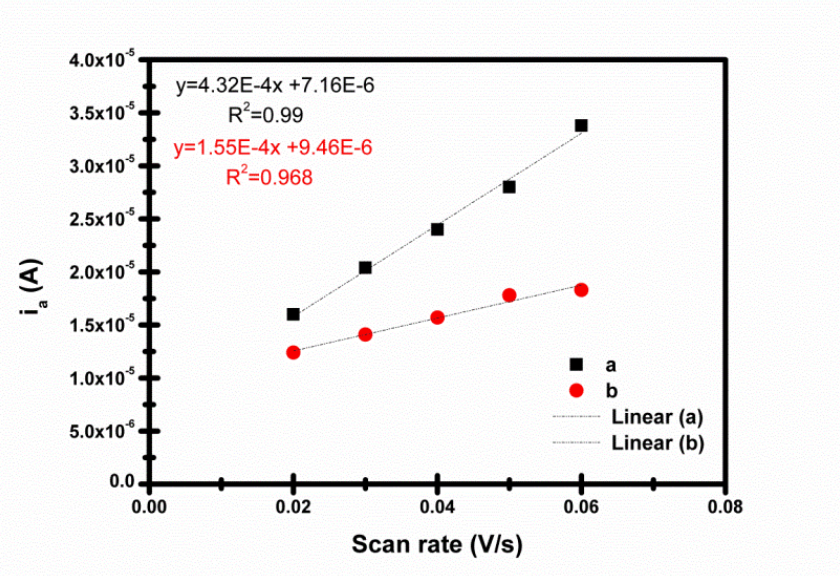

Figure 3.7: Relationship between capacitive current (i_a) and scan rate for CeO_2 films deposited in a) pure Ar and b) Ar/O_2 ambients.

3.3.5 OSC MEASUREMENTS - TGA

Typical OSC measurements require relatively complicated experimental setups. These methods involve gas-phase reactions in pulse mode (flow titration, and gas chromatography or mass spectrometry for detection) [129, 130]. Therefore, a simple OSC measurement technique introduced by Wang et al. [111] is used in this work, where the mass changes of the CeO_2 samples (shown in Figure 3.8) are measured and correlated to OSC using cyclic TGA. Here we used a single TGA cycle to assess the mass change of a supported CeO_2 sample on reduction. After 5 hours of reduction at 600°C, the overall mass change for Ar/O_2 - CeO_2 sample is below the detection limit, i.e. < 0.01 mg which corresponds to experimental uncertainty (due to natural baseline drifts). In contrast, the Ar - CeO_2 sample under similar conditions demonstrated a detectable mass loss of ~ 0.024 mg which corresponds to approximately 0.017% of the total sample mass or to ~ 4.7% of theoretical mass of nanostructured CeO_2 thin film. It is important to note that the equilibrium oxygen nonstoichiometry (δ) in the bulk microcrystalline $CeO_{2-\delta}$ under similar conditions (600°C and $p(O_2) \sim 10^{-21}$ Pa) is reported to be as low as ~ 0.01 [39]. Very small nonstoichiometry variations at this temperature make it impossible to determine the OSC of thin films with higher precision. Nevertheless, the results of thermogravimetric studies clearly show that the samples sputtered in argon atmosphere have a tendency to greater oxygen losses (and therefore higher OSC) upon reduction in a 10 % H_2 flow at 600 °C compared to the films sputtered in Ar/O_2 mixed atmosphere. This implies that samples sputtered in pure Ar atmosphere are reduced CeO_2 deposits containing oxygen vacancies.

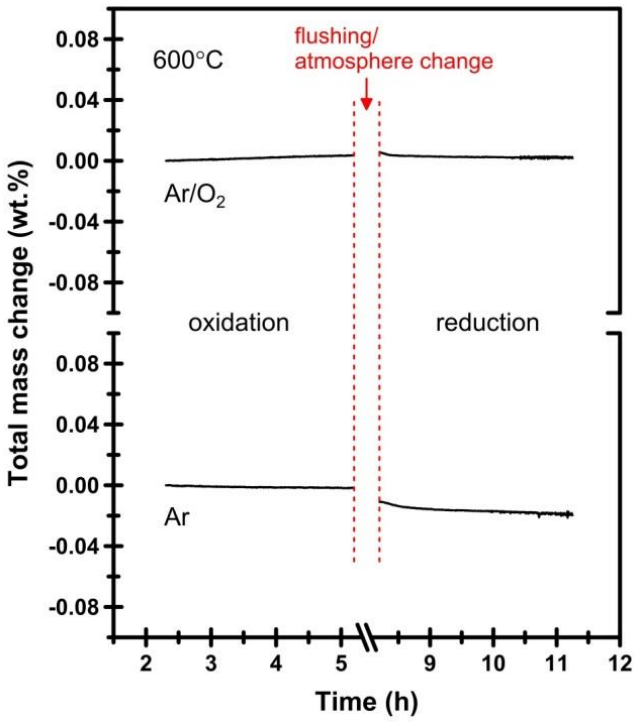

Figure 3.8: TGA curves of CeO_2 films deposited in a pure Ar ambient and in Ar/O_2 mixed ambient, on reduction in 10%H_2-N_2 flow at 600°C.

3.4 CONCLUSIONS

In this study, nanostructured CeO_2 thin films are deposited on Si(100) and ITO coated glass substrates by PDCMS technique using a CeO_2 target. The influence of using various gas ambients on the films, such as a high purity Ar and a gas mixture of high purity Ar and O_2, in the sputtering chamber during deposition are studied. The film compositions are studied using XPS and SIMS. These spectra show a phase transition from cubic CeO_2 to hexagonal Ce_2O_3 due to the ambient atmosphere during the sputtering process. This is related to the transformation of Ce^{4+} to Ce^{3+} and indicates a chemically reduced state of CeO_2 due to the formation of oxygen vacancies. TGA and electrochemical CV studies show that films deposited in an Ar atmosphere have a higher OSC compared to films deposited in the presence of O_2. CV results specifically show a linear variation with scan rate of the

anodic peak currents for both films and the double layer capacitance values for films deposited in Ar/O_2 mixed and Ar atmosphere are $(1.6 \pm 0.2) \times 10^{-4}$ F and $(4.3 \pm 0.5) \times 10^{-4}$ F, respectively. Also, TGA data shows that Ar sputtered samples have a tendency to greater oxygen losses upon reduction compared to the films sputtered in an Ar/O_2 mixed atmosphere. The new key outcome from this work is to demonstrate that the OSC of CeO_2 thin films can be controlled and enhanced by varying the gas atmosphere during deposition.

Chapter 4

FILM ANNEALING TREATMENTS AND CHARACTERISATION

4.1 INTRODUCTION

According to various reports in the literature, highly crystalline CeO_2 can be obtained by applying heat to the substrate during deposition [131, 132]. However, this can also be achieved by post-deposition annealing of the CeO_2 film at high temperatures. Varying the substrate temperature during growth has an effect on the structural, chemical and optical properties but these effects are different to those obtained from varying oxygen flow rates (OFRs) during post-deposition annealing, especially in terms of microstructure (grain size and shape) of the films. Varying the post-deposition annealing temperature or the OFRs also results in changes in the concentration of oxygen vacancies, due to the altered thermodynamic equilibrium [133]. These factors can also influence the structure and morphology of CeO_2 films [134-136], which play an important role in solid/solid catalysis and the electrical properties of CeO_2 [137, 138]. Thus, varying OFRs and temperature

during post-deposition annealing, offers potential for control and engineering of thin film properties.

In this chapter, the effects of post-deposition annealing temperature and atmosphere on the properties of pulsed DC magnetron sputtered CeO_2 thin films deposited in pure Ar ambient, including crystalline structure, grain size and shape and optical properties are investigated. As mentioned in Chapter 3, CeO_2 films deposited in pure Ar atmospheres showed a smooth surface morphology and displayed higher charge and oxygen storage properties than films deposited in the presence of O_2. Therefore, these films were investigated further by post-deposition annealing the films at three different temperatures (500 °C, 800 °C and 1000 °C) and at a fixed temperature of 800 °C under different OFRs. The structural and morphological properties of annealed films were examined using XRD and AFM, respectively. Experimental results obtained from XRD, showed that the prepared films crystallised predominantly in the CeO_2 cubic fluorite structure, although evidence of hexagonal Ce_2O_3 is also seen. The thermal anneal temperature and oxygen content of the Ar/O_2 annealing atmosphere both played important roles in determining the size and shape of the nanocrystals as determined by AFM. The average grain size (determined by AFM) as well as the out of plane coherence length (obtained from XRD) varied with increasing OFR in the annealing chamber. In addition, the shape of the grains seen in the AFM studies transformed from circular to triangular as the OFR was raised from 20 sccm to 30 sccm during an 800 °C thermal anneal. XPS is used to measure near-surface oxidation states of the thin films with varying OFR in the annealing chamber. The bandgap energies are estimated from the UV-Vis absorption spectra and low-temperature photoluminescence (LPL). An extracted bandgap value of 3.04 eV is determined for as-deposited CeO_2 films and this value increased with

increasing annealing temperatures. However, no difference was observed in bandgap energies with varying annealing atmosphere.

4.2 EXPERIMENTAL METHODS

Nanostructured CeO_2 thin films are prepared on Si(100) (for structural, morphological and chemical composition studies) and quartz (for optical studies) substrates (2 x 2 cm) by PDCMS from a 99.99% pure CeO_2 target. Prior to deposition, the substrates are ultrasonically cleaned using acetone, a decontamination solution (30905 Aldrich), de-ionised water and blown dry with a nitrogen stream to remove surface impurities. The same deposition procedures are used to obtain the CeO_2 thin films as that described in Chapter 3, where an ENI RPG-100 pulse generator is used to drive a planar magnetron fitted with the CeO_2 target in power regulation mode. The chamber is first pumped down to a base pressure of 2×10^{-5} Pa by cryogenic pumping. The target is pre-sputtered for 10 minutes prior to deposition to reduce target surface contamination and to obtain a stable plasma density. Sputtering is carried out in a pure Ar atmosphere only (as discussed in Chapter 3) and the working pressure is adjusted and maintained at 0.7 Pa for the duration of the deposition. The target to substrate distance is adjusted to 6 cm. The sputtering is done at room temperature using a power of 65 W at 150 kHz without intentional heating. The substrates are at floating potential and the sputtering time is adjusted to 60 minutes to obtain a uniform film thickness of 50 ± 10 nm for all the deposited samples.

4.2.1 ANNEALING

After deposition and a short contact time with air at room temperature, the CeO_2 thin films samples were transferred into a quartz glass cell, where annealing treatments were performed. Samples were ramped up to target temperatures of 500 °C, 800 °C and 1000 °C at a rate (r) of 40 °C min^{-1} in an air ambient, and held at these temperatures for 1 hour (the dwell time, t_d), in order to study the effect of annealing temperature on the film properties. An optimum temperature of 800 °C (r =40 °C min-1, t_d = 1 hour), which produced good quality polycrystalline CeO_2 films, was chosen and further annealing experiments were carried out to study the effect of varying the O_2 partial pressure ($p(O_2)$) during annealing on the PDCMS CeO_2 deposited films. This is done by heating CeO_2 thin films deposits in an Ar/O_2 atmosphere with different OFRs at 800 °C, while keeping the Ar flow rate (AFR) constant at 50 sccm. The OFR is varied in the range 0 – 50 sccm. After 1 hour of annealing, the sample is allowed to cool down to room temperature (cooling time ≈ 30 min) before characterisation. Note that before each new annealing step, the gas atmosphere is refreshed by pumping and refilling.

4.2.2 CHARACTERISATION

The structural properties of the films are measured using the XRD to determine the crystallinity of the films. The XRD measurements in this chapter are carried out in locked coupled (θ-2θ) mode in a 2θ range of 20° to 60°. A qualitative and quantitative phase analysis of the different phases is done by Rietveld analysis of the diffraction data using the FullProf program [139]. The surface morphology and roughness of the CeO_2 films were studied by a Veeco Nanoscope Dimension 3100 AFM instrument operating in tapping mode using aluminium-coated silicon (Si) probes (Budget Sensors,

Tap300Al-G) with a tip radius of < 10 nm. The intrinsic height resolution of the system is determined by the piezoelectric element and electronic noise and is ~ 0.4 nm, which provides a base level for measurement reliability. The surface roughness of each sample was determined as the root mean square (RMS) value R_q of the distribution of heights in the AFM topography images. The row/column statistical tool of Gwyddion software was used to calculate the standard deviation of R_q of all individual row/column values, and the values obtained were considered when determining the roughness error bars [140]. Where the calculated standard deviation of all individual row/column values is greater than the intrinsic height resolution of the system, the standard deviation is used as the error bar, and where it is less than the intrinsic height resolution, a value of 0.4 nm is used as the error bar. Chemical structure analysis of the CeO_2 films is studied using XPS. The optical absorption properties of the CeO_2 films are studied at room temperature using UV-Vis spectrometer. LPL measurements are carried out from 10 K to 22 K using a closed cycle helium cryostat system and a 325 nm excitation (He-Cd laser) described in Chapter 2.

4.3 RESULTS AND DISCUSSION

As discussed in Chapter 3, the selection of suitable sputtering parameters for the development of good quality CeO_2 films is important and can only be obtained after several repetitions of the experiments, with varying sputtering parameters. However, and as concluded in Chapter 3, CeO_2 deposited in a pure Ar ambient displayed higher OSC compared to films deposited in the presence of O_2. Also and according to various literature reports, varying the post-deposition annealing temperature or the oxygen partial pressure results in change in the concentration of oxygen vacancies, due to the altered thermodynamic equilibrium [133]. These factors can also influence the

structure and morphology of CeO_2 films [134-136]. Therefore, high OSC films deposited in pure Ar atmosphere are further treated to carefully examine the influence/effect of varying the post-deposition annealing temperatures and atmosphere on the film characteristics (microstructure and morphology, composition and stoichiometry, and optical properties). Detailed accounts of the results obtained are provided in this chapter. New and useful information in terms of controlling thin film properties, especially grain shape and size, by varying the annealing temperature and gas atmosphere is provided by the results in this chapter.

4.3.1 STRUCTURE AND MORPHOLOGY

Figure 4.1(a) shows the XRD θ-2θ pattern of the CeO_2 sputtering target used in this study, which shows prominent diffraction peaks indexed to the cubic fluorite structure (PDF No. 00-034-0394). Figure 4.1(b) shows a series of XRD patterns from the CeO_2 thin films: as-deposited and post-deposition annealed at temperatures of 500 °C, 800 °C and 1000 °C for 1 hour in an air ambient. As seen in Figure 4.1(b) and described previously in chapter 3, the as-deposited CeO_2 films show a broad and featureless XRD pattern, characteristic of an amorphous structure. The CeO_2 films annealed at 500 °C shows the emergence of prominent diffraction peaks indexed to the cubic fluorite structure, revealing that the CeO_2 films are being crystallized by the annealing process. For the films annealed at 800 °C and 1000 °C, we observe a higher intensity for the CeO_2 diffraction peaks which clearly reveals that the crystallinity fraction of the CeO_2 films is improved upon increasing the annealing temperature. At these temperatures several weak diffraction peaks corresponding to the Ce_2O_3 phase (PFD No. 00-049-1458) are also observed [141], possibly associated with the oxygen deficient growth environment (Ar gas only). These phases are further investigated using Rietveld refinement

analysis of the CeO_2 diffraction patterns annealed at 500 °C and 800 °C and 1000 °C (shown in Figure 4.1(b)) and this analysis provided some temperature dependent phase change information, but the main conclusion is that the deposit is mainly composed of cubic CeO_2, with some contribution from Ce_2O_3 in all samples, very possibly with a degree of localisation at the surface when the XPS data, described in Section 4.3.2, is considered in conjunction with the XRD data and Rietveld analysis [142, 143]. The details of these impurity phases and their variation with annealing appears rather complex and because of the evidence of surface localisation further work will be needed to elucidate it more fully. Figure 4.2 shows the analysis for the CeO_2 for the three temperatures (500 °C, 800 °C and 1000 °C). To refine the different phases, the structure model (space groups) Fm3m was used for CeO_2, CeO and Ce_2O_3, and; $P\bar{3}ml$ for Ce_2O_3 (although no evidence of the CeO and Ce_2O_3 phases were ultimately seen in the results of the XRD θ-2θ patterns (Figure 4.1)). Analysing the diffraction data it became obvious that some Ce_2O_3 impurity phase occurs in the 800 °C and 1000 °C samples, where there is evidence of the Ce_2O_3 cubic type structure. However, this phase is present only in smaller concentrations (wt.%) of 7.5, 6.6 and 8.1 for 500 °C, 800 °C and 1000 °C, respectively. It can also be seen that the crystallinity deduced from the CeO_2 diffraction data improves with increasing temperature, by comparison of pattern (a) to (b) and (c) in Figure 4.2. As stated above there is no existence of any CeO impurities in any of the samples as determined by the Rietveld analysis. The ratio of R_{wp}/R_{exp}, referred to as the goodness of fit (χ^2-factor) is reported in Table 4.1. For all annealed samples, the χ^2-factor is less than 1.5 indicating a high quality refinement [144]. However, in the XRD refinement of the samples annealed at 500 °C, not all peaks are well fitted/defined and this can be explained to be due to the fact that these samples contain both amorphous and crystalline fractions. Furthermore, the out of plane coherence length of the samples are

reported in Table 4.1, obtained using both the Rietveld refinement analysis and compared to data obtained from the Debye-Scherrer formula using the full width at half maximum (FWHM) of the CeO_2 (111) XRD peak. The values acquired from the refinement are quite similar to those calculated using the Debye-Scherrer equation and therefore we have confidence in employing the Debye-Scherrer equation using the FWHM of the diffraction peak (111) to calculate the out of plane coherence length in all XRD figures including Figure 4.3.

Table 4.1 Rietveld refinement 'goodness of fit' values and out of plane coherence length for the CeO_2 films annealed at 500 °C, 800 °C and 1000 °C.

Annealing Temperature (°C)	Out of plane coherence length (nm)		Goodness of fit values (χ^2)
	Rietveld Refinement Analysis	Debye-Scherrer Formula CeO_2 (111) Peak Data	
500	7.7	7.6	1.13
800	11.0	10.1	1.15
1000	18.5	20.5	1.23

A series of XRD patterns showing the effect of OFR variation during post-deposition annealing (800 ^oC anneal for 1 hour) on the crystallinity of the CeO_2 are shown in Figure 4.3. The OFR ranges from 0 sccm to 50 sccm with a constant AFR of 50 sccm. The diffraction patterns for all samples are crystalline and clearly exhibit the presence of CeO_2 (111), (200), (220), (311) and (222) reflections. There are also weak diffraction peaks corresponding to the Ce_2O_3 phase.

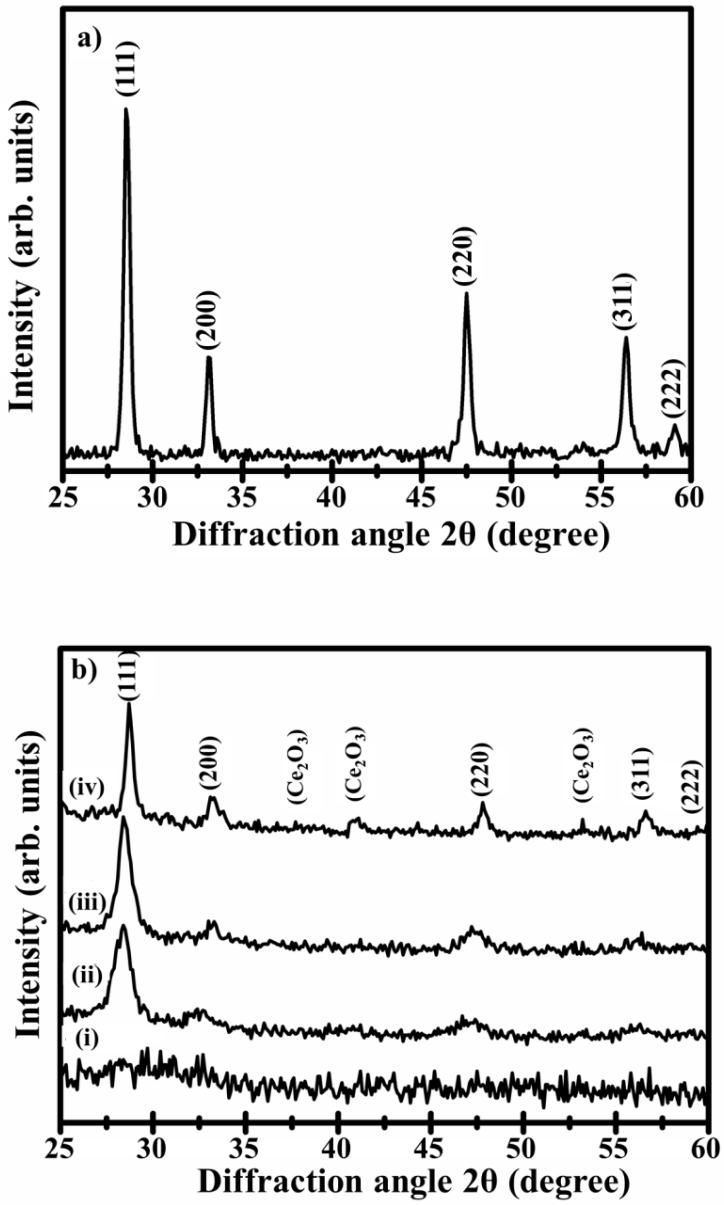

Figure 4.1: XRD θ-2θ patterns of (a) the CeO_2 sputtering target and (b) the CeO_2 films (i) as-deposited and post-deposition annealed at temperatures of (ii) 500 °C, (iii) 800 °C and (iv) 1000 °C in an air ambient.

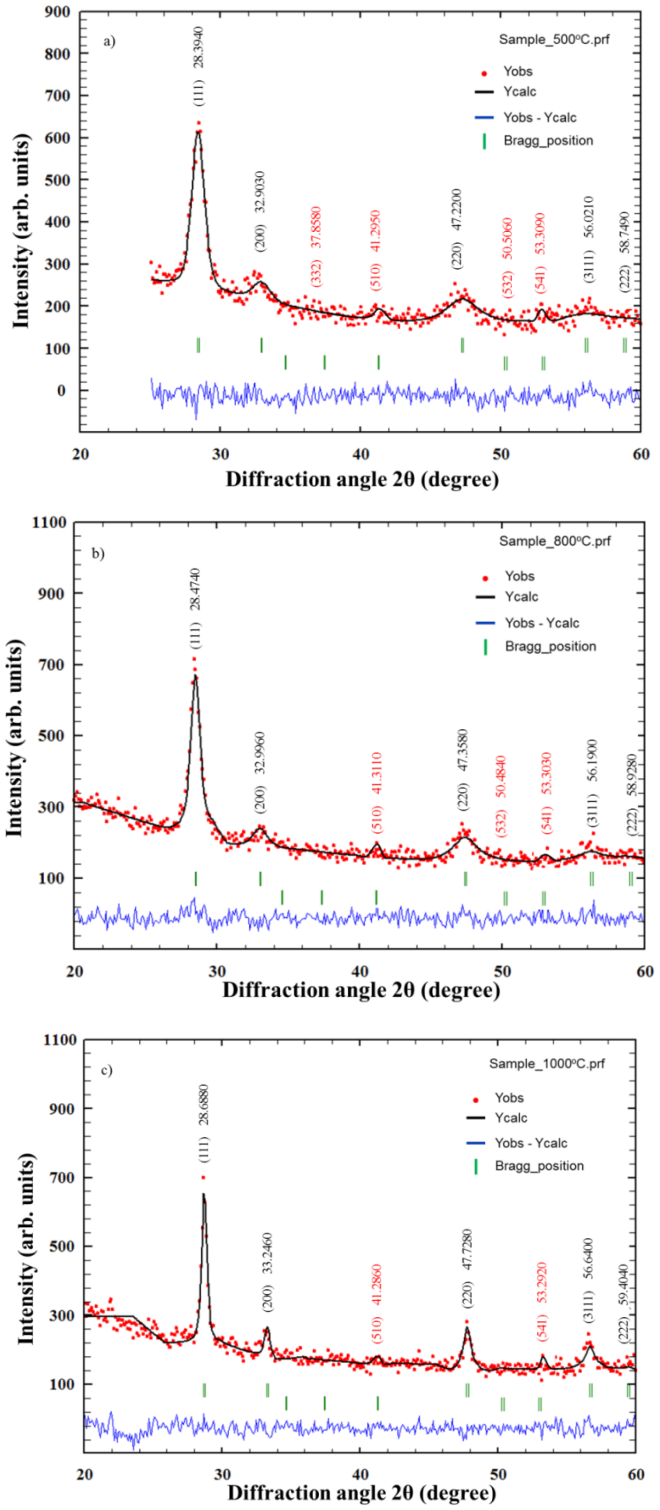

Figure 4.2: Rietveld analysis of three diffraction patterns of CeO_2 annealed samples. a) 500 °C anneal, b) 800 °C anneal and c) 1000 °C anneal. The refinement of data is obtained using three different phases (CeO_2, Ce_2O_3; order corresponds to indicated Bragg peak positions from first to second line and we note that no evidence of the CeO phase is seen).

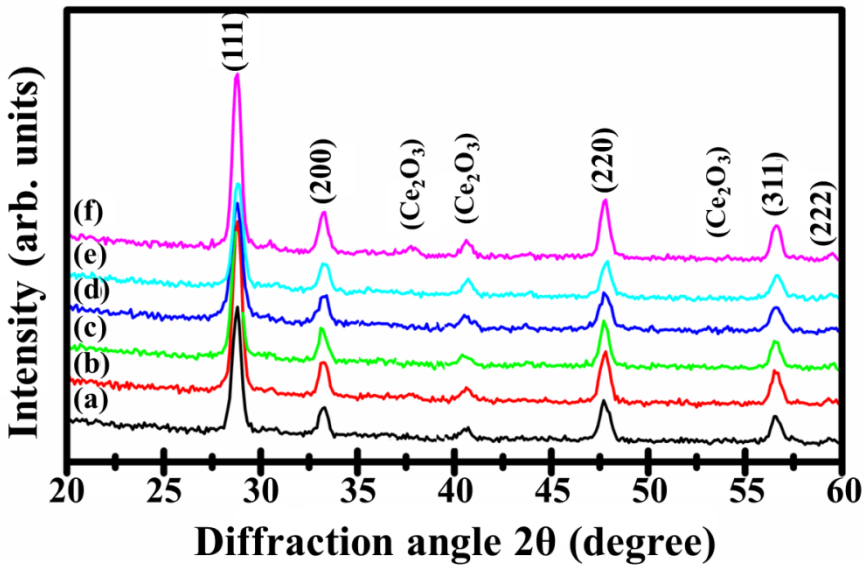

Figure 4.3: XRD patterns of nanostructured CeO_2 thin films grown on Si(100) substrates. The films are annealed at 800 °C, with various OFRs (a) 0 sccm, (b) 1 sccm, (c) 20 sccm, (d) 30 sccm, (e) 40 sccm and (f) 50 sccm. The AFR is kept constant at 50 sccm for all samples.

The FWHM of the (111) XRD peak is used as a measure of the crystalline quality of the CeO_2 crystallites. The out of plane coherence length is calculated using the Debye-Scherer formula [145]:

$$\tau = \frac{0.94\lambda}{\beta \cos\theta} \tag{4.1}$$

As plotted in Figure 4.4, the out of plane coherence length, based on calculations using the (111) peak data, decreases from 24.3 nm to 16.4 nm as the OFR increased from 0 sccm to 30 sccm, and increased to 23.5 nm as the OFR is raised further to 50 sccm. These values are all less than the film thicknesses (which are constant in the range 50 ± 10 nm as mentioned previously) and reveal a nanocrystalline deposit morphology. The oxygen content in the annealing chamber appears to have a small influence on the out of plane coherence length, which can also be correlated to the AFM

images shown in Figure 4.5, assuming the crystallites are approximately equiaxed, but the variation is close to limit of resolution of our XRD system.

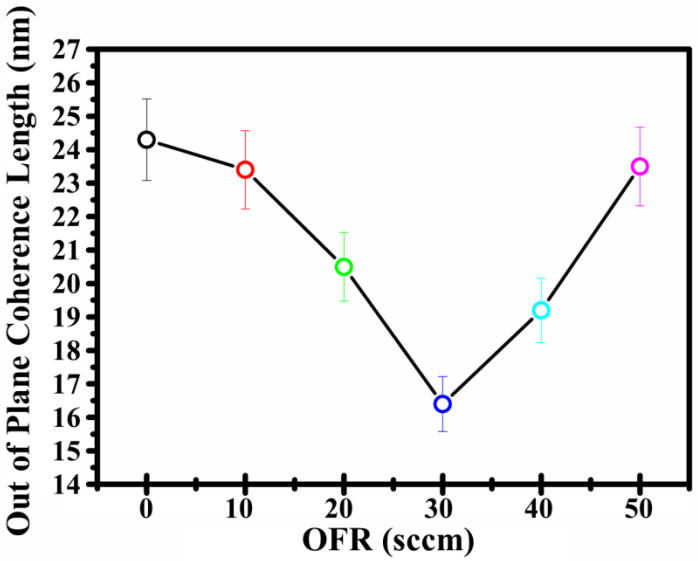

Figure 4.4: Influence of OFR during post-deposition annealing on the out of plane coherence length of the CeO_2 films.

The surface morphologies of the samples are investigated using an AFM. The top-view AFM images for the surfaces of the CeO_2 films are presented in Figure 4.5 for films annealed at 800 °C in various OFRs (0 sccm, 20 sccm, 30 sccm and 50 sccm). The XRD pattern and AFM image of the as-deposited CeO_2 films deposited in pure Ar is shown in Figure 3.1 and 3.2 of Chapter 3. As stated previously, as-deposited CeO_2 films have a very smooth and uniform surface. However, the surface morphology roughens after annealing at 800 °C, due to the crystallisation of the amorphous CeO_2 films. For samples annealed in OFRs of 0 sccm and 20 sccm (Figure 4.5 a and b), the shape of the CeO_2 grains is roughly circular and the RMS roughness values are 3.2 ± 1.2 nm to 2.5 ± 0.4 nm, respectively. By contrast, the grain shape for the samples annealed in OFRs of 30 sccm - 50 sccm (Figure 4.5 c and d) is triangular in nature and the RMS roughness increased from 1.0 ± 0.4 nm to 5.2 ± 2.0 nm. The RMS roughness values (nm) of the films for a 2×2 μm^2 scan

area are summarized in Table 4.2. For comparison, the as-deposited CeO_2 film RMS roughness is very smooth (at or below the intrinsic height resolution of the system, 0.4 nm).

Table 4.2: Summary of post-deposition annealing AFM and XRD results with variation in OFR. Samples are annealed at 800 ^oC for 1 hour.

Sample	OFR (sccm)	(111) XRD Peak FWHM (^{o})	Out of Plane Coherence Length (nm)	RMS Roughness (nm)	Grain Shape
(a)	0	0.35	24.3	3.2 ± 1.2	Circular
(b)	10	0.37	23.4	2.8 ± 0.4	Circular
(c)	20	0.42	20.5	2.5 ± 0.8	Circular
(d)	30	0.52	16.4	1.0 ± 0.4	Triangular
(e)	40	0.45	19.2	2.3 ± 0.6	Triangular
(f)	50	0.36	23.5	5.2 ± 2.0	Triangular

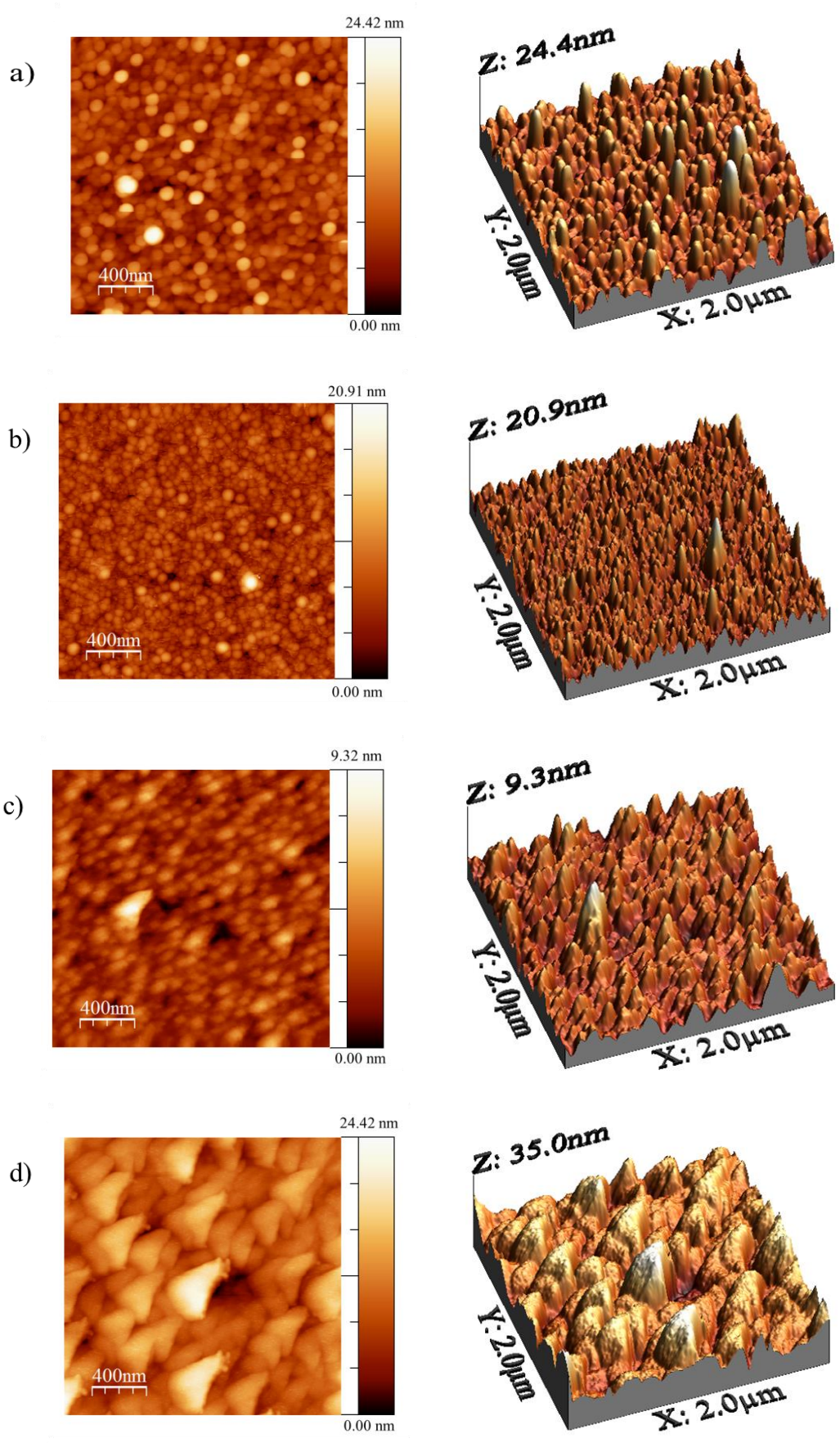

Figure 4.5: 2 x 2 µm² plan-view AFM images of nanostructured CeO_2 films post-deposition annealed at 800 °C in an OFR of (a) 0 sccm, (b) 20 sccm, (c) 30 sccm and (d) 50 sccm. The AFR is kept constant at 50 sccm for all samples.

4.3.2 CHEMICAL COMPOSITION –XPS

The chemical compositions of the films are studied by XPS in order to probe the presence of Ce^{4+} and Ce^{3+} oxidation states and their relative concentrations. Figure 4.6 displays the Ce3d core level spectra of the as-deposited sample (same as Figure 3.4 a in Chapter 3) and samples annealed at 800 °C for 1 hour in different OFRs. There is no significant effect from varying the OFRs in the annealing chamber. The binding energy positions of the Ce^{3+} and Ce^{4+} oxidation state established by previous reported work [112] are indicated by the vertical dotted lines [106]. The spectrum clearly shows a higher concentration of Ce in the Ce^{3+} oxidation state in the as-deposited sample (as shown in Chapter 3) compared to those annealed at 800 °C in Ar gas only, indicating a chemically reduced state of CeO_2 possibly associated with the oxygen deficient growth environment (Ar gas only). Thus the as-deposited CeO_2 sample shows a mixed phase Ce^{3+}/Ce^{4+} charge state, while the annealed CeO_2 samples in 0 sccm and 50 sccm OFRs are solely due to Ce^{4+} (within the limits of sensitivity of our system). It should be noted that although the presence of Ce^{3+} and Ce^{4+} could easily be identified in the Ce 3d as-deposited spectra, the relative concentrations could not be determined due to the complexity of the peak shape and the difficulty in fitting the peak.

Figure 4.7 shows the corresponding O 1s XPS data for the as-deposited CeO_2 and CeO_2 annealed samples. The binding energy positions of the various Ce oxidation states in the O 1s core level spectra are almost identical and overlap considerably [113], mainly due to the O^{2-} nature of the oxygen atom in both Ce_2O_3 and CeO_2. These two contributions give rise to the feature labelled (i) in Figure 4.7 and consequently, it is very difficult to deconvolve the O 1s peak into Ce_2O_3 and CeO_2 components. However, by assuming that the O 1s peak is in a single CeO_2 phase at the surface of the annealed samples due to the absence of a Ce^{3+} oxidation state in the Ce 3d spectra in Figure 4.6, it was possible to establish peak fitting parameters for

the O 1s CeO_2 Ce^{4+}component. These parameters were used to fit the O 1s spectrum for the as-deposited sample, where both Ce^{3+} and Ce^{4+} states exist as shown in the Ce 3d spectra in Figure 4.6. It was evident that an additional peak is needed to achieve an adequate fit and it is suggested that this additional peak is due to the Ce^{3+} oxidation state and is separated from the Ce^{4+} by ~0.3 eV in agreement with Mullins *et. al* [108]. Using these parameters the relative concentrations of the Ce^{3+} : Ce^{4+} as determined by the O 1s core level spectra in the as-deposited film is roughly 1 : 1.

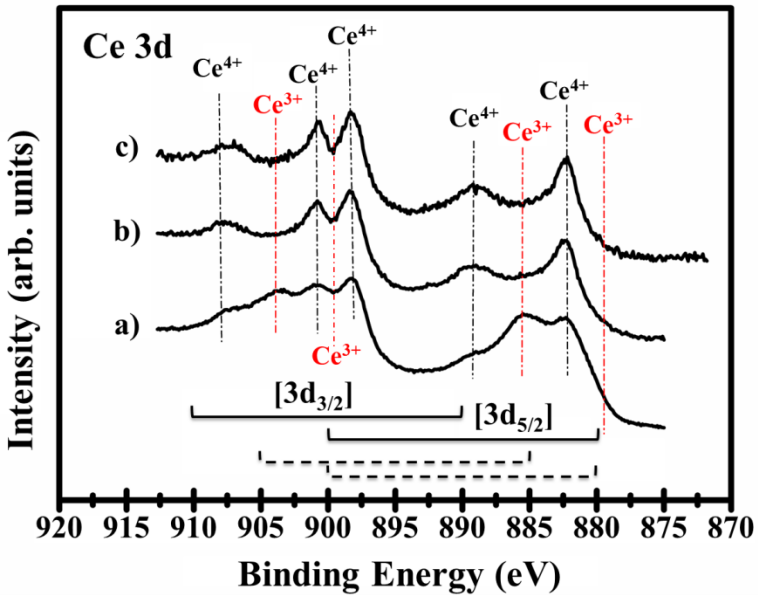

Figure 4.6: XPS Ce3d core level spectra for a) as-deposited CeO_2 and 800 °C annealed CeO_2 samples with OFRs of b) 0 sccm and c) 50 sccm.

The presence of OH groups or C-O contamination on the surface have previously been discussed as possible explanations for the feature labelled (ii) in Figure 4.7, at a binding energy ~ 1.8eV higher than that of the Ce^{4+} oxidation state in the O 1s spectrum [108, 113]. Samples with exposure to different OFRs conditions and samples annealed at a temperature of 800 °C contain larger relative contributions (up to ~31% of the signal in this spectral region) from these contaminant species. As stated above, the annealed

samples, regardless of annealing OFR, show evidence of Ce in the Ce^{4+} oxidation state only and a higher percentage of the contaminant feature (ii).

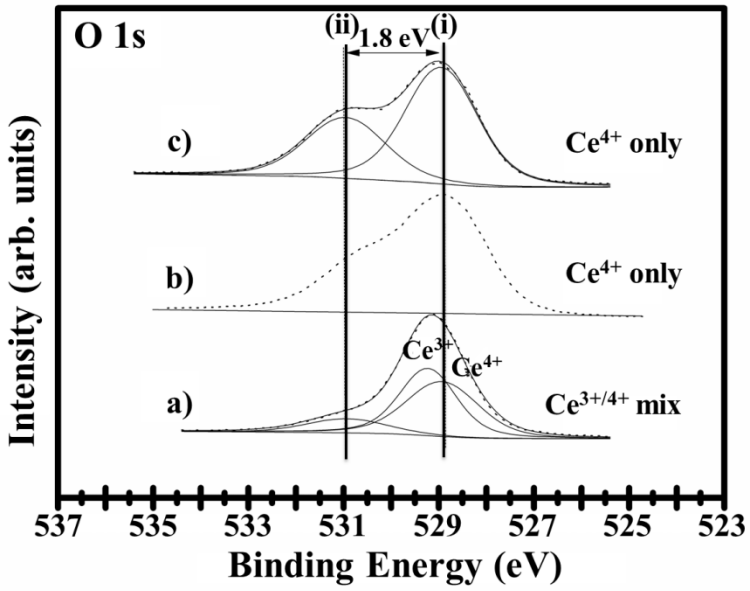

Figure 4.7: O 1s XPS spectra of CeO_2 samples: a) as-deposited, and annealed at 800 °C in b) an OFR of 0 sccm and c) an OFR of 50 sccm.

In Figure 4.8, the annealed CeO_2 samples are further investigated by performing an off-normal emission scan. The scan indicated that the contaminant species O-H/C-O are indeed surface localised, as expected, and are most likely due to atmospheric exposure. All the samples are exposed to atmosphere at room temperature for a short period; thus it is possible that the surfaces of all samples are more heavily oxidised in contrast to the bulk at least within the sampling depth of the XPS, and especially so for the case of some of the annealed samples. Lohwasser *et al.* [146] described an inward diffusion process of O_2 into CeO_2 sputtered films in the temperature range from 700 °C to 950 °C which results in CeO_δ material being surface localised. However due to the proximity of the various oxidation states in the O 1s spectra, it is very difficult to verify these findings using XPS in this study.

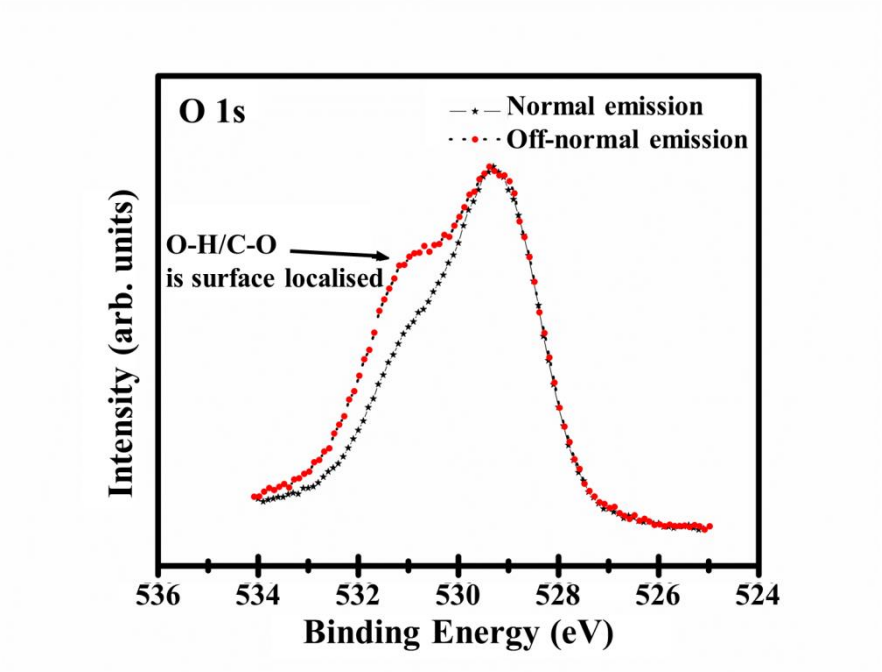

Figure 4.8: O 1s XPS spectra of 800 °C thermal annealed CeO_2 sample (the data shown is from a sample annealed at an OFR value of 50 sccm, but essentially the same spectra and behaviour are seen regardless of OFR value for all samples annealed at 800 °C), normal emission and off-normal emission.

In summary, XPS indicates that the surface of the as-deposited film consisted of a Ce^{3+}/Ce^{4+} mixed phase, while the annealed sample surfaces appeared to contain just the Ce^{4+} oxidation state which is consistent with a more heavily oxidised surface for the annealed samples. It should be noted that XPS is extremely surface sensitive and its findings do not generally accurately reflect bulk properties. Nevertheless, these XPS data are consistent with the XRD data above which show evidence only for Ce_2O_3 and CeO_2 phases, as XPS data from all samples shows the presence of only the Ce^{4+} and Ce^{3+} oxidation states (and no evidence for the Ce^{2+} charge state, associated with the CeO phase, which is not seen in XRD), though the relative concentrations indicated by XRD and XPS cannot be compared for the reason alluded to above.

4.3.3 UV-VIS ABSORPTION AND BANDGAP ENERGY

It was previously reported [147-149] that a change in particle size due to exposure to different temperatures leads to a shift of absorption edge in UV-Vis absorption spectra. Figure 4.9 shows the UV-Vis data from our samples, and the data indicates that the absorption edge shifts toward shorter wavelengths i.e. a blue shift, despite the increase in crystal size, with increasing post-deposition annealing temperature. The direct bandgap energy is estimated by extrapolating the absorption coefficient (α) from the absorbance data using a Tauc plot.

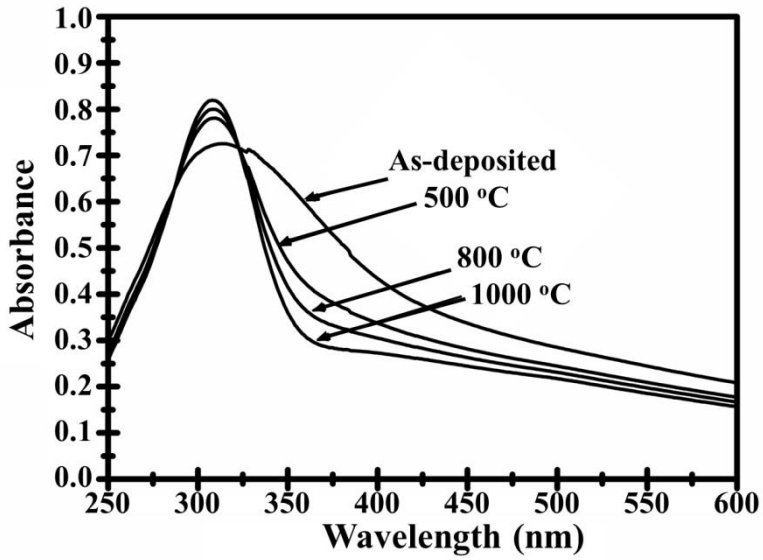

Figure 4.9: UV-Vis absorption spectra of CeO_2 sputtered films, as-deposited and post-deposition annealed at temperatures of 500 °C, 800 °C and 1000 °C in an air ambient.

From the Tauc plot of $(\alpha h\nu)^2$ versus hv (Figure 4.10), one clearly sees that the extracted bandgap value increases from 3.3 eV to 3.6 eV as the annealing temperature increases from 500 °C to 1000 °C. For comparison, the extracted bandgap value is 3.04 eV for as-deposited CeO_2 films. No changes are observed when the OFR is varied in the annealing chamber compared to

the data from a sample annealed at 800 °C in air. The physical meaning of °Cthe extracted values and their variation with process conditions must however be treated with caution, because the influence of excitonic effects, as well as Urbach tail effects, on the spectra is not clear, and it is known that such effects are not accounted for within the Tauc plot formalism [150].

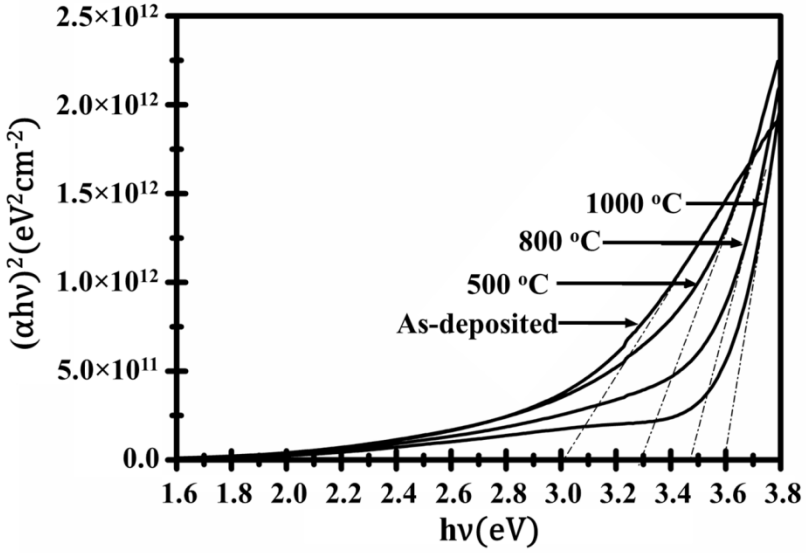

Figure 4.10: Tauc plot of $(\alpha h\nu)^2$ vs. hν for nanostructured CeO_2 sputtered films, as-deposited and post-deposition annealed at temperatures of 500 °C, 800 °C and 1000 °C in an air ambient.

4.3.4 LOW-TEMPERATURE PHOTOLUMINESCENCE

LPL is performed on as-deposited and nanocrystalline CeO_2 films annealed at 800 °C in various OFRs. There were difficulties measuring the LPL spectra of the as-deposited CeO_2 films which showed no presence of any peaks, which may be related to the films' amorphous nature, as highlighted previously. Yet, all nanocrystalline CeO_2 samples displayed similar LPL spectra to that shown in Figure 4.11, so only the data for a sample annealed in an OFR of 50 sccm is shown. It can be clearly seen that the peak intensity at 3.36 eV increases with increasing LPL measurement temperature. This

behaviour indicates that the 3.36 eV emissions are associated with the films (unlike the laser plasma line at ~ 3.43 eV which does not vary with temperature). The emission at 3.36 eV is associated with near bandedge emission from the film material and correlates well with the known value of the CeO_2 bandgap at room temperature (3.2 eV) [43, 151], albeit slightly larger due to the cryogenic measurement temperatures and associated bandgap increase. Furthermore, from our LPL data, it does not appear that the bandgap is significantly affected by the OFR value during the annealing treatment, consistent with the UV-Vis data mentioned earlier.

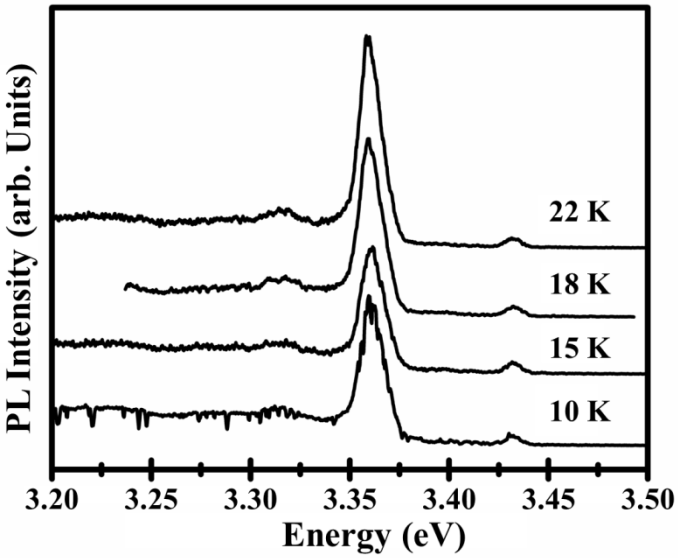

Figure 4.11: LPL spectra of a nanocrystalline CeO_2 thin film annealed at 800 ^oC at an OFR of 50 sccm, measured at 10, 15, 18 and 22 Kelvin (K).

4.4 CONCLUSIONS

From the results presented in this chapter, the crystalline structure and morphology of the amorphous CeO_2 thin films, deposited by PDCMS in pure Ar ambient, described in Chapter 3 are further examined. They are found to be strongly dependent on the post-deposition annealing temperature and

OFR of the Ar/O_2 annealing atmosphere. As highlighted in Chapter 3, the oxygen storage properties are controllable by varying the sputtering deposition parameters; in particular the deposition ambient, where the CeO_2 films grown in Ar ambient displayed higher OSC than films grown in the presence of O_2. Here, the average grain size of the Ar sputtered films can be controlled by either varying the annealing temperature or the OFR during the thermal anneal process. Raising the OFR from 20 to 30 sccm resulted in the grain shape changing from roughly circular to triangular. Analysis of the chemical composition showed that the as-deposited films had contributions from both Ce^{3+} and Ce^{4+} charge states, while the annealed CeO_2 films had contributions predominantly from the Ce^{4+} charge state and this charge state dominated at the film surface. These data are also consistent with XRD data. The thermal anneal temperature also plays an important role in the optical property of the films where an increase in temperature leads to a blue-shift and a decrease in the bandgap value. Our data and analysis clearly show that key material properties such as the bandgap value and the Ce ion charge state can be varied by a suitable thermal annealing treatment. These results are useful in enabling future materials and device development, in terms of being able to control key film parameters for important applications, in particular in the areas of solar-thermal fuel generation and catalysis.

Chapter 5

NANOSPHERE LITHOGRAPHY OF CERIA NANOSTRUCTURES

5.1. INTRODUCTION

It was mentioned previously in Chapter 1, that the rate of H_2 production is directly related to the surface area of the metal oxides; hence, many previous researchers have used porous structures to enhance this parameter. In the context of this thesis, the aim is to increase the surface area through the engineering of spherical nanoshell structures. Not only do the spherical nanoshell structures achieve this but this morphology also increases light absorption, which is essential to enhance the two-step solar driven thermochemical cycling process. This method was proposed by Yao et al. [59] as a light management technique whereby light is trapped inside the spherical nanoshell structures to form whispering-gallery resonant modes, enhancing the light absorption of the metal oxide to enable an efficient solar thermal-driven process. In order to create a CeO_2 nanoshell structure, a cost effective alternative to conventional lithographic techniques such as

photolithography, x-ray lithography etc. is needed. Nanosphere lithography (NSL) is one such alternative and can be successfully employed to create all ordered nanoshell structure.

NSL is an inexpensive, novel fabrication technique that enables nanoscale resolution patterning over large areas [152, 153]. It produces regular and homogenous arrays of nanoparticles with different sizes [154]. This key attribute of NSL is due to its effective self-ordering of polystyrene (PS) latex nanospheres where continuous monolayers can be formed. These nanosphere monolayers can then be treated to reduce their diameter, chemically treated to enhance their hydrophilic character etc., before coating with a film deposit. This results in the formation of nanodimensional features and patterned structures upon the removal of the nanospheres. The formation of an ordered monolayer on a glass plate was first reported, in 1981, by Fischer and Zingsheim [155]. They simply deposited a suspension of colloidal spheres (with a diameter of ~ 300 nm) and allowed it to evaporate. They obtained small-area particle monolayers. This introduced the technique of "naturally" assembled PS latex nanospheres. A year later, Deckman and Dunsmuir extended the scope of the approach of Fischer showing that a monolayer of nanospheres can be used either as a deposit material or as a lithographic mask [156]. Several point defects or dislocations were present in their samples over the scale of tens of micrometers because the mask preparation process is obtained by self-assembly phenomenon rather than by photolithography. They named this strategy "natural lithography". In the 90s, the method was renamed by the Hulteen and Van Duyne group to NSL, and this term is still commonly used nowadays [157, 158]. Over the intervening years, NSL attracted growing interest due to its potential to manufacture a wide variety of one-, two- and three-dimensional nanostructures [159-161].

Following the successful fabrication and characterisation of the CeO_2 films grown using PDCMS in pure Ar environment, as described in details in Chapter 3 and 4, this chapter focuses on increasing surface to volume ratio of these CeO_2 films using NSL. The generation of nanosphere monolayers by self-assembly of PS nanospheres on the surface of DI water and subsequent transfer onto the CeO_2 film coated substrates are demonstrated. Attempts to grow CeO_2 spherical nanoshells using a line of sight technique such as magnetron sputtering are presented. Moreover, two mathematical models, created and used to estimate the increase in surface area as a function of the nanosphere diameter and deposited thickness, are presented.

5.2 GENERATING NANOSPHERES MONOLAYER

The nanosphere colloidal monolayers are generated by a self-assembly on the surface of DI water as shown schematically in Figure 5.1. A low form crystallising glass dish is three-quarter filled with DI water (obtained from a Millipore filtration system). A clean microscope slide is inserted into the water and held still at an angle (~30°) using a retort stand. A nanosphere solution (10% by weight in aqueous solution), containing spheres with a diameter of ca. 600 nm (Fisher Scientific), is diluted with an equal amount of ethanol and mixed thoroughly by sonication. A typical value of 100 µL × 2 (100 µL of nanosphere solution and 100 µL of ethanol) is prepared. Using a micropipette, 20 µL of the mixed solution is slowly applied to the glass slide, immediately above the DI water surface. The tip of the pipette is moved slowly from side to side in order to spread the nanosphere solution across the glass slide until it covers approximately 1 cm of the slide. Care must be taken to ensure the tip of the pipette does not come into contact with the surface of the water as this will lead to spheres being dispersed into the body of the water under the monolayer. This is repeated until enough solution has

been applied to the slide for it to flow down to the water surface. When this occurs, the nanospheres disperse over the water surface. The process is continued until a large area of the water surface is covered, while leaving a clear area large enough for samples to be submerged in the water without coming in contact with the spheres. The substrate is then gently lifted up through the monolayer where the colloidal crystal is transferred to the substrate sample surface. The substrate is allowed to dry at room temperature, leaving the self-assembled monolayer attached to the substrate surface. During this process the application of solution should be continuous; the nanosphere solution should not be allowed to dry on the glass slide as this causes the formation of clumps of nanospheres. The nanosphere solution may also be applied to the side of the glass dish if it has been cleaned thoroughly.

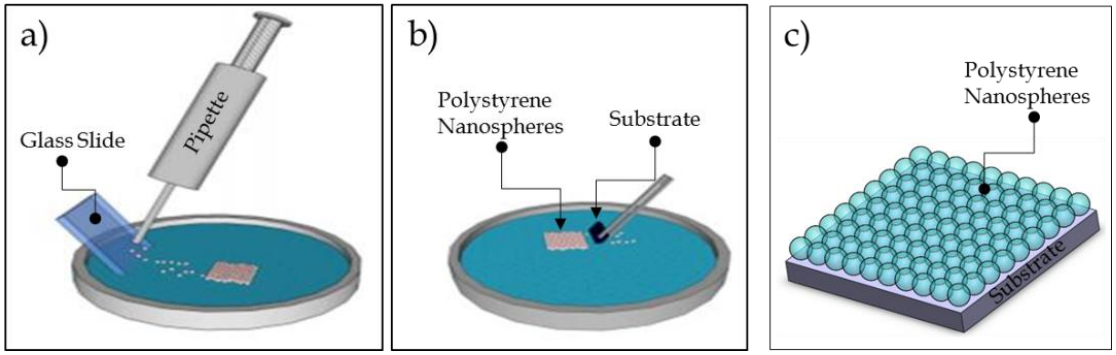

Figure 5.1: A schematic of the equipment and procedures used to obtain nanosphere monolayers on CeO_2 thin films deposited on Si(100), glass and quartz substrates; a) the nanosphere solution is applied to the glass slide just above the DI water surface, b) a self-assembled nanosphere monolayer is created and then lifted off the DI water surface and onto the substrate, c) this results in a nanosphere monolayer deposited on the substrate sample [76].

5.3 NANOSPHERE OXYGEN PLASMA ETCH

The self-assembled colloidal PS nanosphere monolayers deposited on the sample surfaces (described in Section 5.2) are etched using O_2 plasma

(Oxford Instruments Plasmalab 80Plus fitted with an ALCATEL pump) to reduce the nanosphere diameter and thus allow for an interconnection between the CeO_2 (further detailed in Section 5.4) and CeO_2 coated ZnO nanoshell structures (described in Chapter 6). These interconnections between the nanoshells help stabilise and mechanically support the spherical nanoshell structures that are required to enhance the light absorption of the samples. Figure 5.2 shows a graph of the sphere diameter versus O_2 etch time and three SEM images displaying the PS nanosphere monolayers unetched and etched at 60s and 120s exposure times, respectively. These measurements were obtained and analysed by Dr Aidan Cowley and Dr Daragh Byrne, Dublin City University, Ireland. These data are used to control the size of the desired PS nanosphere diameter following etching. The nanosphere monolayers presented in this thesis are all treated in O_2 plasma with an applied power of 300 W, at a pressure of 100 mtorr and an O_2 flow rate of 50 sccm for various periods to reduce the PS nanosphere diameter. The etch time was adjusted to 25 seconds. This etch time reduced the diameter of the PS nanosphere used in this thesis from ca. 600 nm to ca. 520 nm.

5.4 STRUCTURE FORMATION

The cleaned substrate is covered with a monolayer of PS nanospheres. The nanospheres are deposited onto the substrate surface by self-assembly on the surface of the DI water (as described in Section 5.2). In the self-assembly method for depositing a monolayer of nanospheres, a solution containing ethanol and diluted nanospheres in water is applied to the surface of the water. The nanospheres become trapped in the surface of the water due to their hydrophobic character. On the surface of the water, they naturally self -

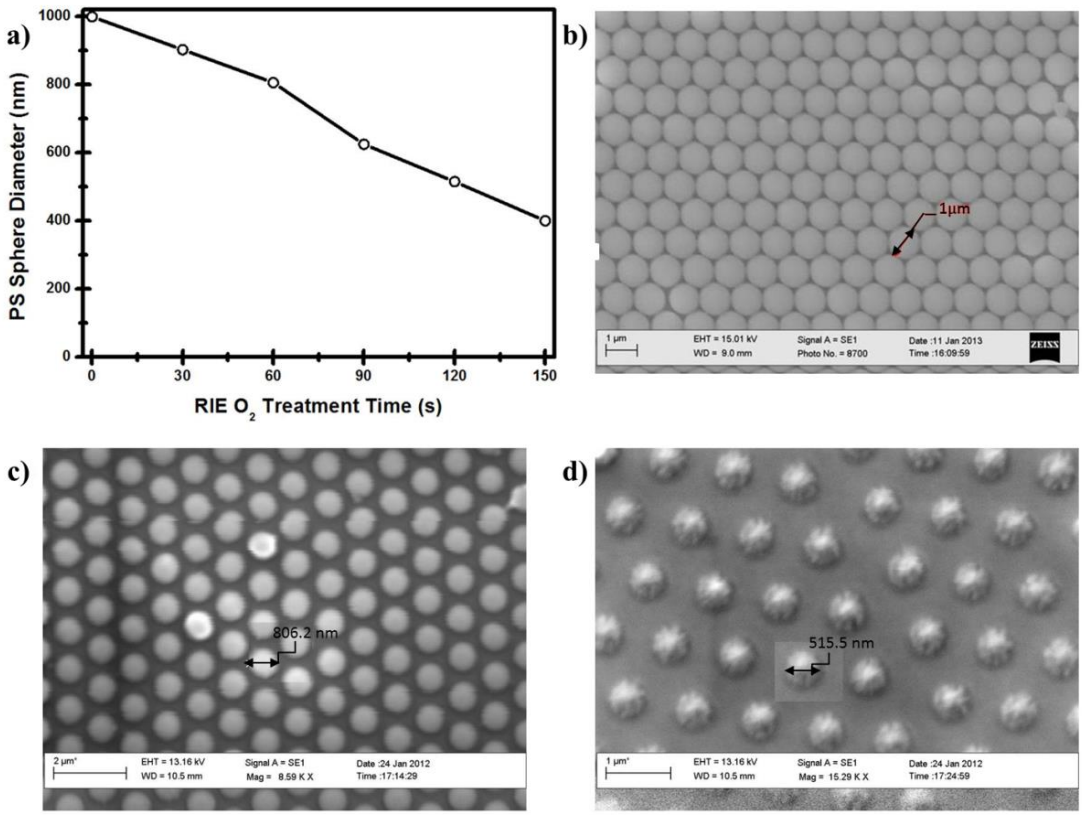

Figure 5.2: a) A graph of PS nanosphere diameters versus O_2 etch time and SEM images of PS nanosphere monolayer samples etched for different times; b) unetched, c) 60s exposure and d) 120s exposure.

assemble into a large colloidal monolayer due to capillary action. This layer can then be transferred onto substrates by gently lifting the substrates through the colloidal monolayer. Using this technique, colloidal crystals have been prepared up to several cm^2 in size, suitable for complete coverage of substrates of a similar area. Substrates coated in this manner are free from bi and tri layers, with fewer domain boundaries and lattice defects. These lattice defects include vacancies and line defects, which are common in all NSL deposition methods reported.

Following the nanosphere deposition on the sample surface, the PS nanosphere monolayer is treated with O_2 plasma in order to slightly reduce the diameter of the nanospheres (as detailed in Section 5.3). This is done not

to only separate the spheres but also to provide enough space between the spheres to enable oxide deposition and mechanically enhance the rigidity of the CeO_2 and ZnO nanoshells (see Chapter 6) to be deposited thereafter. Figure 5.3 shows the SEM images of the PS sphere monolayer template, before and after the O_2 plasma treatment. As shown in Figure 5.3a, a PS sphere monolayer is observed on a Si (100) substrate without aggregation or multiple layer accumulation. Figure 5.3b clearly shows a reduction in the sphere diameters (from 600 nm to ~ 520 nm) after the O_2 plasma treatment, allowing enough space around the spheres for the metal-oxide nanoshell structures to fully interconnect during growth to ensure mechanical stability (further details in Chapter 6). There are some examples of slight movements of spheres, or of a sphere detaching, during the etch despite prior heating at 90 °C for 30 seconds to ensure good adhesion but these are very occasional and do not compromise the overall nanostructure integrity.

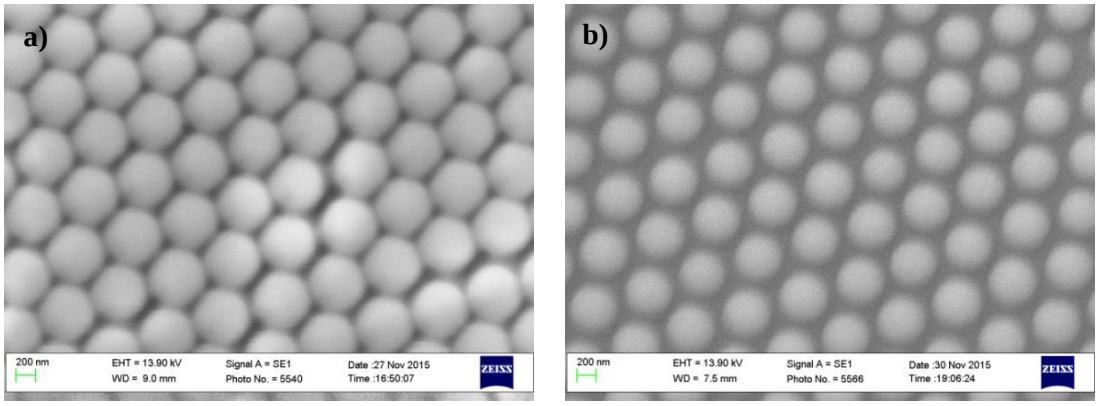

Figure 5.3: SEM images of the PS spheres monolayer deposited on a Si (100) substrate a) before and b) after O_2 plasma treatment. The spheres diameter reduced from ca. 600 nm to 520 nm when exposed to O_2 plasma for 25 seconds.

The samples, with an O_2 plasma treated PS nanospheres monolayer, are transferred into the sputtering chamber in order to coat the PS nanospheres with CeO_2 using the PDCMS system and the sputtering parameters described in Chapter 2 and 3 to generate the CeO_2 nanoshell structures. It is important to note that the sputtering is completed in a pure

Ar atmosphere only. The deposited CeO_2 on the treated PS nanospheres is shown schematically in Figure 5.4. It can be clearly seen in Figure 5.4 and 5.5 that the nanospheres are not completely covered with CeO_2. This can be explained to be due to both the spherical shape of the spheres and the fact that the sputtering process is a line of sight technique. Hence, the sputtered CeO_2 deposit is only able to reach exposed surfaces. Dome-shaped CeO_2 structures are thus realised after PS nanosphere removal, as shown in the plan and 60° view SEM images (Figure 5. 5). To visualise the nanostructures better, the sample was deliberately scratched and further examined using SEM. As can be seen in Figure 5.5 d, the scratched sample clearly shows the dome-shaped CeO_2 nanostructures with clear evidence of the voids.

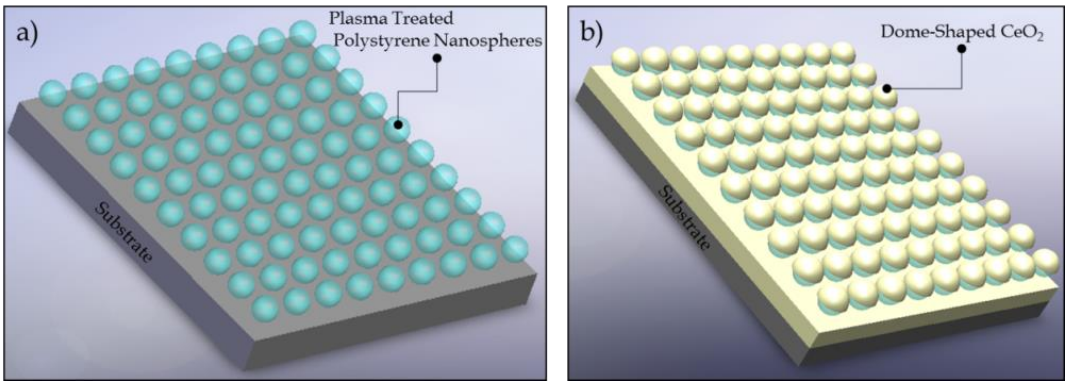

Figure 5.4: 3D images of a) O_2 plasma treated PS nanosphere monolayer deposited on a substrate and b) CeO_2 coated PS nanospheres.

PS nanospheres have a glass transition temperature at 90 °C, a softening temperature at 240 °C, and a full gasification/decomposition temperature at 450 – 500 °C. Therefore, the PS nanosphere monolayer is completely removed by annealing the sample at 500 °C for 30 minutes, which causes the polymer to gasify.

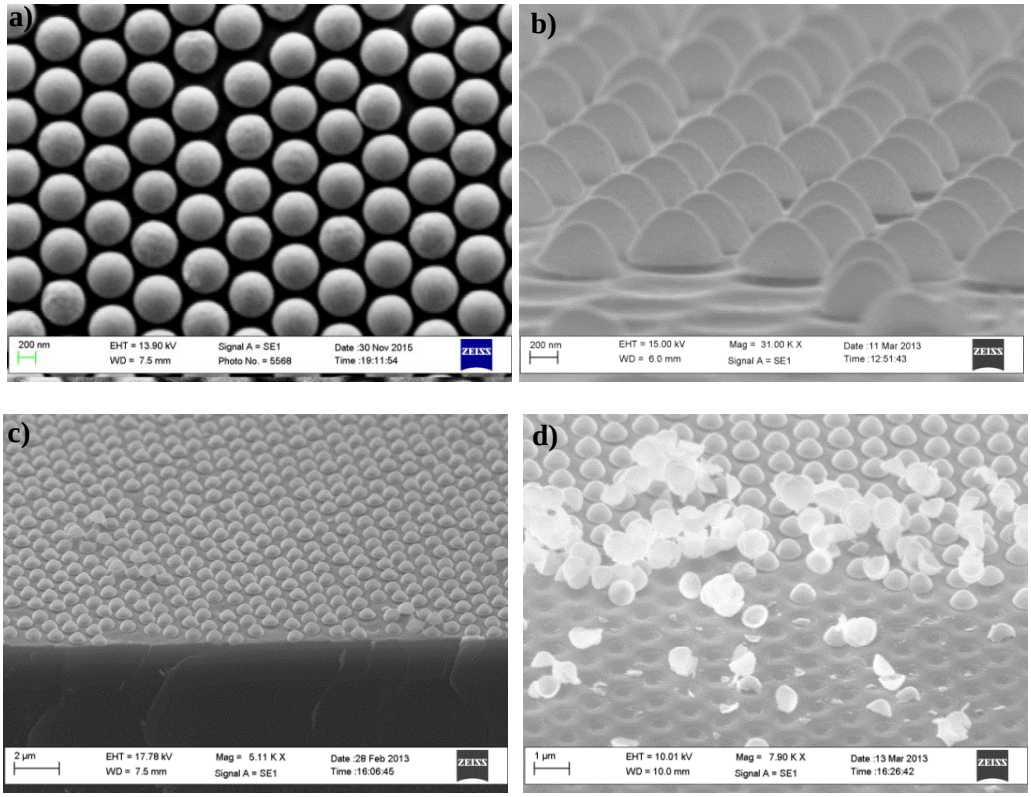

Figure 5.5: SEM images of the dome-shaped CeO_2 nanostructures after the removal of the PS nanospheres (i.e. annealed at 500 °C for 30 minutes in air). The SEM images show a) plan view, b) 45°view, c) and d) 60° view of the dome-shaped structure with a clear evidence of the voids in image d.

5.5 RESULTS AND DISCUSSION

As highlighted previously, the characteristics of the CeO_2 films, used in this chapter, grown by PDCMS in pure Ar ambient have already been examined and discussed in Chapters 3 and 4. Here, we focus on the attempt to create CeO_2 spherical nanoshells using the line of sight magnetron sputtering system. These were explored with the aid of a monolayer of PS nanoshpere template. The unsuccessful attempt resulted in dome-shaped CeO_2 nanostructures rather than spherical shells. These nanostructures were investigated further by examining the structural and morphological properties using XRD and SEM, respectively. The chemical composition was

confirmed using EDX. The optical absorption of the nanostructures was then examined and compared to a flat surface with the same physical thickness.

5.5.1 STRUCTURAL OBSERVATIONS

The structures of the as-deposited and 500 °C annealed CeO_2 films and dome-shaped nanostructures, are examined using XRD, as shown in Figure 5.6. The XRD patterns are recorded at room temperature and the scan is performed through 20 – 60° (2θ), with a step size of 0.1° and an acquisition time of 40s/step. The annealed samples are thermally annealed at 500 °C for 30 minutes in air as stated above, to fully eliminate the PS nanospheres. The XRD scan of the as-deposited CeO_2 film is featureless indicating an amorphous nature (as previously stated in Chapter 3). However, this is not the case in the as-deposited dome-shaped CeO_2 nanostructures. The as-deposited dome-shaped CeO_2 displayed polycrystalline structure with all peaks being identified as those for CeO_2 with a cubic structure (2θ = 28.5°, 33.0°, 47.4°, 56.3°, and 58.9°), with predominant texture along the [111] direction and with no indication of other phases. This could possibly be due to the uneven surface of the PS nanosphere template, which can be linked to literature studies that showed the effect of the substrate surface roughness, and ion bombardment during the sputtering process, on the crystallinity of the deposits[162-164]. Annealing the sample at 500 °C not only removed the PS nanospheres, it also further crystallised the nanostructures and decreased the FWHM value of the XRD reflections from the dome-shaped structures from 1.148° to 0.922°. Furthermore, the annealed CeO_2 film shows prominent diffraction peaks indexed to the cubic fluorite CeO_2 structure, revealing the effect of annealing on the film, although evidence of Ce_2O_3 is also seen. This is addressed in detail in Chapter 4.

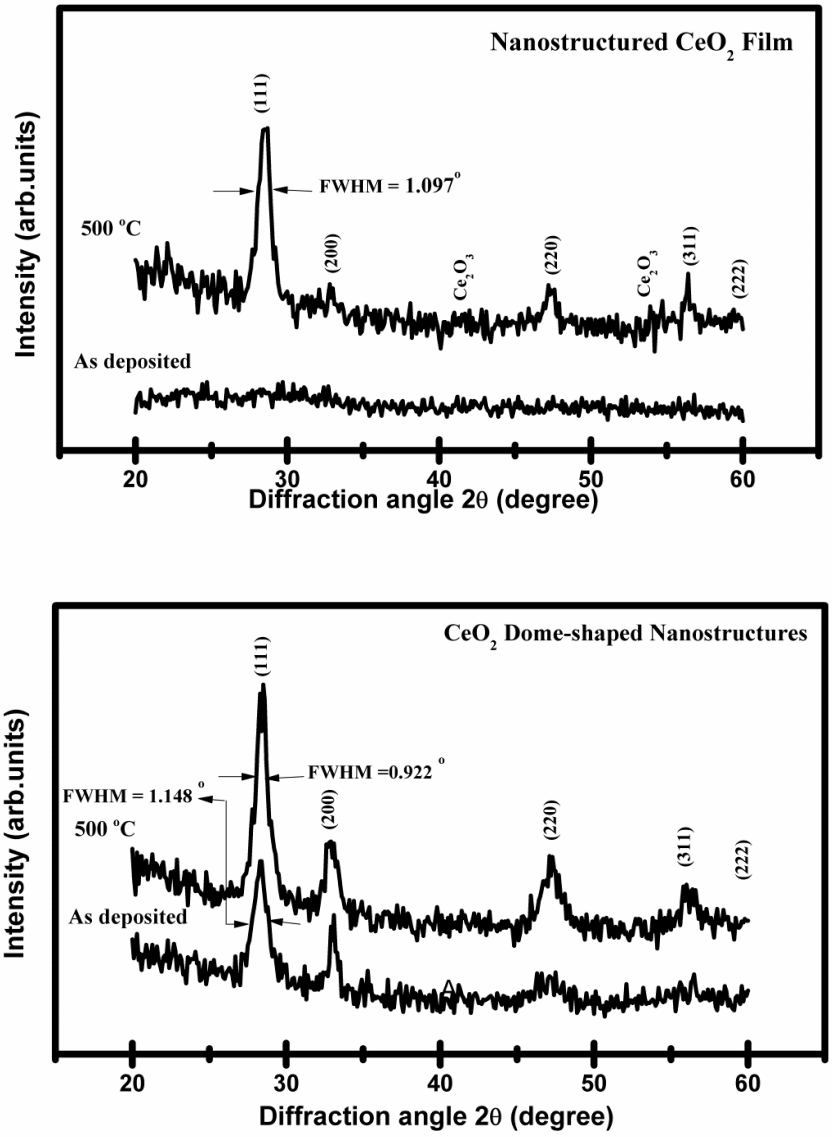

Figure 5.6: XRD θ-2θ pattern (locked coupled) of CeO_2 film (top) and dome-shaped (bottom) nanostructures grown on Si (100) substrates, as-deposited and annealed at 500 °C for 30 minutes. XRD peak located at ~ 28.5° corresponds to the predominant CeO_2 (111) peak.

5.5.2 CHEMICAL COMPOSITION

EDX analysis of the CeO_2 dome-shaped samples was performed to confirm the chemical composition of the nanostructures. It can be clearly seen from the EDX spectrum, in Figure 5.7, that the only constituents detected are Si, Ce

and O for the CeO_2 dome-shaped samples before and after the removal of the PS nanospheres, with a high concentration of Ce being detected on the sample with the PS nanospheres still present. The Si detected is from the substrate and the atomic percentage ratios of the various elements on both samples are shown in Table 5.1. Because there is an underlying SiO_2 layer, the CeO_2 composition/stoichiometry is difficult to calculate with the present data. Using these data the Ce to O ratio can be calculated as ~ 1.6 and 1.2 for the sample with and without the PS nanospheres, respectively. However, it is important to note that these values are not comparable as they depend on many factors including the scanned area, sampling depth and the possible complexity of the chemical reactions during the annealing process.

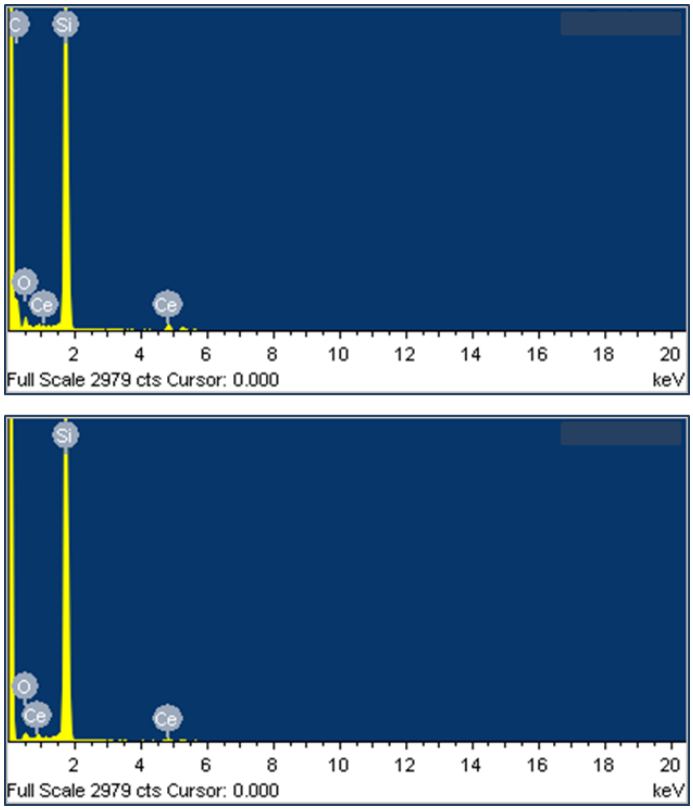

Figure 5.7: EDX spectrum for the CeO_2 dome-shaped before (top) and after (bottom) the removal of the PS nanospheres.

Table 5.1: EDX atomic percentage ratios of the various elements on the CeO_2 dome-shaped nanostructures, before and after the removal of the PS nanospheres.

CeO_2 with PS spheres			**CeO_2 without PS spheres**		
Element	**Weight (%)**	**Atomic (%)**	**Element**	**Weight (%)**	**Atomic (%)**
Si	46.41	30.97	**Si**	87.56	88.59
Ce	8.77	1.17	**Ce**	6.79	1.38
O	5.33	6.24	**O**	5.65	10.03
C	39.49	61.62			

5.5.3 UV-VIS ABSORPTION

The optical properties of the 500 °C annealed CeO_2 film and dome-shaped nanostructure samples were investigated by spectroscopic measurements. The UV-Vis optical absorbance spectra of the samples deposited on quartz substrates are recorded in the wavelength range from 200 to 800 nm. Typical absorbance curve for the CeO_2 film is shown in Figure 5.8. An approximately 50% increase in absorption is exhibited as a result of the dome-shape structure. Note that both films and dome-shaped CeO_2 sample have the same physical thickness of ~ 120 $\pm$ 10 nm achieved by three separate sputtering deposition using same parameters as that described in Chapter 3 and 4. Although spherical nanoshell structures of CeO_2 are not achieved using the PDCMS process, a significant enhancement in the ultra violet (UV) light absorption is achieved. This enhancement can be related to the increase in surface area resulting from the dome-shaped CeO_2 nanostructures and the multiple optical reflections interacting within the domed nanostructure morphology. The increase in area due to dome-shaped nanostructure, using the mathematical model 1 (described in Section 5.6 below), is estimated to be 4 times the surface area of a flat film, which will of course be very beneficial in terms of the surface reactions required in solar-driven thermochemical processes. Figure 5.8 also shows the UV-Vis absorption spectra of the CeO_2

coated PS nanospheres. It can be clearly seen that there is a significant increase in absorption, similar to that seen for the dome-shaped nanostructures, in comparison to the flat film. However, it is essential to remove the PS spheres to optimise light trapping by the different media, considering that the refractive index (n) of PS (1.65) is similar to that of CeO_2 (2.2) and air (n=1).

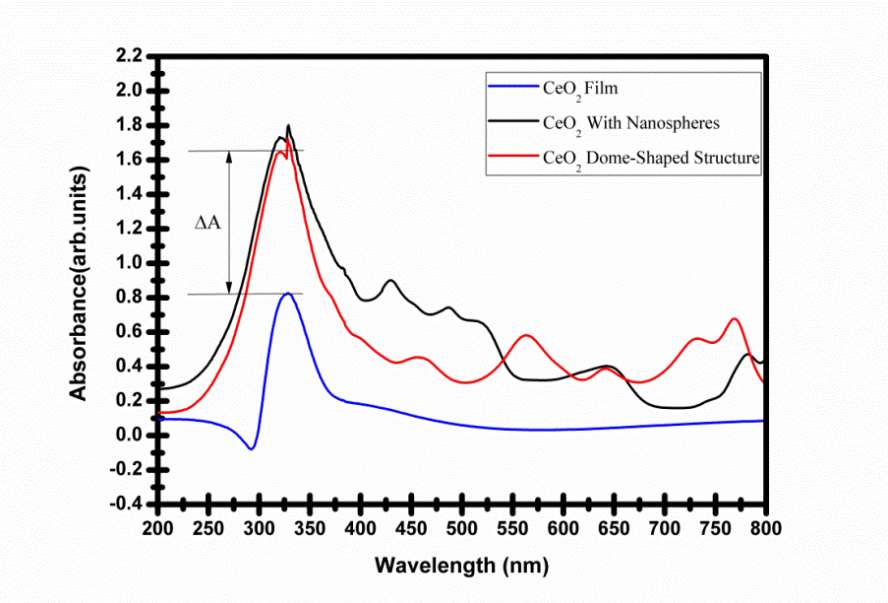

Figure 5.8: Room temperature UV-Vis absorption spectra of CeO_2 film, CeO_2 coated PS nanospheres and CeO_2 dome-shaped structures samples, under normal incidence, with a clear indication of absorption increase (ΔA) as a result of the dome-shaped structure geometry.

The absorbance enhancement is relatively insensitive to the angle of incidence as shown in Figure 5.9. Spectrally integrated relative absorbance enhancement, over the wavelength range 200 – 800 nm, shows a maximum variation of less than 50% between values measured at normal incidence and at an incidence at 70° from the normal for the dome-shaped CeO_2 samples without PS nanospheres, compared to the relevant thin film sample annealed at the same temperature (500 °C) and time (30 minutes). This high value in absorption variation could possibly be due to the geometry and the

unattached nature of the dome-shaped CeO_2 structures, as can be clearly seen in Figure 5.5b.

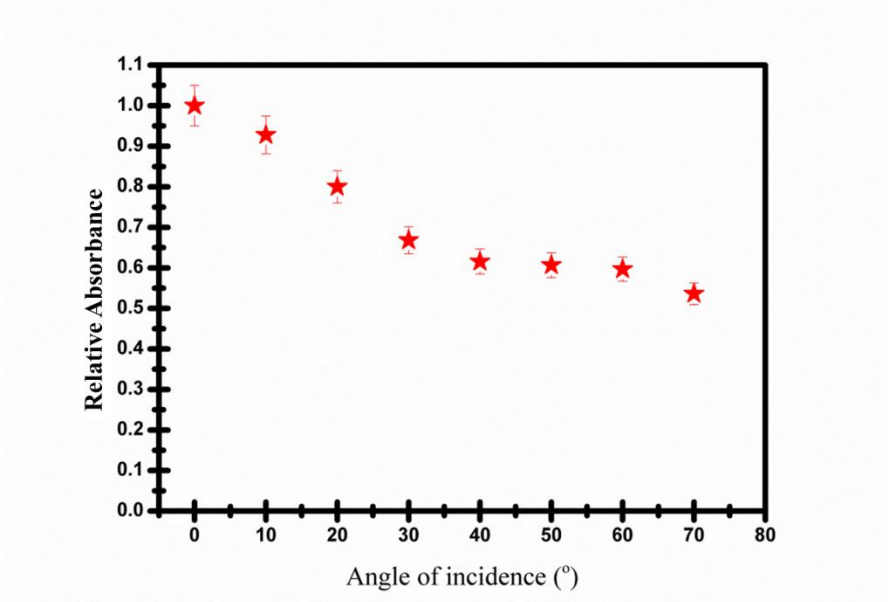

Figure 5.9: Integrated absorption for different incidence angles relative to the normal incidence for the CeO_2 dome-shaped structures sample deposited on quartz substrate.

The relative absorbance enhancement at angle $i°$ is calculated using the following formula:

$$\text{Relative Absorbance Enhancement } (i°) = \frac{I_{A_i°}}{I_{A_0°}} \tag{5.1}$$

$I_{A_i°}$ and $I_{A_0°}$ are the spectrally integrated absorbance enhancements at normal incidence and at an incidence angle of $i°$ from the normal, respectively. The spectrally integrated absorbance enhancement at all incident angles was determined using

$$I_{A_i°} = I_{A_i°}\,(\text{NS}) - I_{A_i°}\,(\text{F}) \tag{5.2}$$

Where $I_{A_i°}$ (NS) and $I_{A_i°}$ (F) are the spectrally integrated absorbance for the nanoshell and thin film samples with the same physical thicknesses of the materials in both the film and nanoshell morphologies, respectively.

5.6 MATHEMATICAL MODELING

Two mathematical models used, in the context of this research in order, to determine the increase in surface area based on the diameter (D) of the PS nanosphere and the film thickness (t) are described in detail in this section. These models define the ratio of the newly increased metal-oxide surface area (A_j), following NSL , to uniform flat surface area (A_i) The first model incorporates an increase in surface area for dome-shaped metal-oxide structures similar to that produced in this chapter and is shown in Figure 5.5. The second model incorporates an increase in surface area for hollow spherical metal-oxide nanoshell structures such as that engineered and described in Chapter 6.

5.6.1 MODEL 1: DOME-SHAPED STRUCTURES

The metal-oxide uniform flat surface area (A_i), prior any surface area increase using NSL, can be simply described as:

$$A_i = LW \tag{5.3}$$

where L and W are the length and width of the substrate, respectively.

After NSL patterning is used to increase the surface are of the metal-oxide deposits using a line of sight method, such as the PDCMS, the increased surface area (A_j) for dome-shaped metal-oxide nanostructures, such as that shown in Figure 5.10, is given by:

$$\begin{aligned} A_j = {} & \text{Area of substrate} - n(\text{area of circle}) \\ & + n\ (\text{surface area of internal and external hemispheres}) \end{aligned} \tag{5.4}$$

where the term n in the above equations is the number of nanospheres on the substrate surface which is approximated using

$$n = \frac{LW}{D^2} \tag{5.5}$$

Therefore, substituting in the appropriate formulas into Equation (5.2), we get

$$A_j = (LW) - n\pi(\frac{D}{2})^2 + 2n\pi[(\frac{D}{2} + t)^2 + (\frac{D}{2})^2] \tag{5.6}$$

This simplifies to

$$A_j = (LW) + n\pi\,(\frac{3}{4}D^2 + 2Dt + 2t^2) \tag{5.7}$$

And

$$A_j = (LW) + \pi LW\,(\frac{3}{4} + \frac{2t}{D} + \frac{2t^2}{D^2}) \tag{5.8}$$

Hence, the surface area ratio ($\frac{A_j}{A_i}$) of the increased surface area relative to the uniform flat surface area is (A_i) is

$$\frac{A_j}{A_i} = \frac{4\,(LW) + n\pi(3D^2 + 8Dt + 8t^2)}{4\,LW} \tag{5.9}$$

This can be simplified to

$$\frac{S_j}{S_i} = 1 + \pi\left(\frac{3}{4} + \frac{2t}{D} + \frac{2t^2}{D^2}\right) \tag{5.10}$$

It is clear that equation (Equation 5.10) does not require the length and width of the substrate/sample to be known in order to obtain the relative increase in surface area, as a result of the dome-shaped structure, relative to the flat surface. It only requires inputs of the nanosphere diameter (D) post O_2 plasma etch treatment and the deposit film thickness (t).

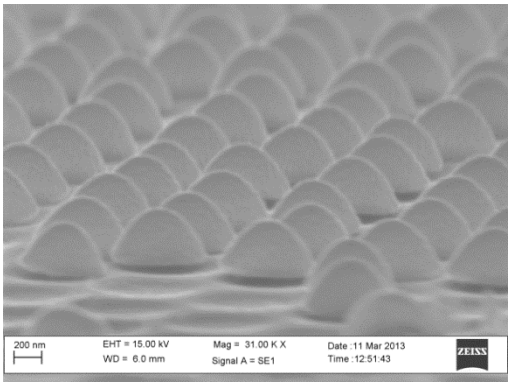

Figure 5.10: SEM image of dome-shaped metal-oxide nanostructures.

Using the above model for nanosphere diameters of 620 nm, 520 nm and 420 nm with the same thickness, the increase in surface area are found to be approximately 3.9, 4 and 4.2 times that of a uniform flat surface area, respectively. Hence, reducing the nanosphere diameter resulted in a slight increase in surface area in comparison to a flat surface.

5.6.2 MODEL 2: SPHERICAL NANOSHELL STRUCTURES

Post NSL and metal-oxide deposition using techniques that provide full coverage of the nanospheres, the surface area (A_j) for the spherical metal-oxide nanoshell structures similar to those shown in Chapter 6 and Figure 5.11 can be described as:

$$\mathrm{A_j} = \text{Area of substrate} - \mathrm{n}(\text{area of circle}) + \mathrm{n}\ (\text{surface area of internal and external spheres}) \quad (5.11)$$

$$A_j = (LW) - n\pi(\frac{D}{2})^2 + 4n\pi[(\frac{D}{2} + t)^2 + (\frac{D}{2})^2] \quad (5.12)$$

This simplifies to

$$A_j = (LW) + n\pi\,(\frac{7}{4}D^2 + 4Dt + 4t^2) \quad (5.13)$$

Therefore, the increase in surface area ratio as a result of the spherical nanoshell structure is

$$\frac{A_j}{A_i} = \frac{4\,LW + n\pi(7D^2 + 16Dt + 16t^2)}{4LW} \tag{5.14}$$

This can be simplified further to Equation 5.15 by substituting in for n using Equation 5.5 above.

$$\frac{S_j}{S_i} = 1 + \pi\left(\frac{7}{4} + \frac{4t}{D} + \frac{4t^2}{D^2}\right) \tag{5.15}$$

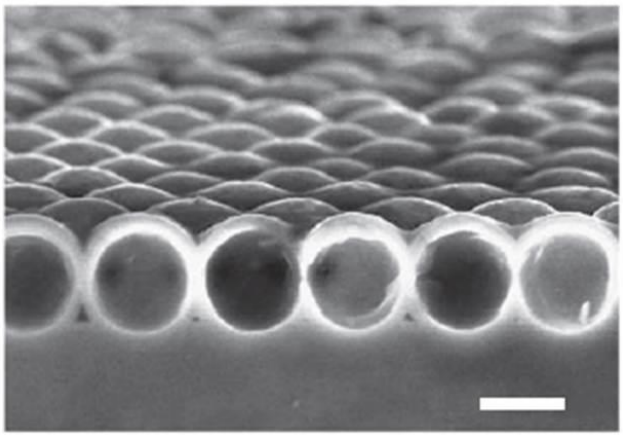

Figure 5.11: SEM image of hollow spherical metal-oxide nanostructures [59].

Therefore, for nanosphere diameters of 620 nm, 520 nm and 420 nm with the same thickness, the increase in surface area using model two are 7.6, 7.8 and 8.2 times that of a uniform flat surface, respectively. Thus, the smaller the diameter of the nanospheres, the higher the surface area obtained. However, this may vary with variations in the deposit thickness i.e. this model is only valid when $t \leq \frac{d}{2}$, where d is the distance separating between two adjacent spheres (see Figure 5.12).

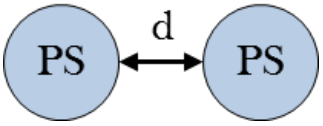

Figure 5.12: Representation of the distance (d) separating two adjacent spheres.

5.7 CONCLUSION

In this chapter, studies of dome-shaped CeO_2 nanostructures obtained by depositing CeO_2 on a monolayer of patterned PS nanospheres template using PDCMS, with same parameters as that reported in previous chapters, are reported. This is achieved as result of both the spherical shape of the spheres and the fact that the sputtering process is a line of sight process that only deposits exposed areas. Although a spherical nanoshell CeO_2 structure is not accomplished in this chapter, the dome-shaped CeO_2 resulted in a 50% increase of UV light absorption, compared to a flat surface with the same physical thickness. It also increased the relative surface area by a factor of approximately four compared tothe flat surface. Furthermore, the structural properties and morphology of the nanostructures are examined by XRD and SEM, respectively. XRD shows that the deposits crystallise when deposited on the PS nanosphere template and after a high temperature treatment. Finally, two mathematical models are established to estimate the relative increase in surface area with and without lithography.

Chapter 6

ENHANCED OPTICAL ABSORPTION VIA SPHERICAL NANOSHELLS

6.1 INTRODUCTION

As stated in Chapter 5, increasing the surface to volume ratio is essential in enhancing the process of a solar driven thermochemical process, as is increasing the light absorption efficiency. Achieving this through the engineering of spherical nanoshell structures using NSL, to enhance both surface to volume ratio and broadband light absorption, remains a challenge. Successful achievement of this important new design will dramatically improve both the light absorption (and reduce adverse directionality effects due to the substantial enhancement of the effective light path in the active material) and the effective surface area for surface reactions [165, 166]. Applying this important recent development in in conjunction with a redox mediator and a UV absorber, such as CeO_2 and ZnO [167, 168], can result in the enhancement of UV light absorption and surface chemical properties, which can in turn be used for more effective applications in a variety of technologies.

Materials based on CeO_2 are extensively used in many applications including the oxygen ion conductor in solid oxide fuel cells [169], UV absorption [168, 170], gas sensors [171] and many more applications previously mentioned. Apart from the well-known oxygen storage capacity of CeO_2 and its redox properties, CeO_2 is also suitable for many personal care products specifically related to its ability for blocking ultraviolet radiation [172-174]. Similarly, ZnO is an important and promising material with many potential applications in short-wavelength optoelectronic devices [175], such as transparent conductive films, surface electro-acoustic wave devices, ultraviolet (UV) emitters, cold cathode emitters, etc. It has a wide and direct bandgap energy of 3.3 eV at room temperature [176] and many typical properties such as transparency in the visible range, electrochemical stability and non-toxicity [177, 178]. Therefore, combining both materials (ZnO and CeO_2) can results in an enhanced/unique UV absorption material as well as high stability at high temperature and high hardness [168].

ZnO nanostructures recently attracted a great attention due to their interesting properties for photonic applications and the variety of morphological structures which can be achieved including nanorods [179], nanorings [180], nanowires [181] and nanobelts [182]. Among these various structures, hollow nanostructures are interesting structures for applications such as photocatalysis [183], solar cells [184], drug delivery [185] and much more [186-188]. Synthesising hollow ZnO nanostructures has been recently done using various templates. For example, Jiang et al. [189] synthesised ZnO hollow spheres using ethanol droplets as soft templates while Duan et al. [190] synthesised ZnO hollow spheres by coating PS beads. Others, like Li et al. [191], Shen et al. [192] and Deng et al. [193], synthesised ZnO hollow particles using a template-free solution method, template-free evaporation method and template-free sonochemical fabrication method, respectively. Although these proposed methods are described as simple and inexpensive,

the drop coating method (proposed by Byrne et al. [179, 194]), using a template of PS beads, yields samples with a patterned spherical nanoshells of ZnO with improved crystallinity, purity and optical properties.

In this chapter, which is a continuation of Chapter 5 ZnO nanostructures, CeO_2 nanostructures and CeO_2-coated ZnO nanostructures were synthesised by simple and efficient low temperature deposition methods on Si (100) and quartz substrates. This approach was considered following the unsuccessful attempts of generating pure CeO_2 nanoshell structures using the line of sight (PDCMS) and the chemical bath deposition methods described in Chapter 5 and 7, respectively. The ZnO films were prepared by a novel drop coating deposition method. This was then combined with a thin layer of the redox active material CeO_2 (similar to that deposited and characterised in Chapter 3 and 4) to form CeO_2-coated ZnO films. Spherical ZnO nanoshell structures and CeO_2-coated ZnO nanoshells have been successfully prepared using PS sphere monolayer templates. The samples used in this study are shown in Figure 6.1. The structural properties and morphologies of the nanostructures are analysed by XRD and SEM. XRD data shows that the prepared films and nanoshells crystallised predominantly in the ZnO wurtzite and CeO_2 cubic fluorite structures when post-annealed at 500 ˚C and 800 ˚C in air. The nanostructure compositions are studied in more detail using SIMS. The optical properties of the nanostructures are measured using UV-Vis absorption spectroscopy and room temperature PL in order to ascertain the effects of the nanoshell structures and the WGMs associated with these structures on the optical properties of the deposits. To the best of our knowledge, using drop coating of PS sphere templates to engineer patterned spherical nanoshells of ZnO has not been reported previously, and is a very simple and versatile method. This work provides useful information on the influence of the nanoshell geometry on the absorption properties of various combinations of these two

types of materials. The addition of the CeO_2 thin film on top of the ZnO hollow nanostructured deposit enhances the UV light absorption further and provides additional functionality such as oxygen storage capacity via changes in stoichiometry. The redox properties of these types of PDCMS grown CeO_2 films are reported in Chapter 3.

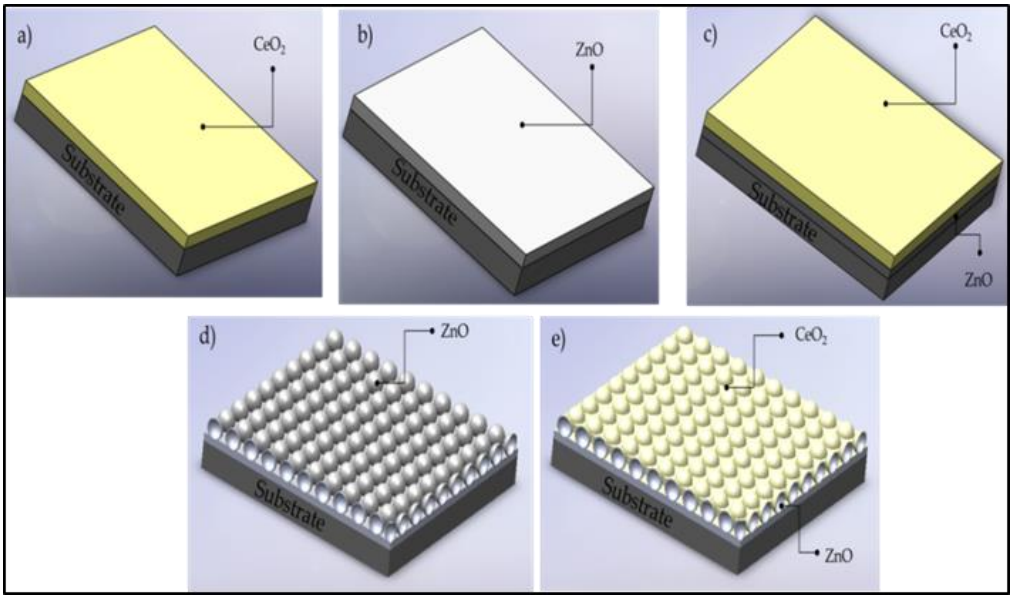

Figure 6.1: Morphologies used in this study: a) CeO_2, b) ZnO and c) CeO_2-coated ZnO films, and; d) ZnO and e) CeO_2-coated ZnO spherical nanoshell structures. All samples were deposited on both Si (100) and quartz substrates and have the same physical thickness of 120 $\pm$ 10 nm.

6.2 FILM SYNTHESIS

Prior to deposition, Si (100) and quartz substrates were cleaved to the desired size (2 × 2 cm) and the substrates were ultrasonically cleaned using acetone and a decontamination solution (30905 Aldrich) and then rinsed with deionised water and blown dry with a nitrogen stream. The ZnO layers used to generate ZnO films were prepared by a method initially proposed and demonstrated by Greene et. al. [195, 196] and further developed by Byrne et al. [76, 179, 194]. This method involved drop coating a mixture of zinc acetate

(5 mM) anhydrous ethanol solution onto the substrate surface. The solution is prepared by dissolving zinc acetate dehydrate in absolute ethanol (EtOH). This solution is then sonicated for up to one hour and allowed to cool in order to ensure a complete dissolution of the zinc acetate. A drop of this solution (typically 3.5 µl per cm^2) is applied to the previously cleaned substrate surface and allowed to spread across the surface. The droplet is then allowed to remain on the substrate surface for a period of 20 seconds before being rinsed with copious quantities of ethanol and dried with a nitrogen stream. This process is repeated approximately 60 times (each application yields approximately a film thickness of 2 nm). The substrates were then annealed at 350 °C for 30 minutes, to decompose the residual zinc salt into zinc oxide and yield a uniform textured nanocrystalline ZnO film with a film thickness of 120 ± 10 nm.

The nanostructured CeO_2 films are prepared on previously cleaned substrates by PDCMS using the same deposition procedures to the ones described in Chapter 3 and 4. The sputtering was performed in pure Ar atmosphere and the working pressure is adjusted and kept at 0.7 Pa for the duration of the sputtering. The sputtering is done at room temperature using a power of 65 W at 150 kHz and for 60 minutes. The process was repeated three times to yield a uniform CeO_2 film thickness of 120 ± 10 nm.

For the CeO_2-coated ZnO films, the substrate is coated with approximately 40 layers of the 5 mM zinc acetate solution to yield a uniform ZnO film thickness of 80 ± 10 nm. The sample is then transferred to the sputtering chamber to deposit a layer of nanostructured CeO_2 with an approximately 50 ± 10 nm thick film on top of the ZnO. This resulted in ~ 120 ± 10 nm thick CeO_2-coated ZnO film to allow for a straight comparison study. Figure 6.2 shows a process flow chart simplifying the deposition steps used to obtain the ZnO, CeO_2 and CeO_2-coated ZnO films.

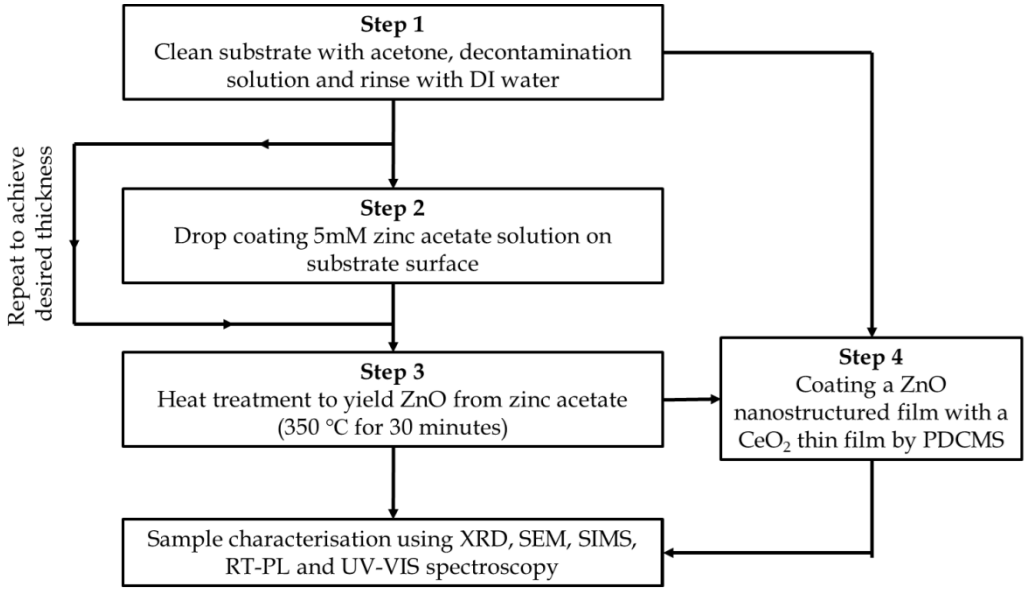

Figure 6.2: Flow chart of the overall process in the fabrication of ZnO, CeO_2, and CeO_2-coated ZnO films.

6.3 PATTERNED NANOSHELL SYNTHESIS

Patterned spherical ZnO nanoshells were fabricated on a PS sphere template using the same deposition method for the ZnO film. PS sphere template is a monolayer of PS spheres with a diameter of ca. 600 nm (solid content of ~ 10 wt. %, Fisher Scientific) that is generated by a self-assembly process on the surface of DI water (as detailed in in Chapter 5), at room temperature, and then transferred onto bare substrates [194]. The deposited close-packed PS sphere monolayer was then heated at 90 °C for 30 seconds to cause them to adhere better to the substrate surface without deforming the spheres [197]. This prevents the nanosphere monolayer lifting away from the substrate when the zinc acetate solution is applied. The PS spheres are then O_2 plasma treated at a power of 300 W, a pressure of 100 mbar, an oxygen flow rate of 50 sccm for 25 seconds, as highlighted in Chapter 5, to reduce the sphere diameter from ca. 600 nm to ca. ~ 520 nm allowing enough space between the spheres for a connected and mechanically stable ZnO nanoshell structure

post-deposition. Following the O_2 plasma treatment, a drop of the 5 mM zinc acetate solution is applied on the PS sphere coated substrate and allowed to spread across the surface. The droplet is then allowed to remain on the PS template and substrate surfaces for a period of 20 seconds before being rinsed with copious quantities of ethanol and dried with a nitrogen stream. This process is repeated approximately 60 times and 40 times to obtain nanoshell thicknesses of 120± 10 nm and 80 ± 10 nm, respectively. The samples are then annealed at 350 °C for 30 minutes, to decompose the residual zinc salt into zinc oxide. This temperature is higher than the softening temperature of the PS spheres. However, the SEM images below (Section 6.4.2) showed spherical ZnO nanoshell structures with voids which maintained their spherical shape post-annealing at 350 °C.

The ZnO spherical nanoshells with the nanoshell thickness of 80 ± 10 nm were then transferred to the sputtering chamber where a thin CeO_2 film of approximately 50 ± 10 nm is deposited on top of the ZnO nanoshells by PDCMS in an Ar environment, using the same deposition parameters reported in Section 6.2 and Chapter 3. This provided the sample shown schematically in Figure 6.1e. A process flow chart and three dimensional schematic images of the nanoshell structures are given in Figure 6.3 and 6.4, respectively. Figure 6.3 describes the fabrication process of the ZnO and CeO_2-coated ZnO spherical nanoshells.

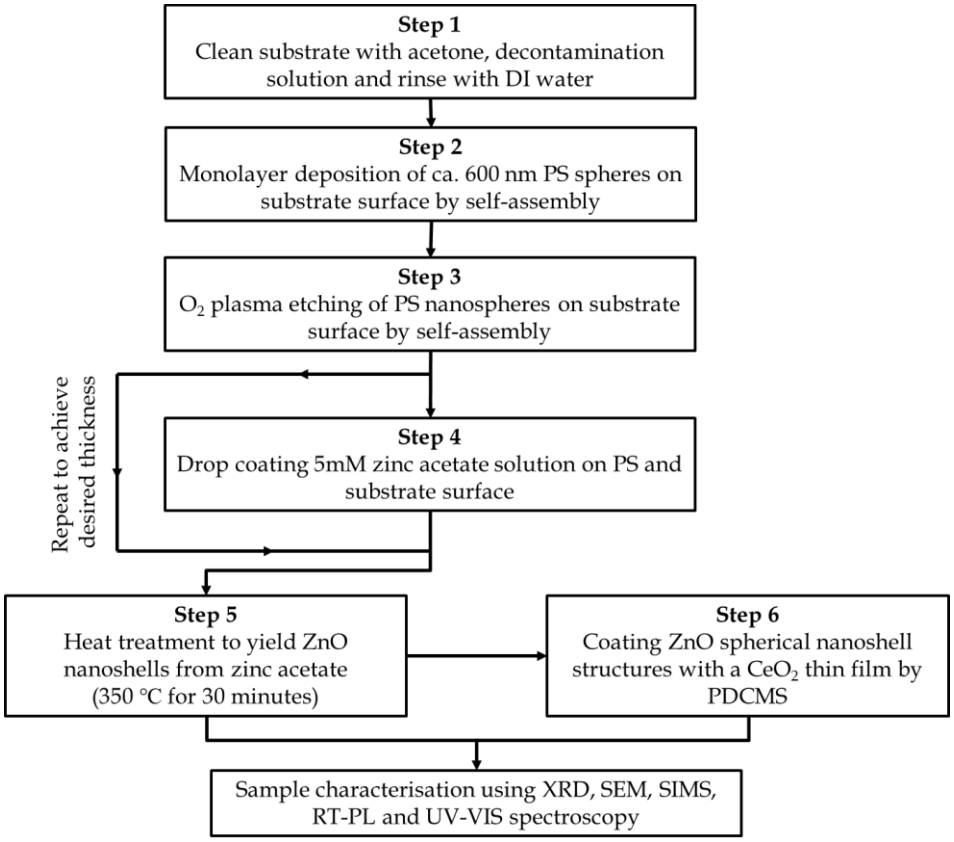

Figure 6.3: Flow chart of the overall process in the fabrication of ZnO and CeO_2-coated ZnO spherical nanoshell structures by zinc acetate drop coating and PDCMS deposition methods on bare substrates.

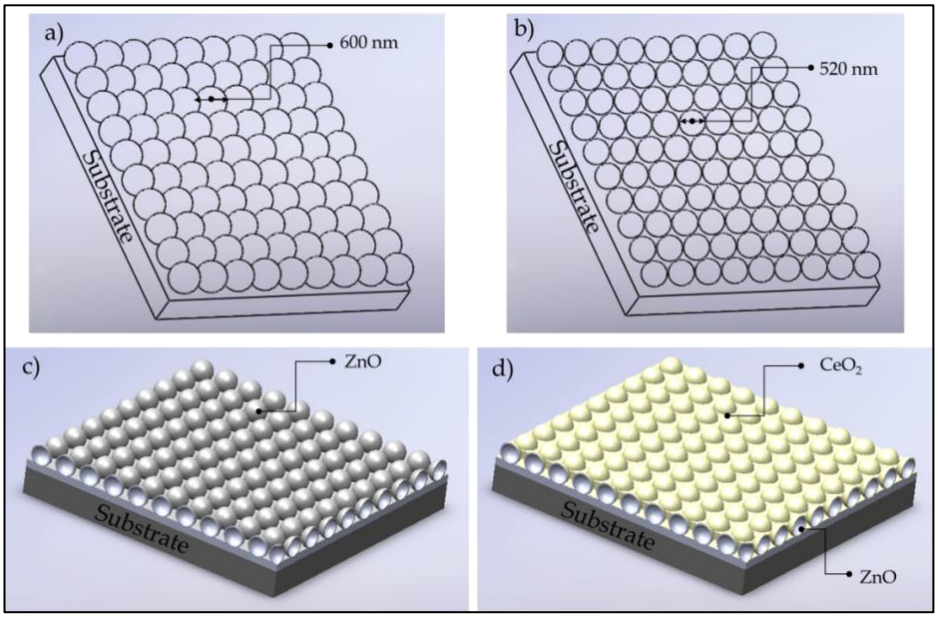

Figure 6.4: 3D images of a) a monolayer of the PS spheres deposited on the substrate surface, b) O_2 plasma etched PS spheres, c) ZnO spherical nanoshells and d) CeO_2-coated ZnO spherical nanoshells.

6.4 RESULTS AND DISCUSSION

To enable easy identification of samples, each structure used in this study is given an associated label which is summarised in Table 6.1. Note, the surface analysis of the ZnO seed layer and the sputtered CeO_2 films used in this chapter are obtained using XPS and further described in Appendix A.1 and Chapters 3 and 4, respectively.

Table 6.1: Associated labels for sample structures used in this study.

Sample Label	Sample Structure Description
C_F	CeO_2 Films
Z_F	ZnO Films
C_Z_F	CeO_2-coated ZnO Films
Z_NS	ZnO Nanoshells
C_Z_NS	CeO_2-coated ZnO Nanoshells

6.4.1 XRD OBSERVATIONS

XRD patterns of the Z_F and Z_NS structures, as-deposited and annealed at 500 °C and 800 °C in air for 30 minutes are shown in Figure 6.5. The XRD scans of all the Z_F and Z_NS structures show a dominant peak at 34.4°, corresponding to the (002) plane of the ZnO wurtzite phase (JCPDS card number 36-1451). This indicates the ZnO nanostructures are highly textured with their c-axis normal to the substrate [76, 198], which indicates that the nanocrystals in the seed layer remain textured normal to the substrate in both the film and nanoshell samples, and indicate the dominate effect of inter-nanocrystal basal plane interactions during deposition. The annealed Z_F structures also show two small peaks at 31.7° and 36.2° which correspond to the ZnO (100) and (101) planes, respectively

In the as-deposited Z_NS sample, two polystyrene ($(C_8H_8)_n$) related peaks are detected. These peaks are only present on the as-deposited

nanoshells as they were only annealed at 350 °C for 30 minutes during growth to decompose the zinc salt onto zinc oxide, which is less than the evaporation temperature needed to eliminate the PS spheres. A broad peak at 34.4° is detected indicating an intermediate nanocrystalline/poorly crystalline ZnO deposit. It is important to note that the samples annealed at 500 °C and 800 °C for 30 minutes have no remaining peaks associated with PS nanospheres. In these annealed nanoshell samples we once again see the dominant peak at 34.4°, corresponding to the (002) plane of the ZnO wurtzite phase, as well as two small peaks at 31.7° and 36.2° which correspond to the ZnO (100) and (101) planes, respectively.

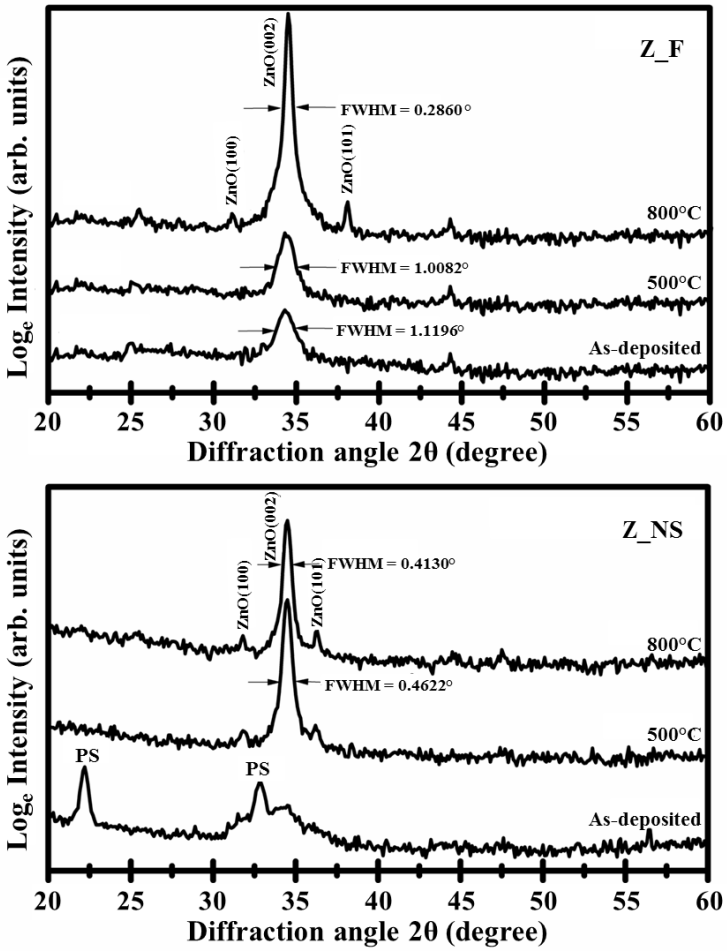

Figure 6.5: XRD θ/2θ scan (locked coupled) of Z_F (top) and Z_NS (bottom) structures grown on Si (100) substrates. The samples are as-deposited and annealed at 500 °C and 800 °C for 30 minutes. The dominant XRD peaks located at 34.4° correspond to the ZnO (002).

Similarly, the XRD patterns of the C_Z_F and C_Z_NS structures, as-deposited and annealed at 500 °C and 800 °C in air for 30 minutes, are shown in Figure 6.6. The XRD of the as-deposited films is similar to that of the Z_F structures as no peaks associated with CeO_2 are detected. This indicates the poorly crystalline nature of the as-deposited CeO_2 films, which is characteristic of as-deposited PDCMS CeO_2 films deposited on a smooth surface (see Chapter 3). However, as the C_Z_F structures are annealed at 500°C and 800 °C, more peaks are detected. These peaks are identified as either ZnO with wurtzite hexagonal structure (2θ = 34.4°) or CeO_2 (JCPDS card number 34-0394) with cubic structure (2θ = 28.5°, 33.0°, 47.4°, 56.3°, and 58.9°). Again, this indicates highly textured ZnO films with their c-axis normal to the substrate. No peaks assignable to Ce^{III} compounds, such as Ce_2O_3 and $Ce(OH)_3$ are seen in the pattern. However, a small peak indicated (*) is detected in the 500°C C_Z_NS structure whose origin has not yet been identified. Furthermore, two small peaks at 31.7° and 36.2° assigned to ZnO(100) and ZnO(101), respectively, are detected in the 800°C C_Z_F structures. There are no substantial differences between the XRD patterns of the C_Z_F structures compared to those of the C_Z_NS structures shown below, and the 800 °C annealed samples are virtually identical. The crystallinity of the CeO_2 and ZnO after the 500 °C anneal is much higher for the films compared to the nanoshell structures, based on the FWHM values of the dominant peaks. However, it is important to note that the XRD pattern of the as-deposited C_Z_NS structure displays all the peaks associated with both the CeO_2 and ZnO phases. The origin of this difference in crystallisation behaviour is not yet clear but has been explained in literature to possibly be caused by surface roughness, in our case due to presence of the PS monolayer (as highlighted in Chapter 5) and/or the ZnO nanoshell structure.

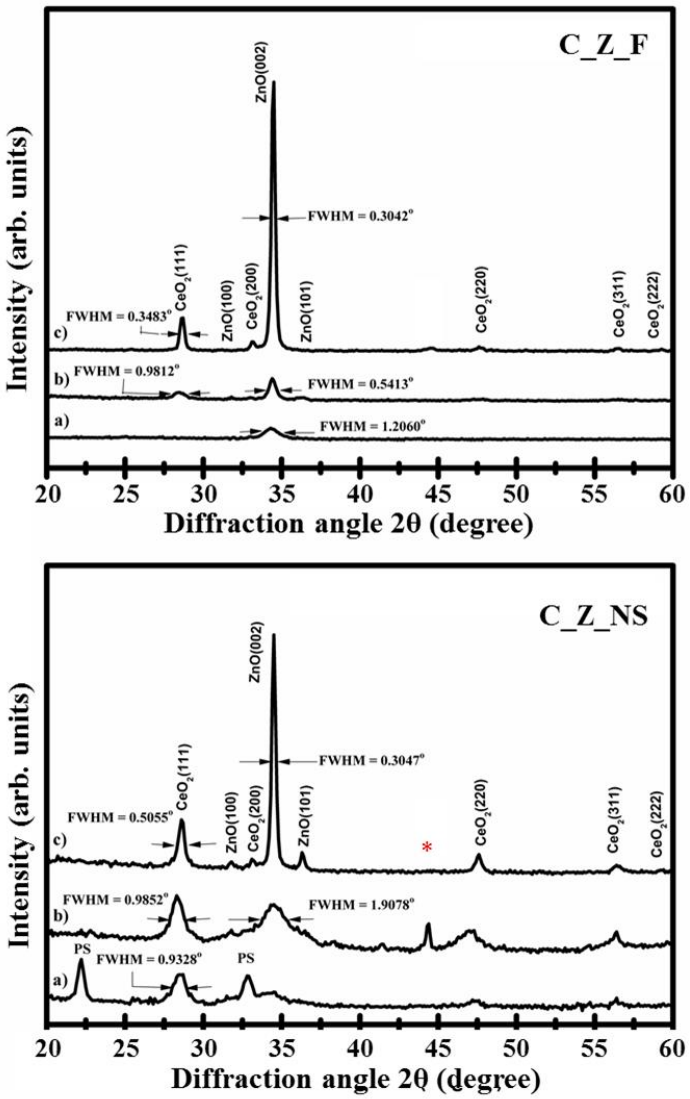

Figure 6.6: XRD θ/2θ scan (locked coupled) of C_Z_F (top) and C_Z_NS (bottom) structures grown on Si (100) substrates. The samples are a) as-deposited and annealed at b) 500 °C and c) 800 °C for 30 minutes. The dominant XRD peaks located at 34.4° and 28.5° correspond to the ZnO (002) and CeO_2 (111), respectively.

The reflected x-ray intensity and reflection peak FWHM of the CeO_2 (111) and ZnO (002) XRD peaks are used as an indicator of the crystallinity quality of the CeO_2 and ZnO deposits. As can be seen in Figure 6.5 and 6.6, an increase in the annealing temperature resulted in an increased XRD reflection intensity and a decrease of the FWHM of the CeO_2 (111) and ZnO (002) XRD peaks (similar to results reported in Chapter 4). In the 500 °C annealed C_Z_F, structure for example, FWHM values of 0.9852° and 1.9078°

are measured for CeO_2 (111) and ZnO (002) XRD peaks, respectively. These values decreased to 0.5055° and 0.3047° for the samples annealed at 800 °C. This trend is the same for all the other ZnO and CeO_2-coated ZnO samples (see Table 6.2); indicating that the crystalline quality of the samples is systematically improved as a result of annealing.

.

Table 6.2: Summary of the FWHM values of the ZnO(002) XRD peaks of the various samples.

	FWHM (°)		
Sample	**As-deposited**	**Annealing Temperature (°C)**	
		500	**800**
Z_F	1.1196	1.0082	0.2860
Z_NS	-	0.4622	0.4130
C_Z_F	1.2060	0.5413	0.3047
C_Z_NS	-	1.9078	0.3047

6.4.2 SEM OBSERVATIONS

Following the initial preparation stages (deposition and O_2 plasma treatment of the PS nanosphere monolayer template, described in detail in Chapter 5) in order to create the ZnO nanoshell structures and the deposition of the zinc acetate films on the PS spheres, the structural morphology of the ZnO deposits depended on the post-deposition annealing temperature. Figure 6.7 shows the plan view of the zinc acetate decomposed into ZnO nanostructures by annealing the sample at 350 °C for 30 minutes. Spherical nano core-shell structures consisting of the PS sphere core and ZnO shell with a total diameter of ca.~ 600 nm are formed, as shown in Figure 6.8. The thickness of the ZnO is estimated to be ~ 80 nm on the CeO_2 coated ZnO sample, as shown in the cross sectional view of the fractured nanostructures (Figure 6.8e and f). Other views of the spherical nanostructures, after a complete removal of the PS spheres by gasification (i.e. following annealing

at 500 °C for 30 minutes in air) and the addition of the thin CeO_2 film (~ 50 ± 10 nm thick), are also shown in Figure 6.8b, c, d and e.

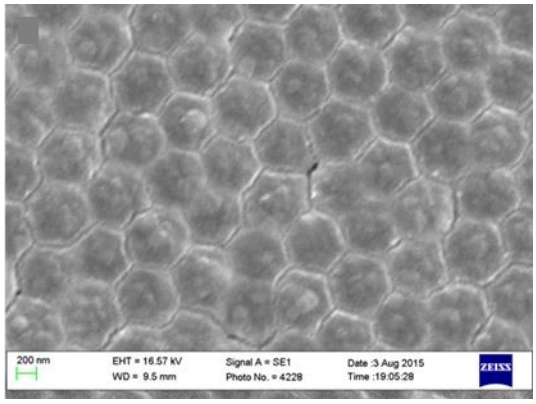

Figure 6.7: Plan view SEM image of the spherical ZnO nanoshells before complete removal of PS nanospheres i.e. simply heated at 350 °C for 30 minutes to decompose the zinc acetate into zinc oxide.

6.4.3 CHEMICAL COMPOSITION

To provide information on the chemical composition and impurity content in the samples and confirm the composition of the C_Z_F structure, SIMS measurements were undertaken at different locations throughout the deposit. Figure 6.9 shows the SIMS spectra of the C_Z_F structure for the mass region from 60 amu/e to 200 amu/e at the boundary where the two materials meet. As reported previously [106], sputtered CeO_2 SIMS spectra showed an intense secondary ion peak of CeO^+ and two lower intensity peaks of Ce^+ and CeO_2^+. This can be clearly observed in Figure 6.9 (spectrum 370). As more scans are performed and the probing depth increased due to surface sputtering by the Ga ion beam, Zn+ and ZnO^+ peaks start to appear and their intensity increased with the increase in the number of scans. Three different Zn isotopes are observed for the Zn ions, ^{64}Zn, ^{66}Zn and ^{68}Zn, with the highest intensity observed for the ^{64}Zn isotope, consistent with the natural isotopic distribution. SIMS spectra from Z_F structure displayed similar peaks to that of spectrum 490 in Figure 6.9, with a constant intensity for all the Zn and ZnO peaks throughout the sample. Note that (i) the

intensity of the peaks depend significantly on the sputtering rate of the components during the SIMS scan and (ii) that each spectrum is taken over a 10.2 second sputtering period i.e. spectrum 370 is recorded after 62.9 minutes (3774 seconds) total sputtering time.

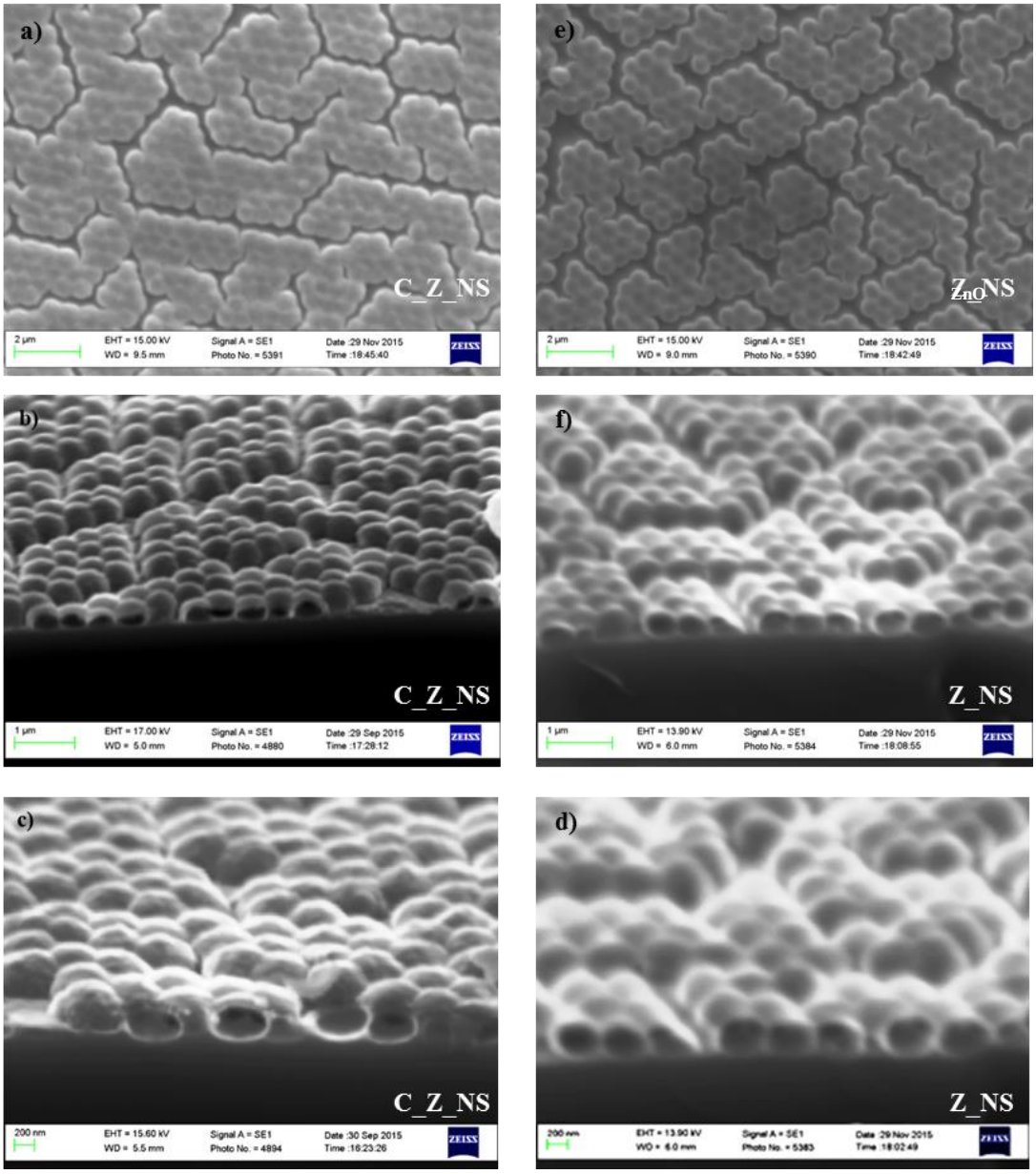

Figure 6.8: SEM images of the spherical nanoshell structures after the removal of the PS spheres (i.e. annealed at 500 °C for 30 minutes in air). The samples are deposited on both Si (100) and quartz substrates. The SEM images show the a) and d) plan view, b) and e) 60° view, c) and f) zoomed 60° view of the Z_NS (right) and C_Z_NS (left) structures with a clear evidence of the internal voids following PS sphere removal.

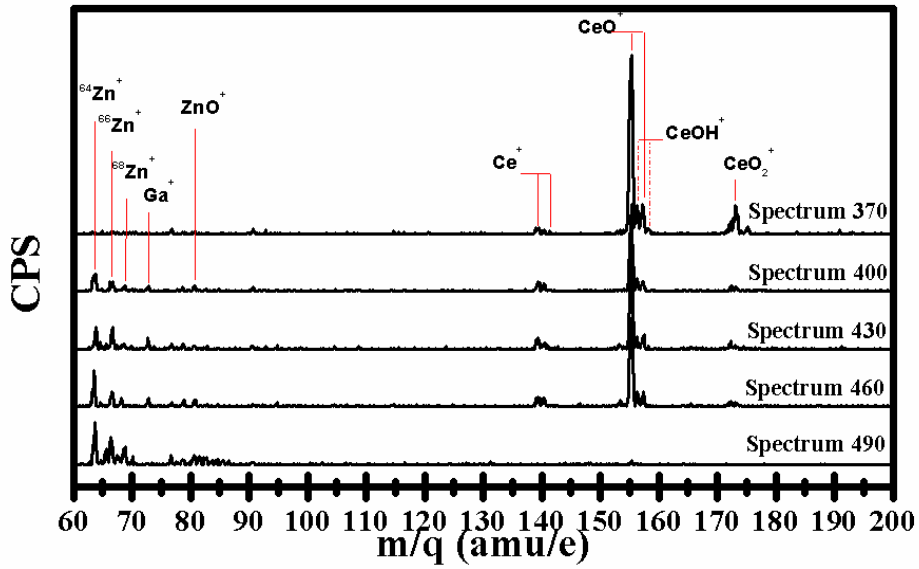

Figure 6.9: SIMS spectra of positive secondary ions at the boundary of the C_Z_F and C_Z_NS structures. Increasing spectrum number indicates increased overall sputtering time, as discussed in the main text.

The SIMS depth profiling data of the relative secondary ion emission yields ($^{64}Zn^+$, Ce^+, CeO^+ and CeO_2^+) as a function of depth at the boundary of the CeO_2-coated ZnO composite layers grown on Si(100) substrate is presented in Figure 6.10. Since the sputtering rate of the different ions varies from one element or compound to another, the count intensity or observed signal strengths are not directly inter-comparable in terms of chemical concentrations. Multiple scans are performed at the same location on the C_Z_F structure. An almost uniform signal level is seen for the Ce^+, CeO^+ and CeO_2^+ ion profiles throughout the CeO_2 layer at depth numbers between 1 and 310. As the exposure time increased, the effect of surface sputtering also increased resulting in a deeper penetration through the films. Therefore, a significant decrease in magnitude of the CeO^+ count intensity with respect to the Ce^+ and CeO_2^+, and an increase of the $^{64}Zn^+$ count intensity is seen, indicating the location of the ZnO/CeO_2 interface. Although a significant reduction of CeO^+ intensity is recorded as the Zn signal begins to increase, it remains the signal with the highest intensity. The SIMS data show clear

evidence of an abrupt interface between the ZnO and CeO_2 materials. The difference in intensities is due to the sputtering rates of the various elements and components and therefore, lower intensities are recorded for Ce^+ and CeO_2^+.

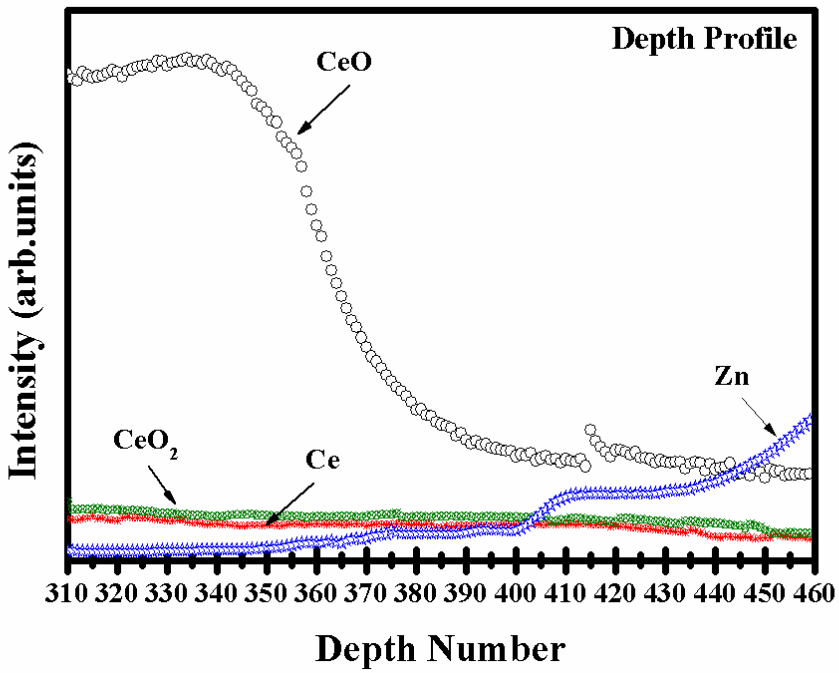

Figure 6.10: Relative secondary ion emission yields for Zn, Ce, CeO and CeO_2 positive ions as a function of depth at the boundary of the composite C_Z_F structure grown on a Si (100) substrate.

6.4.4 UV-VIS ABSORPTION AND BANDGAP ENERGY

The optical properties of the as-deposited samples (C_F, Z_F C_Z_F, Z_NS and C_Z_NS) were investigated by spectroscopic measurements. The optical absorbance spectra of the films deposited on quartz substrates are recorded in the wavelength range from 200 to 800 nm. Typical absorbance curves for the films are shown in Figure 6.11. The influence of adding a CeO_2 film to the ZnO film is clearly observed in these absorbance spectres. The C_Z_F structure has high absorption in the UV and visible regions followed by a fall-off in the absorption at wavelength greater than approximately 380 nm.

Both pure C_F and Z_F structures (with approximately the same film thickness of 120 ± 10 nm) have lower absorbance in the visible region and the absorbance spectra of the composite C_Z_F structure seems to be due to the joint effects of the two constituent oxides. Torres-Huerta et al. [176] attributed this behaviour to the introduction of CeO_2 defective states within the forbidden band, which may lead to absorption of incident photons in the visible region. Therefore, adding CeO_2 to the ZnO films clearly increases the absorption in visible and UV spectral regions. It's important to note that although the thicknesses of the CeO_2 films is greater than that described in Chapter 5, the UV-Vis absorbance spectra for both samples are almost identical.

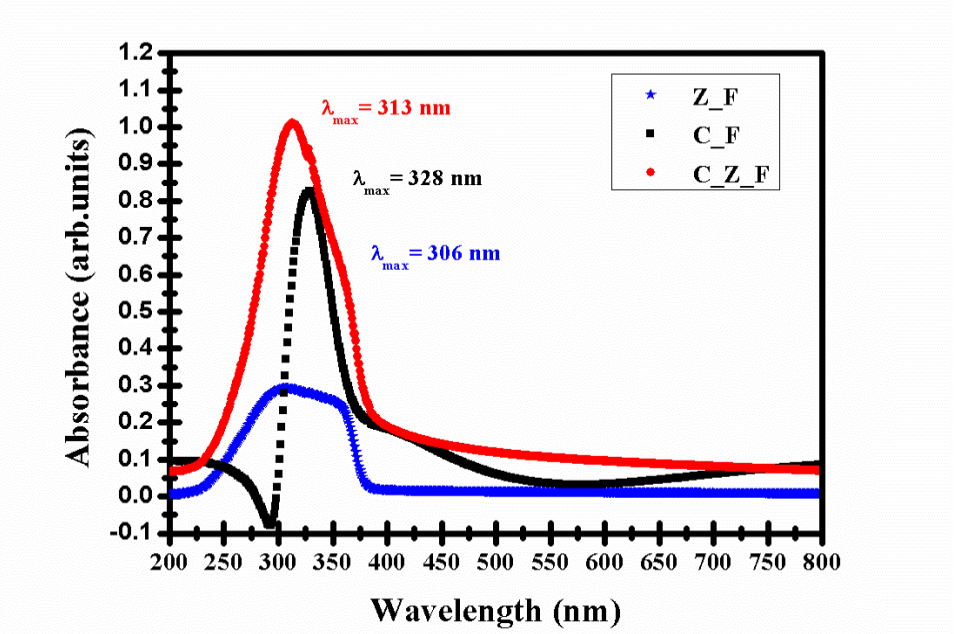

Figure 6.11: Room temperature UV-Vis absorbance spectra of Z_F, C_F and C_Z_F (thickness ~ 120 ± 10 nm) on quartz substrates.

By analysing the absorption data using Tauc plots of $(\alpha h\nu)^n$ versus hν [199], where α is the measured absorption coefficient, the optical bandgap (E_g) can be determined and, ideally, can distinguish between allowed direct (n =2), forbidden direct (n = 2/3), allowed indirect (n = 1/2) and forbidden indirect (n = 1/3) transitions. However, the interpretation of data can be

subjective and is not always conclusive. In Figure 6.12, absorption data for the film samples (C_F, Z_F and C_Z_F) are analysed in the form of Tauc plots for the allowed direct ($(\alpha h\nu)^2$) optical transitions. From the Tauc plot (Figure 6.12), it can be clearly seen that the extracted bandgap value for pure Z_F sample is 3.26eV which is a close match to the typical ZnO band gap value of 3.3 eV. On the other hand, the value of the extracted optical band gap for pure C_F sample is 3.44 eV, which is greater than the as-deposited CeO_2 bandgap value reported in Chapter 4 (3.04 eV for film thickness of 50 ± 10 nm). It is also higher than the direct bandgap values reported on fully oxidised CeO_2 films (3.01 – 3.1 eV) [200] and bulk CeO_2 powder (3.19 eV) [201]. However, this estimated bandgap value (E_g = 3.44 eV) for CeO_2 is in close agreement with other reported direct bandgap values for CeO_2 nanoparticles [147, 202-204]. This mismatch can be explained in terms of the cerium oxide structures (stoichiometric and non-stoichiometric) forming the film as a result of the sputtering process [106]. Finally, the bandgap energy extracted for the C_Z_F structure is 3.25 eV, which is very close to that of the Z_F structure. Hence, the C_Z_F structure shows higher UV-Vis absorption in the visible region than pure oxides (ZnO and CeO_2) as a consequence of the addition of CeO_2 to the ZnO structure.

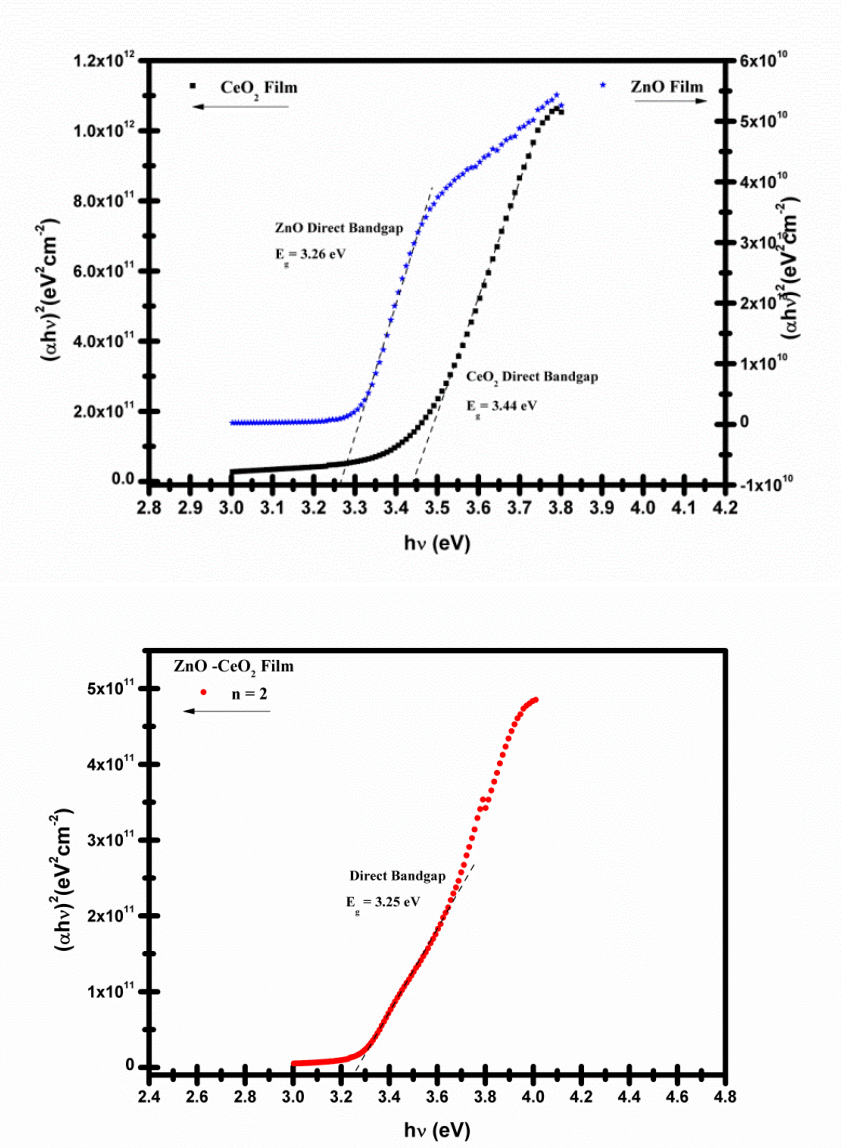

Figure 6.12: Tauc plot of $(\alpha h\nu)^2$ as a function of photon energy ($h\nu$) for C_F, Z_F (top) and C_Z_F (bottom) samples.

Figure 6.13 shows the UV-Vis absorption spectra of the pure Z_F, C_Z_F, Z_NS and C_Z_NS samples, with the same physical thicknesses of the two materials in both the planar and nanoshell morphologies. All samples are annealed at 500 ˚C in air for 30 minutes in order to completely eliminate the PS spheres from the nanoshell samples and to enable a direct comparison between the nanoshells and the films. Other Z_F, C_F, Z_NS and C_Z_NS samples were also annealed at 800 ˚C to crystallise the materials;

however, no significant differences in absorption, compared to samples annealed at 500 ˚C, are seen in these samples (similarly to results reported in Chapter 4, Section 4.3.3). It can be clearly seen in Figure 6.13 that pure Z_NS and C_Z_NS samples exhibit a much higher UV light absorption level of ~ 3 times and 1½ times the comparable thin film absorption, respectively. This strongly confirms that a significant enhancement in the UV light absorption is achieved by the engineered spherical nanoshells, for identical sample material thicknesses; hence the geometry of the structure dramatically improves the absorption. It is important to note that the sharp peak at ~ 330 nm is due to an instrumental artefact (change in grating response) as it is detected in most of our UV-Vis absorption spectra. The samples with the nanoshell morphologies also show distinctly higher apparent absorption in the visible region, compared to equivalent thickness samples with thin film morphologies. We believe that this is due to the effects of increased light scattering and diffraction of energy out of the incident beam, due to the ordered spherical nanoshell structures, which have a periodicity of similar order (600 nm) to visible light wavelengths. Note that the engineering of these spherical nanoshells not only enhanced the optical properties, it has also increased the surface to volume area by a factor of 7.8 times that of a planar (using the mathematical model 2 described in Chapter5). This increase in surface area, combined with the enhanced light management obtained, should increase the redox activities and improve the solar-driven thermochemical process.

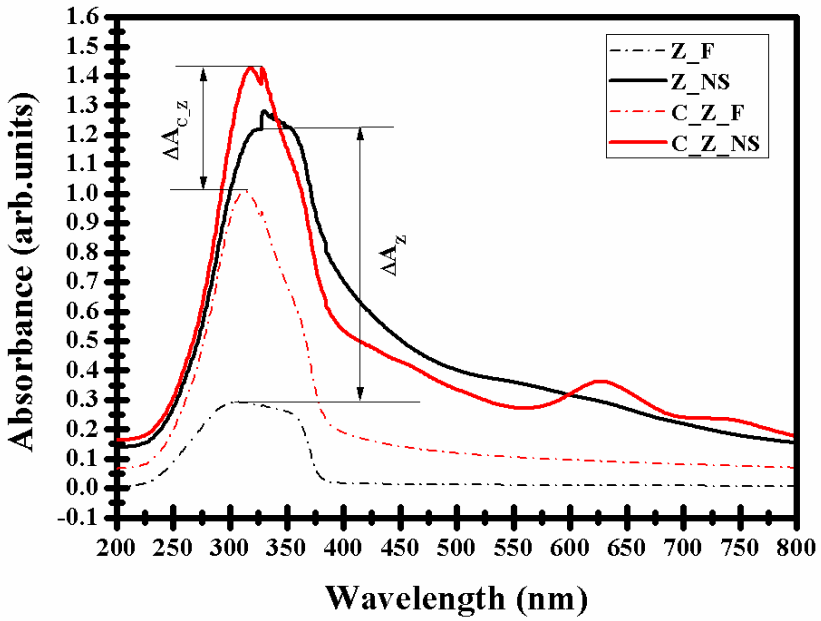

Figure 6.13: Room temperature UV-Vis absorption spectra of Z_F, C_Z_F, Z_NS and C_Z_NS samples, under normal incidence, with a clear indication of an increase in the absorption (ΔA) as a result of the nanoshell structure geometry.

6.4.4.1 DIRECTIONALITY STUDIES

The absorbance enhancement is also relatively insensitive to the angle of incidence as shown in Figure 6.14. Spectrally integrated over the wavelength range of 300 – 800 nm, the relative absorbance enhancement shows a maximum variation of less than 30% between values measured at normal incidence and at an incidence angle of 70° from the normal for both the C_Z_NS and Z_NS samples, compared to the relevant thin film samples. This variation is significantly lower than the one reported, in Chapter 5, for the CeO_2 dome-shaped nanostructures (50%). Although the UV-Vis absorbance spectra of the dome-shaped nanostructures displayed higher values than the spherical nanoshell structures, these results cannot be directly compared due to the different metal-oxides used. Note also that the relative absorbance

enhancement at angle $i°$ is calculated using the same formula (Equation 5.1) provided in Chapter 5, Section 5.5.3.

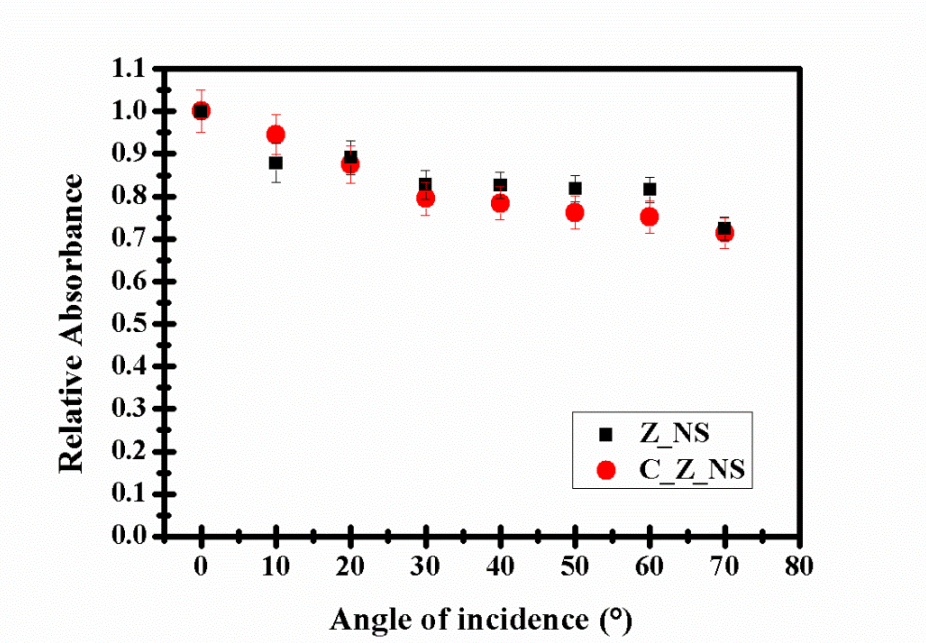

Figure 6.14: Integrated relative absorbance for different incidence angles relative to normal incidence for samples Z_NS and C_Z_NS.

6.4.5 PHOTOLUMINESCENCE

The luminescence properties of the Z_F, C_Z_F, Z_NS and C_Z_NS structures are investigated and shown in Figure 6.15. The high intensity luminescence peak is related to ZnO and this strong emission at around 3.31 eV (375 nm) is in close agreement with the previous reports from room temperature PL studies of ZnO [205, 206]. There is a significant reduction of the intensity of the PL peaks in the Z_NS and C_Z_NS samples with respect to the Z_F and C_Z_F samples. This can be explained as being due to the uneven surface, which will reduce the focusing effect of the laser, since the spectrometer slit size used, is approximately 1 μm. The FWHM of the strong PL spectra of C_Z_F structure obtained using Gaussian fitting is approximately 0.1795 eV. No PL peaks are observed associated with CeO_2.

Moreover, three very low intensity peaks are observed at 3.74 eV (332 nm), 3.67 eV (338 nm) and 3.60 eV (344 nm) in Figure 6.15, whose origin is the subject of ongoing study, but which do not appear to be associated with laser plasma line emission leakage, as shown in Figure 6.16.

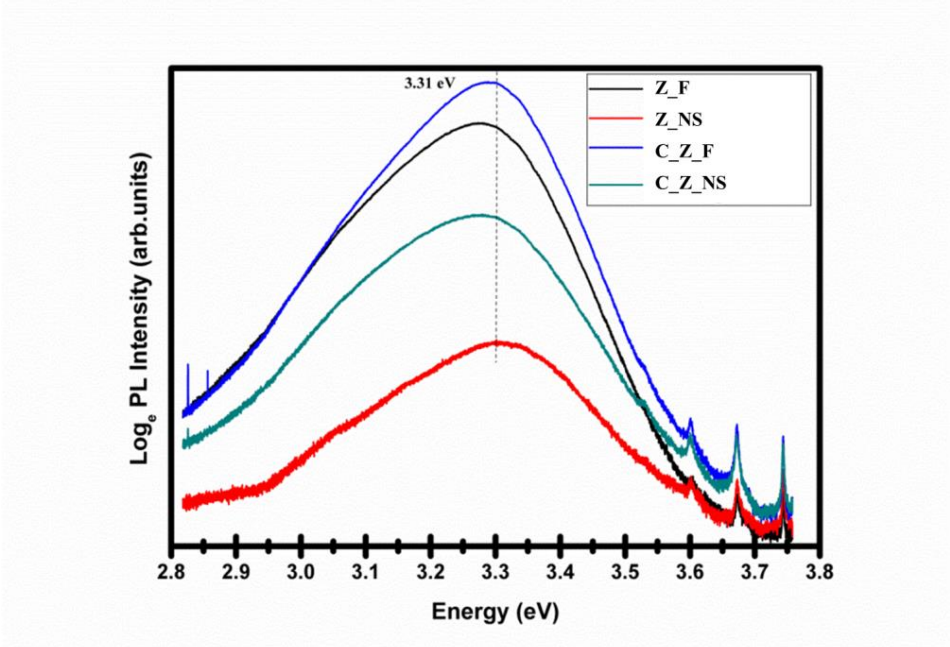

Figure 6.15: Room-temperature PL spectra of Z_F, C_Z_F, Z_NS and C_Z_NS samples.

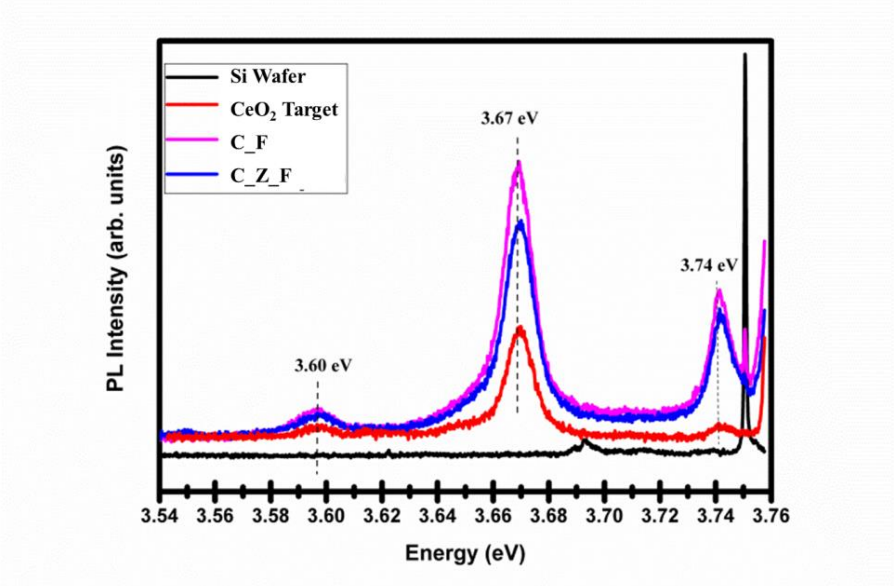

Figure 6.16: Room-temperature PL spectra of the short wavelength emission region for metal-oxide films in the range of 3.6 – 3.75 eV, compared to the emission seen from a bare Si wafer under identical conditions.

6.5 CONCLUSIONS

In this chapter, we have demonstrated a simple and reproducible method to fabricate ZnO and CeO_2-coated ZnO films and nanoshell structures on Si (100) and quartz substrates. The ZnO nanostructures are grown by a facile drop coating method using zinc acetate in anhydrous ethanol solution as a starting material, while the CeO_2 are produced by a PDCMS method, similar to the films produced in Chapter 3, 4 and 5. XRD, SEM and SIMS measurements confirmed the structural, morphological and compositional properties of the deposited materials. In particular, XRD data indicated an amorphous/poorly crystalline nature of the as-deposited ZnO and CeO_2 nanostructures and the crystalline quality improved after post-deposition annealing at higher temperatures. SEM images showed the successful engineering of the spherical nanoshell structures with a clear indication of the central voids. SIMS analysis of the chemical composition showed the presence of the Ce^+, CeO^+, CeO_2^+, Zn^+ and ZnO^+ ionic species in the various relevant samples as well as the three different Zn isotopes (^{64}Zn, ^{66}Zn and ^{68}Zn), and depth profiling showed the location of the ZnO/CeO_2 interface in relevant samples. UV and visible light absorption is very significantly enhanced through the engineering of spherical nanoshells on a PS monolayer template, most likely due to the whispering gallery modes in such nanoshell cavities, as well as the addition of the CeO_2 layer. The reported results and analysis clearly show that key materials properties such as the UV and visible light absorption can be significantly enhanced by nanostructure engineering of the deposits to create spherical nanoshell cavities. They had a maximum absorbance enhancement variation of less than 30% between normal incidence and incidence at 70° from the normal, which is much lower than the variation resulted from the dome-shaped nanostructures (described in Chapter 5). These results are important in terms of enabling future

materials and device developments, with the aim of controlling key film parameters for technologically important applications. In particular, in the areas of solar-thermal fuel generation and catalysis, the combination of spherical nanostructure engineering possible with ZnO materials combined with the oxygen storage and variable stoichiometry properties of CeO_2 will provide an unique set of advantageous material and structural properties.

Chapter 7

CERIA WET CHEMICAL GROWTH AND CHARACTERISATION

7.1 INTRODUCTION

Spin coating, a solution-based (wet chemical) deposition process, is used to deposit thin CeO_2 films in standard atmospheric environments from a cerium nitrate solution. As mentioned in Chapter 2, this kind of technique offers the advantage of a simple, low cost and high throughput process that enables the fabrication of high performance and ultra-low-cost CeO_2 thin films for many industrial applications. In this chapter, detailed accounts of the substrate and the cerium salt chemical solution preparation are provided in sections 7.2 and 7.3, respectively. After the decomposition of the cerium nitrate solution into CeO_2 thin films by applying thermal anneal, a successful nanocrystalline CeO_2 film with a uniform thickness of 40 ± 5 nm is produced. The structural and elemental analysis of these decomposed CeO_2 films are examined using XRD, SIMS, XPS and EDX, as described in section 7.5. Moreover and due to the simplicity and effectiveness of this wet chemical deposition method,

increasing the surface area to volume ratio via spherical nanoshell structures was possible. Therefore, various attempts were conducted in order to generate spherical nanoshell structures on a PS nanospheres template. Unfortunately, these attempts were unsuccessful as explained below, mainly due to the high value of the thermal anneal temperature required to decompose the cerium salt solution deposit into pure CeO_2 films. Due to the unsuccessful attempts of engineering the nanoshell structures using this deposition method, other metal-oxides such as ZnO (further detailed in Chapter 6), with lower Zn salt to pure ZnO decomposition temperature, were considered as an alternative option to engineer the spherical nanoshell structures.

7.2 SUBSTRATE PREPARATION

The Si(100) substrates (SIGMA ALDRICH) are cleaved into pieces (2 cm × 2 cm). Clean dry air is then blown on the substrate to get rid of any debris from the cleaving. The Si(100) substrates are then rinsed by DI water (obtained from a Millipore filtration system) and etched with a base piranha solution to remove any organic residue on the surface prior to spin coating. The base piranha etch solution is a mixture of three parts ammonium hydroxide (NH_4OH) and one part hydrogen peroxide (H_2O_2). The mixture will oxidise and remove organic materials present on the surface leaving behind a clean surface. The reaction is not self-initiating under normal conditions; hence it is necessary to heat the mixture to 100 °C to start the reaction. The Si(100) pieces are immersed in the mixture for 45 minutes to complete the cleaning process. The pieces are then removed from the etch solution and rinsed thoroughly with DI water. The pieces are left in a clean container immersed in DI water to avoid any further contamination, and are dried using clean compressed air prior to the wet chemical deposition process. The quartz

substrates are also cleaved into pieces of ~ 2 cm × 2 cm. However, the quartz substrates are cleaned differently. They are ultrasonically cleaned using acetone, a decontamination solution (30905 ALDRICH), DI water and blown dry with a nitrogen stream to remove any surface contamination.

7.3 CHEMICAL SOLUTION PREPARATION

The chemical solution used to obtain the polycrystalline CeO_2 films, as briefly described in Chapter 2, is prepared by placing 2g of cerium (III) nitrate hexahydrate ($Ce(NO_3)_3.6H_2O$, 99% purity, purchased from Sigma-Aldrich) and 0.2g of 10% polyvinyl alcohol (PVA, prepared from 99+% PVA purchased from Sigma-Aldrich) in 20 ml DI water. The solution is then stirred, using a magnetic stirrer, for three hours to ensure a complete dissolution. A small puddle (~1 ml) of the fully dissolved chemical solution is dropped onto the centre of the pre-cleaned substrate, which is rotated to form a film of the chemical solution material onto the substrate. This is then decomposed to yield pure polycrystalline CeO_2 films, as detailed below.

7.4 DEPOSITION PROCESS

Thin films of CeO_2 are prepared by a spin coating process where ~1 ml of CeO_2 salt solution (described in section 7.3) is deposited on 2 × 2 cm Si(100) and quartz substrates. Prior to the deposition, the substrates are cleaned using the methods described in Section 7.2. A spin coater supplied by Laurell Technologies Corporation (highlighted in Chapter 2) is used to spin coat CeO_2 salt solution on the substrates. The spin coating process is completed in air and the substrates are held in position using a vacuum. The spin coating parameters are adjusted to a spin velocity of 3000 rpm, a spin acceleration of

540 rpm/s and a spin time of 40 s to obtain a uniform film thickness of 40 ± 5 nm for all deposited samples (thicknesses of the final decomposed CeO_2 layers are measured using spectroscopic ellipsometry). The number of spin coating layers used to obtain the film thickness value of 40 ± 5 nm is ten layers, where each layer was left in air for 5 minutes to dry before the next deposited layer was added. Note, there were no other curing methods required between applications.

The chemical solution used has two components, $Ce(NO_3)_3.6H_2O$ and PVA which need to be decomposed in order to produce a pure nanocrystalline CeO_2 film. This $Ce(NO_3)_3.6H_2O$/PVA to CeO_2 decomposition is achieved by annealing the samples after completing the spin coating deposition process and a short contact time with air at room temperature. The decision on the annealing temperature was finalised, after a variety of literature was reviewed on the decomposition of $Ce(NO_3)_3.6H_2O$ and the elimination of the PVA. Vratny *et al*. [207] and Srydom *et al*. [208] reported that $Ce(NO_3)_3.6H_2O$ fully decomposes at 400°C to produce CeO_2 [209]. PVA undergoes various reactions at different temperatures; however it can be fully eliminated at 500 °C [210]. Therefore, the deposit samples are transferred into a quartz glass cell, where annealing treatment is performed. Figure 7.1 shows a graphical representation of the annealing cell and the annealing parameters used to yield the pure nanocrystalline CeO_2 films. Samples are ramped up to a target temperature of 400 °C at a rate (r) of 40 °C min^{-1} in an air ambient and held at these temperatures for 30 minutes (the dwell time, t_d). It is then further annealed at a temperature of 500 °C, at a ramp rate of 40 °C min^{-1}, for another 30 minutes to complete the decomposition reaction and yield pure nanocrystalline CeO_2 films. Another sample was produced by annealing the cerium salt deposit at 400 °C for 30 minutes and annealing it at the higher temperature of 800 °C for another 30

minutes, again using a ramp rate of 40 °C min^{-1}. Table 7.1 summaries the samples used in this chapter with their associated labels.

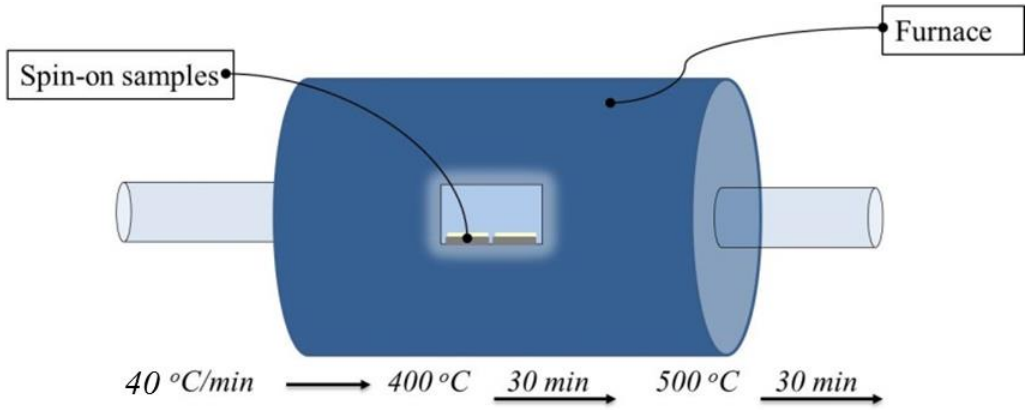

Figure 7.1: A schematic representation of the annealing furnace and annealing parameters used to decompose the chemical solution to yield pure nanocrystalline CeO_2 films.

Table 7.1: Summary of decomposed CeO_2 thin film deposits, with their associated labels.

Label	Description
400 °C-500 °C CeO_2	CeO_2 thin film yield by decomposing cerium nitrate and PVA deposits by post-deposition annealing sample at 400 °C and 500 °C for 30 minutes at each temperature.
400 °C-800 °C CeO_2	CeO_2 thin film yield by decomposing cerium nitrate and PVA deposits by post-deposition annealing sample at 400 °C and 800 °C for 30 minutes at each temperature.

7.5 RESULTS AND DISCUSSION

As discussed in Chapter 2, the selection of suitable spin coating parameters for the development of good quality, uniform decomposed pure CeO_2 film deposits are important and can only be obtained after several repetitions of

the experiments, by varying the spin parameters. The optimisation of the process conditions is established by observing the structural, morphological and optical properties of the films. Most importantly, the impact of various spin parameters such as spin speed (rpm), spin acceleration (rpm/s) and spin time (s) on the thickness (nm) and thickness uniformity (%) of the deposited films are studied. To begin, the spin time is fixed at 40 s since the longer the spin time, the thinner the film and 40 s gave a suitable film thickness of ~ 40 nm. It is important to note that this average thickness value is obtained as a result of ten separate spin coating layers. The typical spin speed value from literature is found to be 3000 rpm [211, 212]. Therefore, the impact of spin acceleration on the quality of the film is investigated first. The spin speed value and spin time are kept constant at 3000 rpm and 40 s, respectively. Figure 7.2 shows the average thickness and thickness uniformity of the decomposed CeO_2 film (400 °C – 500 °C) generated by depositing cerium salt at spin accelerations of 90, 180, 270, 540, 990, 1530, 2160 and 2970 rpm/s.

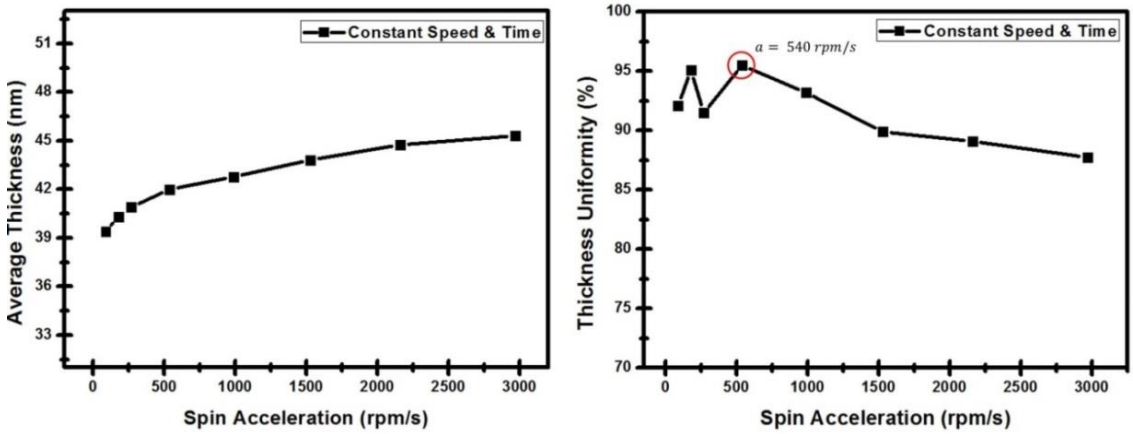

Figure 7.2: The impact of spin acceleration (a) on the average thickness and thickness uniformity of the 400 °C – 500 °C CeO_2 film, $v_{constant}$ = 3000 rpm and $T_{constant}$ = 40s.

The average thickness values obtained after the deposition of ten layers, for the samples are within the 39 – 45 nm range. However, the thickness uniformity is above 90% for all acceleration values except for 1530,

2160 and 2970 rpm/s, with the highest thickness uniformity (95.5%) for a spin acceleration value of 540 rpm/s. This acceleration value is then used to find the optimum spin speed value.

Although the typical spin speed value used in literature and industries is 3000 rpm, the impact of the spin speed on the average thickness and thickness uniformity is investigated and the results obtained are shown in Figure 7.3. The initial speed value used is 2000 rpm. The speed is then increased, in increments of 500 rpm to 5000 rpm.

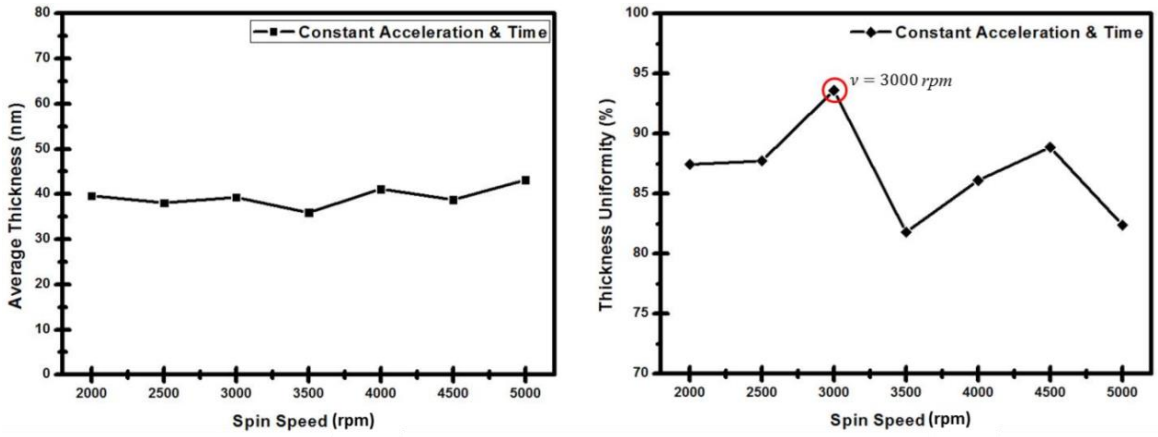

Figure 7.3: The impact of spin speed (v) on the average thickness and thickness uniformity of the 400 °C – 500 °C CeO_2 film, $a_{constant}$ = 540 rpm/s and $T_{constant}$ = 40s.

The thickness values are then measured, at ten different locations, using spectroscopic ellipsometry and the thickness uniformity is calculated using Equation 7.1.

$$\text{Uniformity (\%)} = \left(1 - \frac{t_{max} - t_{min}}{t_{average}}\right) \times 100 \qquad (7.1)$$

where t_{max} is the maximum thickness, t_{min} is the minimum thickness and $t_{average}$ is the average thickness of a spin coated decomposed CeO_2 deposit.

Based on the outcomes of these investigations, the optimised spin coating parameters are used to obtain a uniform decomposition of a pure nanocrystalline CeO_2 film with a thickness of 40 ± 5 nm. Figure 7.4 shows the plan view SEM image of the decomposed CeO_2 film using cerium nitrate as a

starting material. These optimum parameters are summarised in Table 7.2 and they are used to deposit the CeO_2 films characterised below.

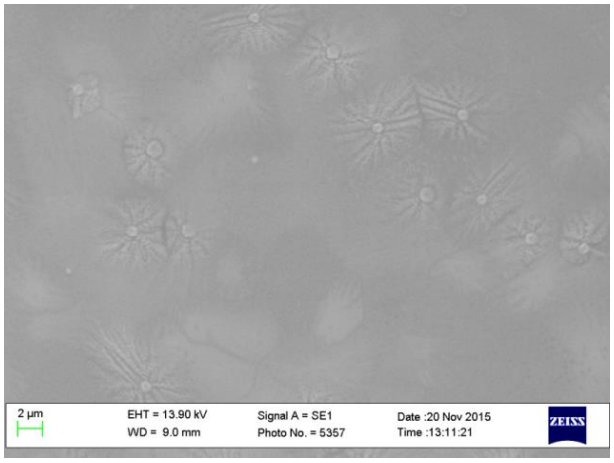

Figure 7.4: Plan view SEM image of the decomposed 400 °C -500 °C CeO_2 film deposited by spin coating using cerium nitrate as a starting material to yield CeO_2.

Table 7.2: Optimised spin coating parameters to obtain the decomposed CeO_2 films with uniform thicknesses of 40 ± 5 nm, after ten distinct coating layers.

Parameter	Symbol	Value	Unit
Spin Time	T	40	S
Spin Speed	*V*	3000	Rpm
Spin Acceleration	*A*	540	rpm/s

7.5.1 STRUCTURAL STUDIES

XRD θ-2θ patterns of the decomposed 400 °C -500 °C CeO_2 and 400 °C -800 °C CeO_2 films are shown in Figure 7.5. Four diffraction peaks ascribed to (111), (200), (220) and (311) reflections, which are prominent diffraction peaks indexed to the cubic fluorite CeO_2 structure (PDF No. 00-034-0394), are detected in all decomposed CeO_2 samples. Figure 7.5a shows a predominant orientation peak along the [111] direction. The presence of the diffraction peaks indicates the crystalline nature of the CeO_2 films. However, in Figure

7.5b, the (200) peak displays the highest intensity at 2θ = 33°. Although CeO_2 has a (200) peak at this angle, the intensity of that peak is usually 25% of the CeO_2(111) peak and it may be the case that the Si(100) kinematically forbidden peak described by Hwang [213] also contributes to the intensity of this peak (and this forbidden peak intensity varies with the diffractometer phi angle, which is uncontrolled and varies from scan to scan). This is confirmed by rotating the samples which resulted in different XRD intensities for the (200) peak in particular. Further evidence for the presence of two components is seen in the asymmetric line shape seen in Figure 7.5b. For this reason the full width at half maximum (FWHM) of the CeO_2 (111) peak is used as an indicator of the crystallinity quality of the CeO_2 deposits. Using Gaussian fitting, the FWHM is calculated for the two samples. As expected, lower CeO_2 (111) peak FWHM values are obtained for CeO_2 films annealed at higher temperatures (400 °C -800°C).

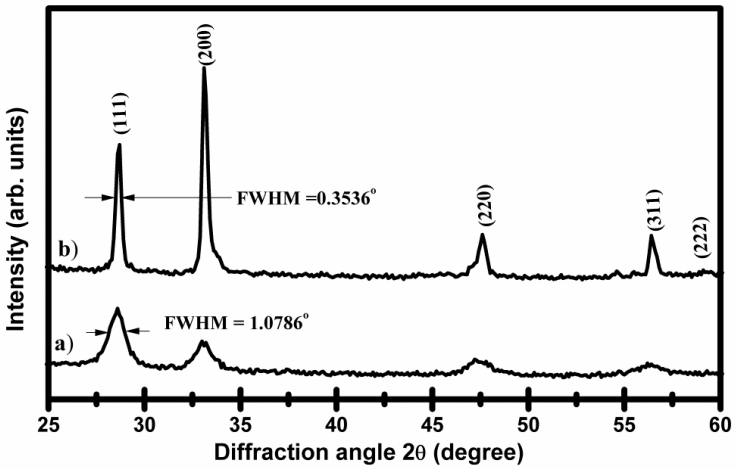

Figure 7.5: XRD θ-2θ patterns of decomposed CeO_2 film deposited by a spin coater and annealed at a) 400 °C- 500 °C and b) 400 °C -800 °C for 30 minutes at each temperature.

7.5.2 COMPOSITION ANALYSIS

EDX analysis of the wet chemical deposited 400 °C -500 °C CeO_2 film was performed to determine the elemental composition of the film. It can be clearly seen from the EDX spectrum of the decomposed CeO_2 film, in Figure 7.6, shows that the only constituents detected are Si, Ce and O. The Si is from the substrate, and the atomic percentage ratios of the various elements are shown in Table 7.3. However, the fact that there is a SiO_2 layer, as previously mentioned in Chapter 5, makes accurate calculation of the CeO_2 composition/stoichiometry difficult with the present data.

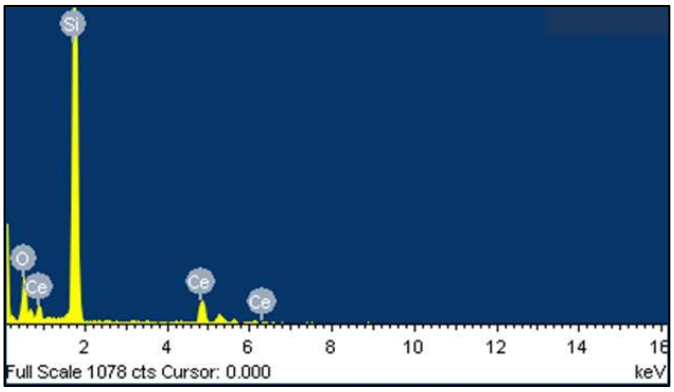

Figure 7.6: EDX spectrum for the 400 °C -500 °C CeO_2 film.

Table 7.3: EDX atomic percentage ratios of the various elements on the 400 °C -500 °C CeO_2 film.

Element	Weight (%)	Atomic (%)
Si	42.74	51.31
Ce	38.56	9.28
O	18.71	39.42

The surface chemical compositions of the films are further studied by XPS in order to probe the presence of Ce^{4+} and Ce^{3+} oxidation states. Figure 7.7 displays the Ce3d core level spectra of the 400 °C-500 °C CeO_2 and 400 °C-800 °C CeO_2 films. The 400 °C-500 °C CeO_2 film shows a mixed Ce^{3+}/Ce^{4+} charge state, while 400 °C-800 °C CeO_2 film shows a dominant Ce^{4+} charge

state. The established binding energy positions of the Ce^{3+} and Ce^{4+} oxidation states are indicated by the vertical dotted lines. It is important to note that although the presence of the Ce^{3+} and Ce^{4+} could easily be identified in the Ce 3d spectra of both samples, the relative concentrations could not be determined due to the complexity of the peak shape and the difficulty in the fitting the peak, as discussed previously.

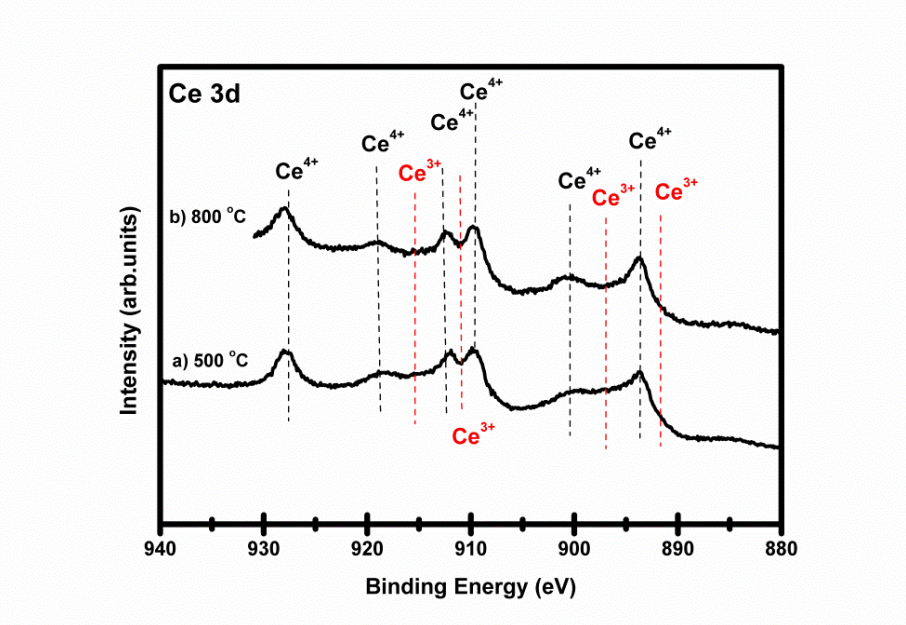

Figure 7.7: XPS Ce 3d core level spectra for spin coated a) 400 °C-500 °C CeO_2 and b) 400 °C-800 °C CeO_2 films.

Figure 7.8 shows the corresponding O 1s XPS data for the 400 °C-500 °C CeO_2 and 400 °C-800 °C CeO_2 samples. The binding energy positions of the various Ce oxidation states in the O 1s core level spectra are almost identical and overlap considerably, mainly due to the O^{2-} nature of the oxygen atom in both Ce_2O_3 and CeO_2. These two contributions give rise to the feature labelled (i) in Figure 7.8 and consequently, it is very difficult to deconvolve the O 1s peak into Ce_2O_3 and CeO_2 components. This is because it is well established that the very top layer of a CeO_2 system is usually rich in Ce^{3+} cations [8-9].

The presence of C-O contamination on the surface has previously been discussed, in Chapter 3 and 4, as a possible explanations for the feature labelled (ii) in Figure 7.8, at a binding energy ~ 1.8 eV higher than that of the Ce^{4+} oxidation state in the O 1s spectrum. But this energy shift value is slightly higher 1.8 eV in Figure 7.8, with ~ 2.1 eV and ~ 2.6 eV for the 400 °C-500 °C CeO_2 and 400 °C-800 °C CeO_2 samples, respectively. This is likely related to the presence of carbonate species that could be desorbed during the decomposition and/or the formation of O-C or O-Ce-C related components from the PVA present in the chemical solution used to decompose the CeO_2 films used in this experiment. However, regardless of the annealing temperatures, the samples displayed evidence of Ce in the Ce^{4+} oxidation state only, with a smaller percentage of Ce in the Ce^{3+} oxidation state in the 400 °C-500 °C CeO_2 sample, and a higher percentage of the contaminant/carbonate species (ii) in the 400 °C-800 °C CeO_2 sample. It is important to note that the samples are only annealed at the stated temperatures in air atmosphere; no further annealing is carried-out in UHV prior to the XPS experiment.

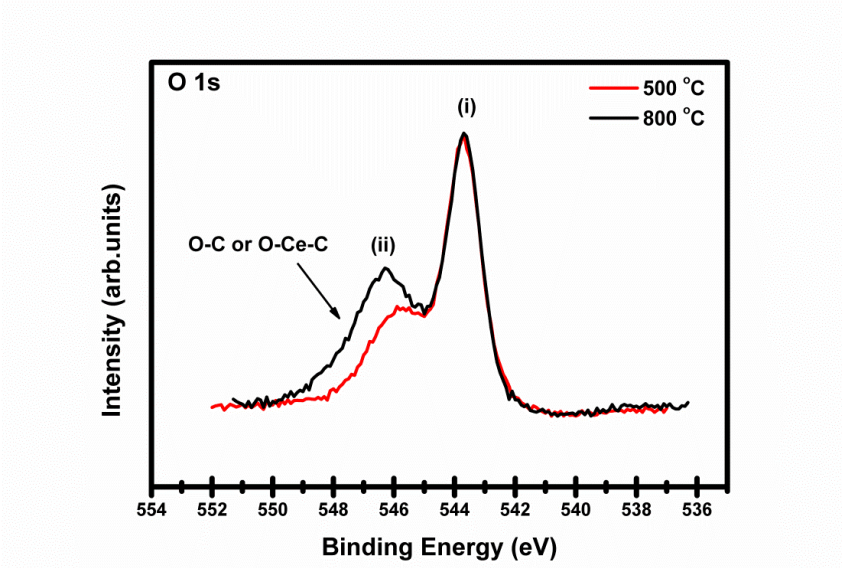

Figure 7.8: O 1s XPS spectra of spin coated 400 °C-500 °C and 400 °C-800 °C CeO_2.

7.5.3 OPTICAL PROPERTIES

The optical properties of the spin coated 400 °C-500 °C and 400 °C-800 °C CeO_2 films are investigated by UV-Vis absorption spectroscopy. The decomposition temperatures used to fully decompose the cerium nitrate and PVA solution into CeO_2 films lead to no significant difference in the absorption property as shown in Figure 7.7. The absorption of the 400 °C-500 °C CeO_2 film displayed slightly higher absorbance intensity, both in UV and visible regions, compared to the 400 °C-800 °C CeO_2 film.

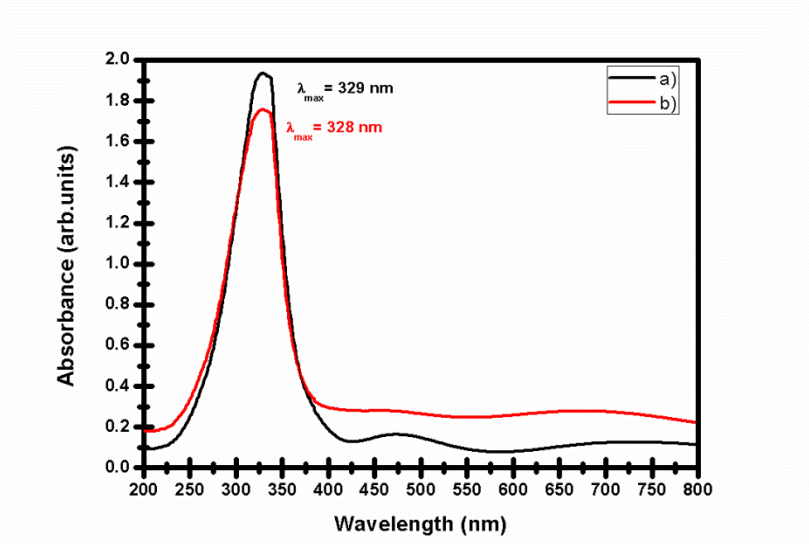

Figure 7.9: Room temperature UV-Vis absorption spectra of CeO_2 film deposited by a spin coater on quartz substrates a) 400 °C-500 °C and b) 400 °C-800 °C.

The bandgap energies of the CeO_2 films are estimated by extrapolating the absorption coefficient (α) from the absorbance data using a Tauc plot as shown in Figure 7.10. Figure 7.10 clearly shows that the extracted bandgap values of the two decomposed CeO_2 films are 3.38 eV and 3.46 eV for the 400 °C-500 °C and 400 °C-800 °C CeO_2 samples, respectively. Comparing the estimated bandgap energies to literature, the values are slightly larger than those of bulk CeO_2 powders (3.19 eV for direct transition and 3.01 eV for indirect transition) [214]. However, these values are similar to the bandgap

energy values recorded for the sputtered CeO_2 annealed samples, as highlighted in Chapter 4. Those values were 3.32 eV and 3.48 eV for the sputtered samples annealed at 500 °C and 800 °C, respectively.

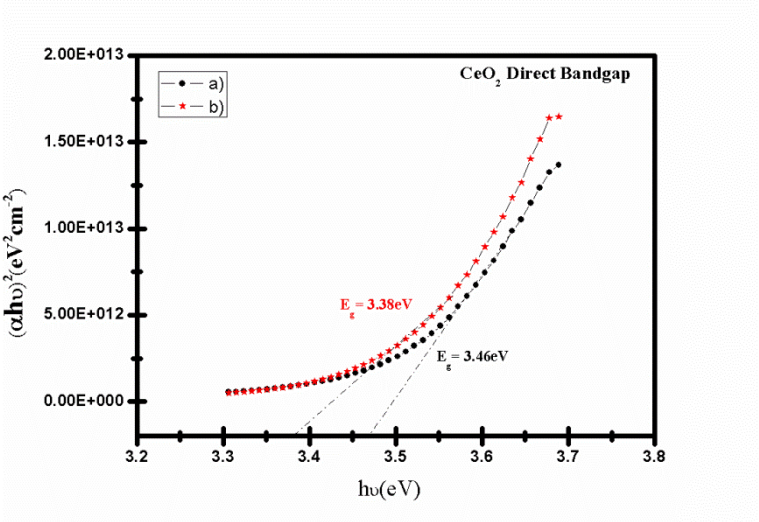

Figure 7.10: Tauc plot of $(\alpha hv)^2$ vs. hv for the CeO_2 films deposited by a spin coater on quartz substrates a) 400 °C-500 °C sample and b) 400 °C-800 °C sample.

7.5.4 NANOSHELL ENGINERING

As mentioned earlier in the chapter, the chemical bath method using $Ce(NO_3)_3.6H_2O$/PVA solution was adopted and extensively investigated, mainly to try develop and achieve spherical CeO_2 nanoshell structures, after the unsuccessful attempts using the PDCMS technique (described in Chapter 5). Multiple (ultimately unsuccessful) trails were attempted to engineer CeO_2 spherical nanoshell structures.

For example, the binder (PVA) quantity was reduced to 0.15 g, 0.1 g and 0.05 g from the initial value of 0.2 g, and the new chemical solutions were annealed either at 400 °C for 30 minutes or at lower temperatures (350 °C, 300 °C, 250 °C, 200 °C, 150 °C, 100 °C and 50 °C) for longer periods of time to fully decompose the cerium salt. This was followed by a 30 minute thermal anneal at a temperature of 500 °C to fully eliminate both the PVA and the PS nanospheres and yield pure CeO_2 nanostructures. The final

results of the CeO_2 deposits obtained were investigated using SEM. Figure 7.11 presents plan and 60° views SEM images of the 400 °C-500 °C CeO_2 nanostructures (where, as before, in our naming convention the first temperature refers to the anneal used to decompose the cerium salt and, in this case, the second to the anneal used to eliminate both the PVA and the PS nanospheres), from a cerium salt containing 0.2 g PVA.

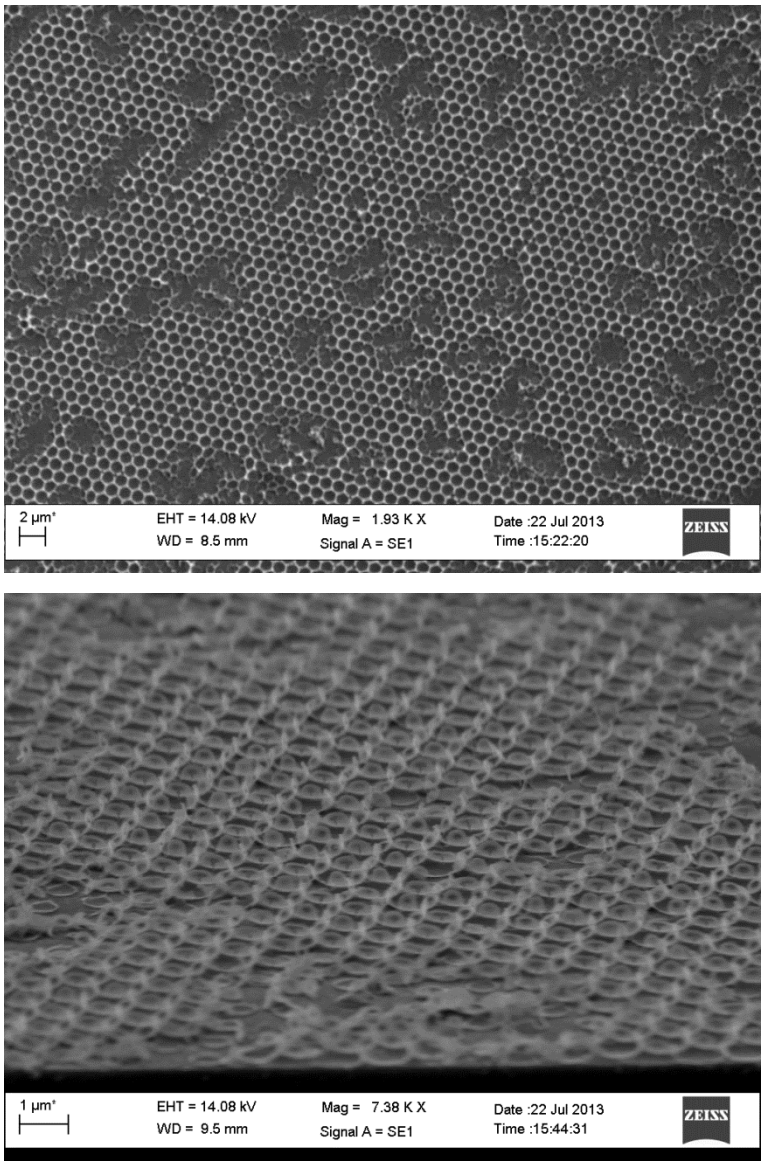

Figure 7.11: SEM images (top and 60° views) of the 400 °C-500 °C CeO_2 nanostructures after the decomposition of the residual cerium salt into CeO_2 and the removal of the PVA binder (0.2 g) and PS nanospheres.

The SEM images for all other samples with a reduced binder quantity and those first annealed at lower temperatures displayed similar results to that in Figure 7.11. As can be clearly seen in Figure 7.11, these attempts at generation of the spherical nanoshell structures failed.

Furthermore, a literature review of other cerium salts, with lower decomposition temperatures was conducted. However, the decomposition temperatures for all cerium salts were higher than the glass transition and melting temperature of the polystyrene nanosphere. Therefore, no further trials using different cerium salt solutions were attempted.

7.6 CONCLUSIONS

In this chapter, a simple low cost and high throughput wet chemical process is successfully used to fabricate a uniform 40 ± 5 nm thick nanocrystalline CeO_2 thin film post-decomposition of the cerium salt. Structural studies using XRD confirmed the crystalline nature of the decomposed CeO_2 films. The crystallinity of the films increased as a result of increasing the annealing temperature. EDX is used to identify the chemical constituents of the decomposed CeO_2 films. Only Ce, O and Si elements are detected, which indicates a full decomposition of the cerium salt and PVA into nanocrystalline CeO_2 film was achieved by annealing. XPS data showed Ce mainly in the Ce^{4+} oxidation state on both samples, 400 °C-500 °C CeO_2 and 400 °C-800 °C CeO_2,with a smaller percentage of the Ce in the Ce^{3+} oxidation state in the 400 °C-800 °C CeO_2 sample. It also displayed a higher percentage of contaminant/carbonate species on the 400 °C-800 °C CeO_2 sample. The optical properties of the spin coated decomposed CeO_2 films were examined and no significant differences are seen for the samples as a result of the different decomposition temperatures. Although a pure uniform CeO_2 film was successfully achieved using this method, increasing the surface to

volume ratio through the development of spherical nanoshells remains a challenge. Therefore, PDCMS technique is presently considered more feasible than this wet chemical technique for the case of pure CeO_2 materials.

Chapter 8

CONCLUSIONS AND FUTURE WORK

8.1 CONCLUSIONS

Among the entire metal-oxide material candidates which show numerous functional properties suitable for efficient H_2 production in a H_2O- splitting two-step thermochemical cycle, this thesis focused on the redox active metal-oxide CeO_2. This material has emerged as a promising candidate for energy related applications but more specifically in two-step thermochemical cycling processes. This is mainly due to its rapid fuel production kinetics and high selectivity resulting mainly from its unique properties and specifically its highly efficient O_2 storage capacity. The ability to combine these unique material properties with a novel light management structural geometry, based on the creation of low quality-factor whispering gallery resonant modes inside spherical nanoshell structures, is crucial for the future applications in the solar fuel-cell industry. Engineering the spherical geometry of the metal-oxide (as described in Chapter 6) is a matter of great interest because, as mentioned previously, the spherical geometry enhances the light absorption, while the metal-oxide nanomorphology will provide

higher redox activities as a result of the larger surface area (spherical geometry), which will lead to an efficient thermochemical process and improved H_2 production.

The successful development and characterisation of the CeO_2 nanostructured thin films, by PDCMS of the CeO_2 target is described in Chapter 3 of the thesis. The influences of two sputtering gas ambients on the structural and morphological properties are studied using XRD and AFM measurements, respectively. It is observed that there is no structural effect on the as-deposited CeO_2 in an inert gas (Ar) sputtering ambient. An improvement in the crystallinity of the as-deposited CeO_2 is observed when O_2 gas is introduced in the sputtering chamber. The film compositions are studied using XPS and SIMS. The results indicated a transformation of the Ce from the Ce^{4+} state to the Ce^{3+} state, indicative of a chemically reduced state of CeO_2 due to the formation of oxygen vacancies. TGA and electrochemical CV on both sputtered samples showed higher oxygen storage capacity for films deposited in an inert gas (Ar) compared to films deposited in the presence of O_2. The CV results specifically exhibited a linear variation with scan rate of the anodic peak currents for both films. The double layer capacitance values for films deposited in Ar and Ar/O_2 mixed atmospheres are found to be $(4.3 \pm 0.5) \times 10^{-4}$ F and $(1.6 \pm 0.2) \times 10^{-4}$ F, respectively. TGA results on the films confirmed that Ar sputtered samples have a tendency to greater oxygen losses upon reduction, compared to the films sputtered in an Ar/O_2 mixed atmosphere. This key outcome demonstrates that the oxygen storage capacity of the sputtered CeO_2 films can be controlled and enhanced by varying the gas atmosphere during the deposition process.

As mentioned in Chapter 1, in a metal-oxide two-step thermochemical cycle, the first step occurs as a result of an endothermic reaction where a high temperature is required to start the reaction. Therefore, since CeO_2 sputtered in an Ar ambient displays higher oxygen storage capacity, it is extremely

worthwhile to investigate the effect of post-deposition annealing temperature and atmosphere on the properties of these thin CeO_2 films, including crystalline structure, grain size and shape and optical properties. The results obtained from XRD showed that prepared films crystallised predominantly in the CeO_2 cubic fluorite structure, although evidence of hexagonal Ce_2O_3 is also seen, as a result of post-deposition annealing. These results are described in Chapter 4. The thermal anneal temperature and the oxygen content of the Ar/O_2 annealing atmosphere played important roles on the size and shape of the nanocrystals, as determined by AFM. The average grain size as well as the out of plane coherence length varied with varying OFR in the annealing chamber. Additionally, the shape of the grains seen in the AFM studies transformed from circular to triangular as a result of increasing the OFR from 20 sccm to 30 sccm during an 800 °C thermal anneal. Furthermore, a bandgap energy value of 3.04 eV is estimated from the UV absorption for the as-deposited CeO_2 and this value increased with increasing annealing temperature. An emission at 3.36 eV associated with nanocrystalline CeO_2 is also observed in low-temperature PL.

The engineering and development of high surface to volume ratio CeO_2 structures using a PS nanosphere template is described in Chapter 5. This was studied due to the importance of high surface area for an efficient H_2 production in the two-step thermochemical cycle. Firstly, the nanosphere colloidal monolayer deposition was generated by a self-assembly method on the surface of DI water. This is used as a starting template to create CeO_2 spherical nanoshell structures using PDCMS However, due to both the shape of the nanospheres and the fact that the sputtering process is line of sight, the sputtered CeO_2 deposit can only reach exposed surfaces and as a consequence, domed shaped structures are realised. Nevertheless, the optical properties of the domed-shaped structures are studied using UV-Vis absorption spectroscopy. The results showed an increase in UV and light

absorption as a result of the domed-shape nanostructure compared to thin CeO_2 films.

The development of hollow spherical nanoshells of metal-oxides with a low decomposition temperature, as an alternative structure to the conventional porous structures used in present two-step thermochemical processes, is described in Chapter 6. This is a novel aspect of this thesis work since the spherical geometry of the metal-oxide is believed to enhance light absorption through the creation of whispering gallery resonant modes within the spherical nanostructures and thus enable a more efficient solarthermal-driven process (see Chapter 1). The generation of ZnO and CeO_2 coated ZnO films and nanoshells are demonstrated in Chapter 6. The ZnO nanostructures are grown by a facile drop coating method using zinc acetate in anhydrous ethanol solution and the CeO_2 nanostructures are produced by a PDCMS method. XRD, SEM and SIMS measurements confirmed the structural, morphological and compositional properties of the deposited materials. UV and visible light absorption is quite significantly enhanced through the engineering of spherical nanoshells on a PS monolayer template, most likely due to the whispering gallery modes in such nanoshell cavities, as well as the addition of the CeO_2 layer. These results are significantly important in terms of enabling future materials and device developments, with the aim of controlling key film parameters for technologically important applications, specifically in the areas of solar-thermal fuel generation and catalysis, where the combination of the nanostructure engineering possible with ZnO materials and the oxygen storage and variable stoichiometry properties of CeO_2 provides a unique set of advantageous material properties.

A wet chemical process is successfully used to fabricate nanocrystalline CeO_2 thin films from cerium nitrate as a starting material, as described in Chapter 7. Two final decomposition temperatures of 500 °C and 800 °C are used to fully decompose the cerium nitrate into CeO_2 films. The

film properties at both final temperatures are investigated. The structural properties, studied using XRD, revealed diffraction peaks associated with the cubic fluorite CeO_2 structure only. The compositions of the films are examined using both EDX and XPS. The EDX results showed the existence of the elements Si, Ce and O on both samples. XPS Ce 3d data for the samples consisted mainly of Ce in the Ce^{4+} oxidation state and no significant differences are detected between the samples further annealed at 500 °C and 800 °C. The optical absorption of the samples shows no significant difference between the two samples, annealed at 500 °C and 800°C, respectively.

8.2 FUTURE WORK

After the successful deposition of CeO_2 thin films by both PDCMS and wet chemical spin coating techniques, useful and important future work could obviously include the fabrication of CeO_2 spherical nanoshell structures by adopting other methods. This work is now in progress. Although the ZnO nanoshell and CeO_2-coated ZnO nanoshell structures show improved optical properties compared to thin films, directly engineering CeO_2 spherical nanoshells will enhance the UV and light absorption further, providing for a better performance of solar fuel-cell and two-step thermochemical cycle processes, especially with its high ultraviolet absorbance which also enables other applications such as UV protection coatings. This can be executed through the use of SiO_2 nanosphere monolayers as a template; however, more knowledge on the fabrication and etching of the nanospheres is essential as simple gasification techniques will not work.

Alternative deposition methods can be investigated since many recent reports have successfully fabricated spherical shells of ceria, cerium and ceria-based materials for photocatalytic activities. For example, Zhang, L. et. al. [215] prepared hollow shells of CeO_2 with TiO_2 photocatalysts by a

precipitation-co-hydrothermal method. Deng, W. et. al. [216] synthesized monodisperse ceria hollow spheres via a sol-gel method, where the spheres were successfully fabricated by calcination. Other chemical techniques were successfully used to fabricate ceria spheres including cerium nitrate on silica cores [217], potentiostatic electrodeposition of CeO_2 on PS sphere templates [218], and; a one-step hydrothermal method [219]. All these different deposition techniques could be adapted to successfully fabricate CeO_2 spherical shell structures.

Further work could also include the study of oxygen storage properties of the wet chemical deposited CeO_2 films using TGA and electrochemical CV. The effect of multiple spherical nanoshell structure layers (possessing higher surface areas and more whispering gallery structures) on the oxygen storage and optical absorption properties could also be explored. The effect of using different spherical diameters on the optical absorption could also be examined. As mentioned in Chapter 1, metal-oxide and metal doped CeO_2 have exhibited remarkably lower thermal reduction temperatures compared to undoped CeO_2, which is an important property in the two-step thermochemical cycle production. Therefore, engineering metal and metal-oxide doped CeO_2 spherical nanoshell structures is potentially an important element of the future work and a study of the oxygen storage properties of these doped CeO_2 structures and the thermal reduction temperature required could be investigated. Finally, a two-step thermochemical cycle unit can be built and tested for H_2 production using spherical nanoshell structures of CeO_2, ZnO, CeO_2 coated ZnO and metal and metal-oxide doped CeO_2 samples. These data can then be compared to the H_2 production rate from the available porous CeO_2 two-step thermochemical cycle.

Appendix

A.1 Chemical Analysis - XPS

XPS was also used to study and characterise the surface of the ZnO seed layer films used in Chapter 6. Figure A.1 shows the Zn 2p spectra of these ZnO seed layer films, with high intensity peaks located at 1044.50 eV and 1021.33 eV assigned to the Zn $2p_{1/2}$ and Zn 2 $p_{3/2}$, respectively.

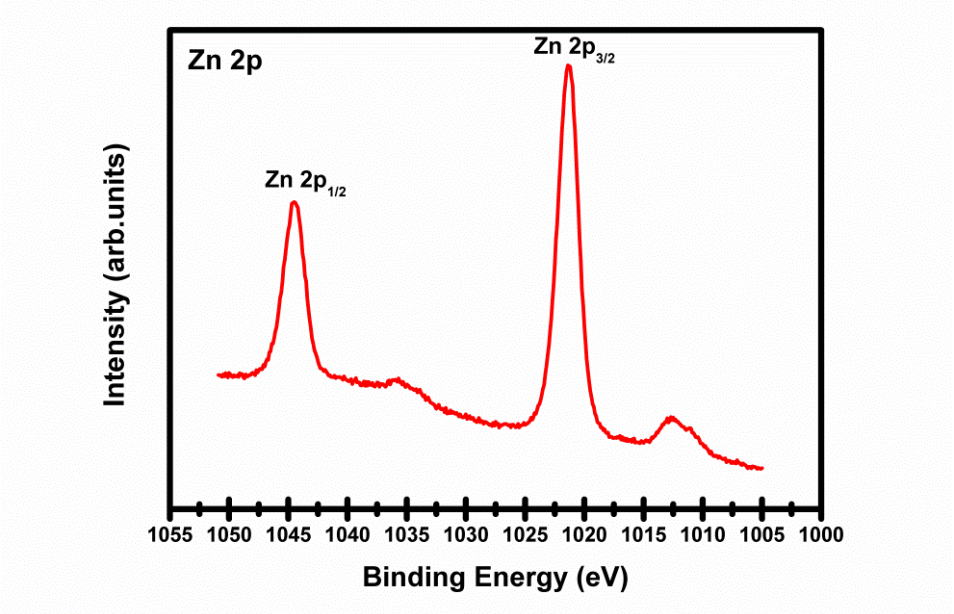

Figure A.1: XPS Zn 2p spectra of ZnO seed layer film deposited on Si (100) substrate using zinc acetate as a starting material.

In the survey scan (Figure A.2), only C, O and Zn elements are observed, thus demonstrating that no other contaminants are present in the ZnO seed layer specimens. Higher resolution scans of O and C are conducted. For O 1s spectrum (Figure A.3), two peaks at binding energies of 530.1 eV and 531.8 eV are observed. An oxygen peak at a binding energy of 531.8 eV is associated with C-O bonds originating from oxygen physically and chemically adsorbed on the surface. The oxygen peak at a binding energy of 530.1 eV corresponds to O-Zn bonds. The main Zn peak at binding energy of 1021.33 eV (Figure A.1) originates from Zn-O bonds. Figure A.4

shows the C 1s spectrum of the ZnO seed layer. There is a very weak peak at 299.1 eV, the binding energy of adventitious carbon, indicating a low contaminant level at the surface of these ZnO films.

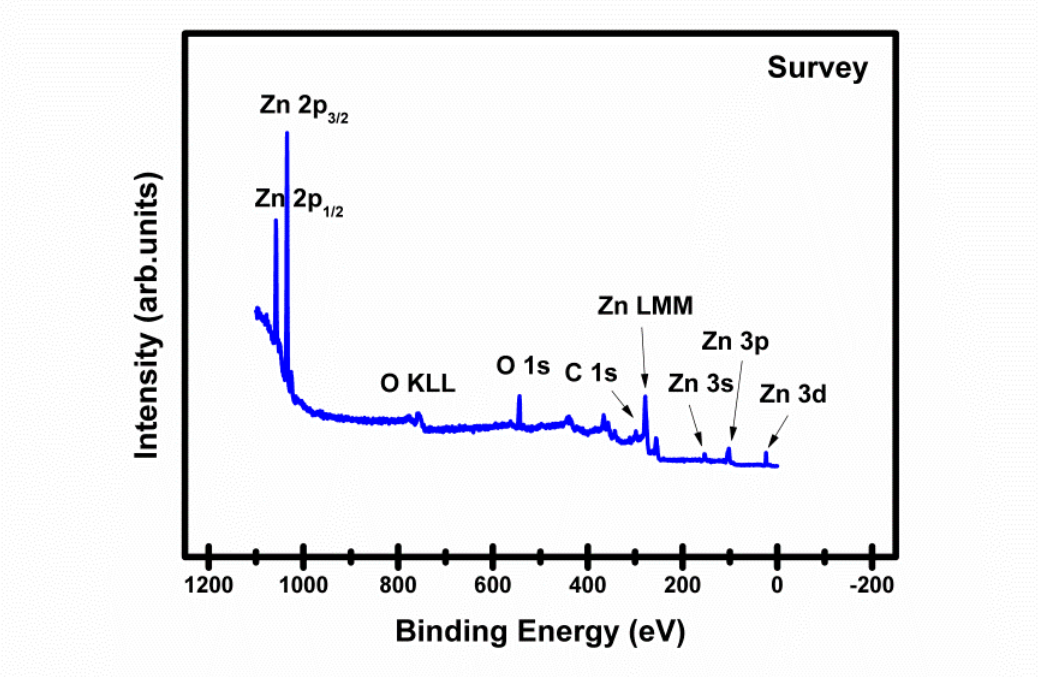

Figure A.2: XPS survey spectrum on ZnO seed layer film deposited on Si (100) substrate.

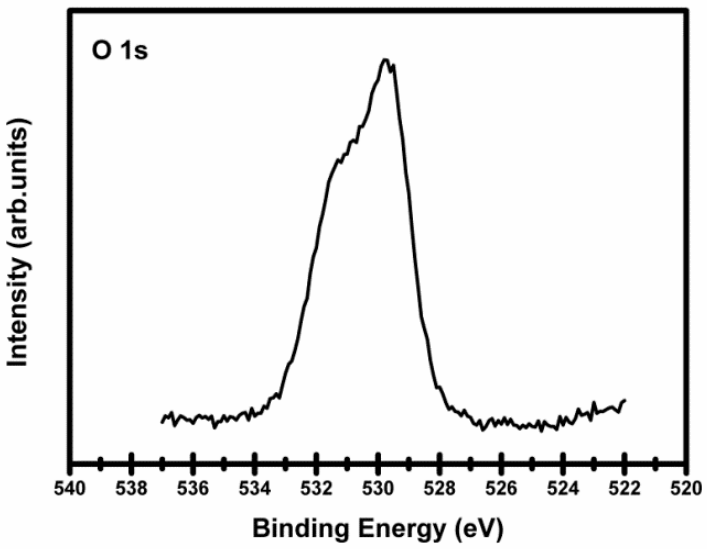

Figure A.3: O 1s XPS spectrum of ZnO seed layer film deposited on Si(100) substrate.

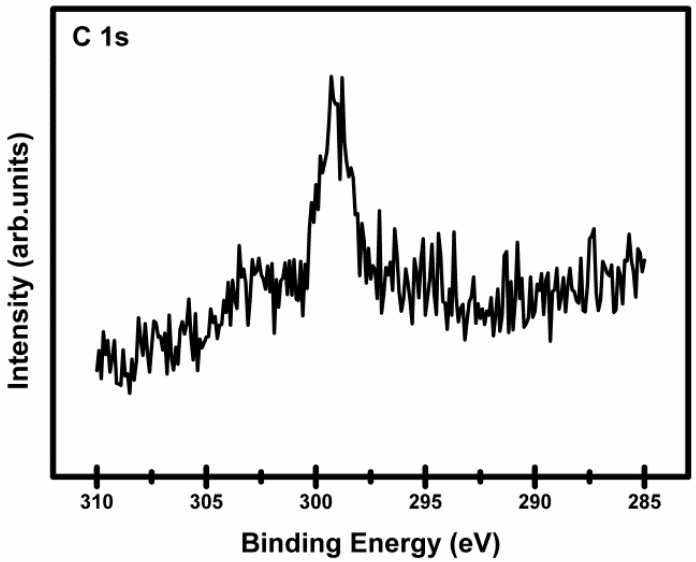

Figure A.4: C 1s XPS spectrum of ZnO seed layer film deposited on Si(100) substrate.

References

[1] D.E. Anderson (1975). U.S. Patent No. 3,924,604. Washington, DC: U.S. Patent and Trademark Office.

[2] W.C. Chueh, C. Falter, M. Abbott, D. Scipio, P. Furler, S.M. Haile, A. Steinfeld, Science, 330 (2010) 1797-1801.

[3] S. Abanades, P. Charvin, G. Flamant, P. Neveu, Energy, 31 (2006) 2805-2822.

[4] S. Abanades, G. Flamant, Solar Energy, 80 (2006) 1611-1623.

[5] S. Abanades, A. Legal, A. Cordier, G. Peraudeau, G. Flamant, A. Julbe, Journal of Materials Science, 45 (2010) 4163-4173.

[6] A. Le Gal, S. Abanades, International Journal of Hydrogen Energy, 36 (2011) 4739-4748.

[7] M. Howley, M. Holland and D. Dineen, Energy in Ireland 1990 - 2013, 2014 Report, Sustainable Energy Authority of Ireland (seai), 2014. Retreived from http://www.seai.ie/Publications

[8] K.E. Trenberth, J.T. Fasullo, J. Kiehl, Bulletin of the American Meteorological Society, 90 (2009) 311-323.

[9] J.R. Bolton, Science, 202 (1978) 705-711.

[10] M.A. Green, Solar Cells: Operating Principles, Technology, and SystemApplications (1982).

[11] I. Dincer, C. Zamfirescu, International Journal of Hydrogen Energy, 37 (2012) 16266-16286.

[12] K. Rajeshwar, R. McConnell, S. Licht, Toward a Renewable Energy Future. Springer: New York, (2008).

[13] M. Momirlan, T. Veziroğlu, Renewable and Sustainable Energy Reviews, 3 (1999) 219-231.

[14] A. Steinfeld, Solar Energy, 78 (2005) 603-615.

[15] E.A. Fletcher, R.L. Moen, Science, 197 (1977) 1050-1056.

[16] E. Bilgen, International Journal of Hydrogen Energy, 9 (1984) 53-58.

[17] L. Xiao, S.-Y. Wu, Y.-R. Li, Renewable Energy, 41 (2012) 1-12.

[18] D. Graf, N. Monnerie, M. Roeb, M. Schmitz, C. Sattler, International Journal of Hydrogen Energy, 33 (2008) 4511-4519.

[19] C. Perkins, A.W. Weimer, International Journal of Hydrogen Energy, 29 (2004) 1587-1599.

[20] T. Kodama, N. Gokon, Chemical Reviews, 107 (2007) 4048-4077.

[21] J.E. Funk, R.M. Reinstrom, Industrial & Engineering Chemistry Process Design and Development, 5 (1966) 336-342.

[22] J.E. Funk, International Journal of Hydrogen Energy, 26 (2001) 185-190.

[23] S. Yalcin, International Journal of Hydrogen Energy, 14 (1989) 551-561.

[24] G. Beghi, International Journal of Hydrogen Energy, 11 (1986) 761-771.

[25] T. Nakamura, Solar Energy, 19 (1977) 467-475.

[26] K. Ehrensberger, A. Frei, P. Kuhn, H. Oswald, P. Hug, Solid State Ionics, 78 (1995) 151-160.

[27] Y. Tamaura, A. Steinfeld, P. Kuhn, K. Ehrensberger, Energy, 20 (1995) 325-330.

[28] L. Vayssieres, On Solar Hydrogen and Nanotechnology, John Wiley & Sons, 2010.

[29] M. Lundberg, International Journal of Hydrogen Energy, 18 (1993) 369-376.

[30] L. Brown, N. Wong, R. Buckingham, R. Rennels, Y. Chen, in: 17th World Hydrogen Energy Conference, 2008.

[31] L. Schunk, W. Lipiński, A. Steinfeld, Chemical Engineering Journal, 150 (2009) 502-508.

[32] W.C. Chueh, A.H. McDaniel, M.E. Grass, Y. Hao, N. Jabeen, Z. Liu, S.M. Haile, K.F. McCarty, H. Bluhm, F. El Gabaly, Chemistry of Materials, 24 (2012) 1876-1882.

[33] M. Roeb, C. Sattler, R. Klüser, N. Monnerie, L. de Oliveira, A.G. Konstandopoulos, C. Agrafiotis, V. Zaspalis, L. Nalbandian, A. Steele, Journal of Solar Energy Engineering, 128 (2006) 125-133.

[34] P. Loutzenhiser, M. Gálvez, I. Hischier, A. Stamatiou, A. Frei, A. Steinfeld, Energy & Fuels, 23 (2009) 2832-2839.

[35] P. Furler, J. Scheffe, M. Gorbar, L. Moes, U. Vogt, A. Steinfeld, Energy & Fuels, 26 (2012) 7051-7059.

[36] J.R. Scheffe, A. Steinfeld, Energy & Fuels, 26 (2012) 1928-1936.

[37] G.A. Ozin, A.C. Arsenault, L. Cademartiri, Nanochemistry: a Chemical Approach to Nanomaterials, Royal Society of Chemistry, 2009.

[38] G. Cao, Synthesis, Properties and Applications, World Scientific, 2004.

[39] S. Mostafa, F. Behafarid, J.R. Croy, L.K. Ono, L. Li, J.C. Yang, A.I. Frenkel, B.R. Cuenya, Journal of the American Chemical Society, 132 (2010) 15714-15719.

[40] A. Tschope, W. Liu, M. Flytzanistephanopoulos, J.Y. Ying, Journal of Catalysis, 157 (1995) 42-50.

[41] K. Eguchi, T. Setoguchi, T. Inoue, H. Arai, Solid State Ionics, 52 (1992) 165-172.

[42] P. Jasinski, T. Suzuki, H.U. Anderson, Sensors and Actuators B: Chemical, 95 (2003) 73-77.

[43] A. Corma, P. Atienzar, H. Garcia, J.-Y. Chane-Ching, Nature Materials, 3 (2004) 394-397.

[44] B.M. Reddy, A. Khan, Catalysis Surveys from Asia, 9 (2005) 155-171.

[45] N. Skorodumova, R. Ahuja, S. Simak, I. Abrikosov, B. Johansson, B. Lundqvist, Physical Review B, 64 (2001) 115108.

[46] J. Kullgren, K. Hermansson, C. Castleton, The Journal of Chemical Physics, 137.4 (2012) 044705.

[47] T. Murota, T. Hasegawa, S. Aozasa, H. Matsui, M. Motoyama, Journal of Alloys and Compounds, 193 (1993) 298-299.

[48] S. Babu, R. Thanneeru, T. Inerbaev, R. Day, A.E. Masunov, A. Schulte, S. Seal, Nanotechnology, 20 (2009) 085713.

[49] C. Zhang, A. Michaelides, D.A. King, S.J. Jenkins, Physical Review B, 79 (2009) 075433.

[50] M. Mogensen, N.M. Sammes, G.A. Tompsett, Solid State Ionics, 129 (2000) 63-94.

[51] B.K. Cho, Journal of Catalysis, 131 (1991) 74-87.

[52] C.T. Campbell, C.H. Peden, Science, 309 (2005) 713-714.

[53] R. Panlener, R. Blumenthal, J. Garnier, Journal of Physics and Chemistry of Solids, 36 (1975) 1213-1222.

[54] Q.-L. Meng, C.-i. Lee, T. Ishihara, H. Kaneko, Y. Tamaura, International Journal of Hydrogen Energy, 36 (2011) 13435-13441.

[55] P. Singh, M. Hegde, Chemistry of Materials, 22 (2009) 762-768.

[56] H. Kaneko, T. Miura, H. Ishihara, S. Taku, T. Yokoyama, H. Nakajima, Y. Tamaura, Energy, 32 (2007) 656-663.

[57] S. Huang, L. Li, J. Vleugels, P. Wang, O. Van der Biest, Journal of the European Ceramic Society, 23 (2003) 99-106.

[58] S. Haussener, A. Steinfeld, Materials, 5 (2012) 192-209.

[59] Y. Yao, J. Yao, V.K. Narasimhan, Z. Ruan, C. Xie, S. Fan, Y. Cui, Nature Communications, 3 (2012) 664.

[60] A. Savchenkov, V. Ilchenko, L. Maleki, T.A. Handley, (2006). U.S. PAtent No. 6,987,914. Washington, DC: U.S. Patent and Trademark Office.

[61] W. Liang, V. Ilchenko, A. Savchenkov, A. Matsko, D. Seidel, L. Maleki, Optics letters, 35 (2010) 2822-2824.

[62] G.C. Righini, S. Soria, Sensors, 16 (2016) 905.

[63] P. Furler, J. Scheffe, D. Marxer, M. Gorbar, A. Bonk, U. Vogt, A. Steinfeld, Physical Chemistry Chemical Physics, 16 (2014) 10503-10511.

[64] P. Kelly, R. Arnell, Vacuum, 56 (2000) 159-172.

[65] D.B. Hall, P. Underhill, J.M. Torkelson, Polymer Engineering and Science, 38 (1998) 2039-2045.

[66] W. Somkhunthot, T. Burinprakhon, I. Thomas, T. Seetawan, V. Amornkitbamrung, Elektrika J Elec Eng, 9 (2007) 20-26.

[67] S. Swann, Physics in Technology, 19 (1988) 67.

[68] R.A. Powell, S.M. Rossnagel, PVD for Microelectronics: Sputter Deposition Applied to Semiconductor Manufacturing, Elsevier, 1999.

[69] S. de Souza, S.J. Visco, L.C. De Jonghe, Solid State Ionics, 98 (1997) 57-61.

[70] Y. Xiang, W. Chengbiao, L. Yang, Y. Deyang, X. Tingyan, Plasma Science and Technology, 8 (2006) 337.

[71] T. Moiseev, D.C. Cameron, Surface and Coatings Technology, 200 (2006) 5306-5317.

[72] P. Kelly, J. Hisek, Y. Zhou, R. Pilkington, R. Arnell, Surface Engineering, 20 (2004) 157-162.

[73] A. Belkind, Z. Zhao, D. Carter, L. Mahoney, G. McDonough, G. Roche, R. Scholl, H. Walde, in: Proceedings of the Annual Technical Conference-Society of Vacuum Coaters, 2000, pp. 86-90.

[74] R.K. Vijayaraghavan, Investigation of Doped Cuprous Halides for Photovoltaic and Display Applications, Dublin City University, 2011. Retrieved from http://doras.dcu.ie/16694/

[75] G. Binnig, C.F. Quate, C. Gerber, Physical Review Letters, 56 (1986) 930.

[76] D. Byrne, The Growth and Characterisation of Ordered Arrays of Zinc Oxide Nanostructures and Optical Studies of Defects in Zinc Oxide, Dublin City University, 2012. Retrieved from http://doras.dcu.ie/16919/

[77] A. Urquhart, M. Alexander, Tissue Engineering Using Ceramics and Polymers, (2007) 175.

[78] S. Tanuma, T. Shiratori, T. Kimura, K. Goto, S. Ichimura, C. Powell, Surface and Interface Analysis, 37 (2005) 833-845.

[79] P.T. Kissinger, W.R. Heineman, Journal of Chemical Education, 60 (1983) 702.

[80] D. Macdonald, Transient Techniques in Electrochemistry, Springer Science & Business Media, 2012.

[81] A.J. Bard, L.R. Faulkner, Electrochemical Methods: Fundamentals and Applications, Wiley New York, 1980.

[82] M. Roeb, M. Neises, N. Monnerie, F. Call, H. Simon, C. Sattler, M. Schmücker, R. Pitz-Paal, Materials, 5 (2012) 2015-2054.

[83] C. Descorme, R. Taha, N. Mouaddib-Moral, D. Duprez, Applied Catalysis A: General, 223 (2002) 287-299.

[84] B. Zhang, X. Tang, Y. Li, Y. Xu, W. Shen, International Journal of Hydrogen Energy, 32 (2007) 2367-2373.

[85] N. Özer, Solar Energy Materials and Solar Cells, 68 (2001) 391-400.

[86] J. Owens, E. Tarte, P. Berghuis, R. Somekh, IEEE Transactions on Applied Superconductivity, , 5 (1995) 1657-1660.

[87] N. Savvides, A. Thorley, S. Gnanarajan, A. Katsaros, Thin Solid Films, 388 (2001) 177-182.

[88] H. Yahiro, Y. Eguchi, K. Eguchi, H. Arai, Journal of Applied Electrochemistry, 18 (1988) 527-531.

[89] L. Wu, H. Wiesmann, A. Moodenbaugh, R. Klie, Y. Zhu, D. Welch, M. Suenaga, Physical Review B, 69 (2004) 125415.

[90] E. Rossinyol, J. Arbiol, F. Peiró, A. Cornet, J. Morante, B. Tian, T. Bo, D. Zhao, Sensors and Actuators B: Chemical, 109 (2005) 57-63.

[91] M.-T. Ta, D. Briand, Y. Guhel, J. Bernard, J. Pesant, B. Boudart, Thin Solid Films, 517 (2008) 450-452.

[92] R.P. Netterfield, W.G. Sainty, P.J. Martin, S.H. Sie, Applied Optics, 24 (1985) 2267-2272.

[93] G. Atanassov, R. Thielsch, D. Popov, Thin Solid Films, 223 (1993) 288-292.

[94] T. Ami, M. Suzuki, Materials Science and Engineering: B, 54 (1998) 84-91.
[95] D. Norton, J. Budai, M. Chisholm, Applied Physics Letters, 76 (2000) 1677-1679.
[96] A. Morshed, M. Moussa, S. Bedair, R. Leonard, S. Liu, N. El-Masry, Applied Physics Letters, 70 (1997) 1647-1649.
[97] T. Brezesinski, J. Wang, R. Senter, K. Brezesinski, B. Dunn, S.H. Tolbert, ACS Nano, 4 (2010) 967-977.
[98] S.G. Rudisill, L.J. Venstrom, N.D. Petkovich, T. Quan, N. Hein, D.B. Boman, J.H. Davidson, A. Stein, The Journal of Physical Chemistry C, 117 (2013) 1692-1700.
[99] P. Periyat, F. Laffir, S. Tofail, E. Magner, RSC Advances, 1 (2011) 1794-1798.
[100] M. Anwar, S. Kumar, F. Ahmed, N. Arshi, Y.J. Seo, C.G. Lee, B.H. Koo, Current Applied Physics, 11 (2011) S301-S304.
[101] H. Nagata, T. Tsukahara, S. Gonda, M. Yoshimoto, H. Koinuma, Japanese Journal of Applied Physics, 30 (1991) L1136.
[102] J. Jones, E. Croke, C. Garland, O. Marsh, T. McGill, Journal of Vacuum Science & Technology B, 16 (1998) 2686-2689.
[103] D. Huang, F. Qin, Z. Yao, Z. Ren, L. Lin, W. Gao, Q. Ren, Applied Physics Letters, 67 (1995) 3724-3725.
[104] Y.M. Chiang, E. Lavik, I. Kosacki, H. Tuller, J. Ying, Applied Physics Letters, 69 (1996) 185-187.
[105] T. Chikyow, S. Bedair, L. Tye, N. El-Masry, Applied Physics Letters, 65 (1994) 1030-1032.
[106] A. Eltayeb, R.K. Vijayaraghavan, A. McCoy, A. Venkatanarayanan, A.A. Yaremchenko, R. Surendran, E. McGlynn, S. Daniels, Journal of Power Sources, 279 (2015) 94-99.
[107] K. Sundaram, P. Wahid, O. Melendez, Journal of Vacuum Science & Technology A, 15 (1997) 52-56.

[108] D. Mullins, S. Overbury, D. Huntley, Surface Science, 409 (1998) 307-319.

[109] M.Y.M. Abdelrahim, S.R. Benjamin, L.M. Cubillana-Aguilera, I. Naranjo-Rodríguez, J.L. de Cisneros, J.J. Delgado, J.M. Palacios-Santander, Sensors, 13 (2013) 4979-5007.

[110] Q. He, S. Mukerjee, B. Shyam, D. Ramaker, S. Parres-Esclapez, M. Illán-Gómez, A. Bueno-López, Journal of Power Sources, 193 (2009) 408-415.

[111] D. Wang, Y. Kang, V. Doan-Nguyen, J. Chen, R. Küngas, N.L. Wieder, K. Bakhmutsky, R.J. Gorte, C.B. Murray, Angewandte Chemie International Edition, 50 (2011) 4378-4381.

[112] L. Garvie, P. Buseck, Journal of Physics and Chemistry of Solids, 60 (1999) 1943-1947.

[113] H. Borchert, Y.V. Frolova, V.V. Kaichev, I.P. Prosvirin, G.M. Alikina, A.I. Lukashevich, V.I. Zaikovskii, E.M. Moroz, S.N. Trukhan, V.P. Ivanov, The Journal of Physical Chemistry B, 109 (2005) 5728-5738.

[114] I.-W. Park, J. Lin, J.J. Moore, M. Khafizov, D. Hurley, M.V. Manuel, T. Allen, Surface and Coatings Technology, 217 (2013) 34-38.

[115] G. Balakrishnan, C. Raghavan, C. Ghosh, R. Divakar, E. Mohandas, J.I. Song, S. Bae, T.G. Kim, Ceramics International, 39 (2013) 8327-8333.

[116] B. Elidrissi, M. Addou, M. Regragui, C. Monty, A. Bougrine, A. Kachouane, Thin Solid Films, 379 (2000) 23-27.

[117] I. Porqueras, C. Person, C. Corbella, M. Vives, A. Pinyol, E. Bertran, Solid State Ionics, 165 (2003) 131-137.

[118] M. Suchea, S. Christoulakis, K. Moschovis, N. Katsarakis, G. Kiriakidis, Thin Solid Films, 515 (2006) 551-554.

[119] L. Damiani, R. Mansano, in: Journal of Physics: Conference Series, IOP Publishing, 2012, pp. 012019.

[120] K. Mašek, M. Václavů, P. Bábor, V. Matolín, Applied Surface Science, 255 (2009) 6656-6660.

[121] A. Migani, K.M. Neyman, F. Illas, S.T. Bromley, The Journal of Chemical Physics, 131 (2009) 064701.

[122] P. Burroughs, A. Hamnett, A.F. Orchard, G. Thornton, Journal of the Chemical Society, Dalton Transactions, (1976) 1686-1698.

[123] Z. Wang, Z. Li, J. Feng, S. Yan, W. Luo, J. Liu, T. Yu, Z. Zou, Physical Chemistry Chemical Physics, 16 (2014) 8521-8528.

[124] Q. Zhu, C. Xie, H. Li, Q. Yang, Journal of Alloys and Compounds, 585 (2014) 267-276.

[125] N. Van Duy, S. Jung, N.T. Nga, D.N. Son, J. Cho, S. Lee, W. Lee, J. Yi, Materials Science and Engineering: B, 175 (2010) 176-180.

[126] M. Salari, S.H. Aboutalebi, A.T. Chidembo, I.P. Nevirkovets, K. Konstantinov, H.K. Liu, Physical Chemistry Chemical Physics, 14 (2012) 4770-4779.

[127] T. Suzuki, I. Kosacki, H.U. Anderson, P. Colomban, Journal of the American Ceramic Society, 84 (2001) 2007-2014.

[128] V. Birss, W. Mustain, D. Wilkinson, P. Kulesza, K. Ota, Electrode Processes Relevant to Fuel Cell Technology, The Electrochemical Society, New Jersey, USA, 2010.

[129] H.-X. Mai, L.-D. Sun, Y.-W. Zhang, R. Si, W. Feng, H.-P. Zhang, H.-C. Liu, C.-H. Yan, The Journal of Physical Chemistry B, 109 (2005) 24380-24385.

[130] G. Zhou, J. Hanson, R.J. Gorte, Applied Catalysis A: General, 335 (2008) 153-158.

[131] K.N. Rao, L. Shivlingappa, S. Mohan, Materials Science and Engineering: B, 98 (2003) 38-44.

[132] A. Khare, R. Choudhary, K. Bapna, D. Phase, S.P. Sanyal, Journal of Applied Physics, 108 (2010) 103712.

[133] V.F. Solovyov, T. Ozaki, A. Atrei, L. Wu, A. Al-Mahboob, J.T. Sadowski, X. Tong, D. Nykypanchuk, Q. Li, Scientific Reports, 4 (2014).

[134] G. Chiodelli, L. Malavasi, V. Massarotti, P. Mustarelli, E. Quartarone, Solid State Ionics, 176 (2005) 1505-1512.

[135] H. Fukuda, M. Miura, S. Sakuma, S. Nomura, Japanese Journal of Applied Physics, 37 (1998) 4158.

[136] J.-H. Yoo, S.-W. Nam, S.-K. Kang, Y.-H. Jeong, D.-H. Ko, J.-H. Ku, H.-J. Lee, Microelectronic Engineering, 56 (2001) 187-190.

[137] T. Suzuki, I. Kosacki, H.U. Anderson, Solid State Ionics, 151 (2002) 111-121.

[138] P. Miceli, S. Bensaid, N. Russo, D. Fino, Nanoscale Research Letters, 9 (2014) 1-10.

[139] S. Schorr, A. Weber, V. Honkimäki, H.-W. Schock, Thin Solid Films, 517 (2009) 2461-2464.

[140] A.A. Duarte, S.L. Filipe, L.M. Abegão, P.J. Gomes, P.A. Ribeiro, M. Raposo, Microscopy and Microanalysis, 19 (2013) 867-875.

[141] J. Hanawalt, H. Rinn, L. Frevel, Industrial & Engineering Chemistry Analytical Edition, 10 (1938) 457-512.

[142] C. Hardacre, G.M. Roe, R.M. Lambert, Surface Science, 326 (1995) 1-10.

[143] S. Eck, C. Castellarin-Cudia, S. Surnev, M. Ramsey, F. Netzer, Surface Science, 520 (2002) 173-185.

[144] R.A. Young, Crystal Research and Technology, 30 (1995) 443-584.

[145] H.P. Klug, L.E. Alexander, X-ray Diffraction Procedures, Wiley New York, 1954.

[146] W. Lohwasser, J. Gerblinger, U. Lampe, H. Meixner, Journal of Applied Physics, 75 (1994) 3991-3999.

[147] H.-I. Chen, H.-Y. Chang, Ceramics International, 31 (2005) 795-802.

[148] C. Liu, Z. Xu, Y. Zhang, J. Fu, S. Zang, Y. Zuo, Materials Letters, 139 (2015) 279-283.

[149] P. Patsalas, S. Logothetidis, L. Sygellou, S. Kennou, Physical Review B, 68 (2003) 035104.

[150] C.F. Klingshirn, Semiconductor Optics, Springer Science & Business Media, 2012.
[151] Z.C. Orel, B. Orel, Physica Status Solidi (b), 186 (1994) K33-K36.
[152] S. Garry, E. McCarthy, J.-P. Mosnier, E. McGlynn, Applied Surface Science, 257 (2011) 5159-5162.
[153] C.L. Haynes, R.P. Van Duyne, The Journal of Physical Chemistry B, 105 (2001) 5599-5611.
[154] P. Colson, C. Henrist, R. Cloots, Journal of Nanomaterials, 2013 (2013) 21.
[155] U.C. Fischer, H. Zingsheim, Journal of Vacuum Science & Technology, 19 (1981) 881-885.
[156] H. Deckman, J. Dunsmuir, Applied Physics Letters, 41 (1982) 377-379.
[157] J.C. Hulteen, R.P. Van Duyne, Journal of Vacuum Science & Technology A, 13 (1995) 1553-1558.
[158] J.C. Hulteen, D.A. Treichel, M.T. Smith, M.L. Duval, T.R. Jensen, R.P. Van Duyne, The Journal of Physical Chemistry B, 103 (1999) 3854-3863.
[159] L. Li, T. Zhai, H. Zeng, X. Fang, Y. Bando, D. Golberg, Journal of Materials Chemistry, 21 (2011) 40-56.
[160] G. Zhang, D. Wang, Chemistry–An Asian Journal, 4 (2009) 236-245.
[161] X. Ye, L. Qi, Nano Today, 6 (2011) 608-631.
[162] J. Krzak-Roś, J. Filipiak, C. Pezowicz, A. Baszczuk, M. Miller, M. Kowalski, R. Będziński, Acta of Bioengineering and Biomechanics, 11 (2009) 21-29.
[163] J.B. Lee, S.H. Kwak, H.J. Kim, Thin Solid Films, 423 (2003) 262-266.
[164] R. Bland, G. Kominiak, D. Mattox, Journal of Vacuum Science & Technology, 11 (1974) 671-674.
[165] M.L. Brongersma, Y. Cui, S. Fan, Nature materials, 13 (2014) 451-460.
[166] S.-F. Leung, Q. Zhang, F. Xiu, D. Yu, J.C. Ho, D. Li, Z. Fan, The Journal of Physical Chemistry Letters, 5 (2014) 1479-1495.

[167] M. Faisal, S.B. Khan, M.M. Rahman, A. Jamal, K. Akhtar, M. Abdullah, Journal of Materials Science & Technology, 27 (2011) 594-600.
[168] J.F. de Lima, R.F. Martins, C.R. Neri, O.A. Serra, Applied Surface Science, 255 (2009) 9006-9009.
[169] R. Chockalingam, V.R. Amarakoon, H. Giesche, Journal of the European Ceramic Society, 28 (2008) 959-963.
[170] R. Li, S. Yabe, M. Yamashita, S. Momose, S. Yoshida, S. Yin, T. Sato, Materials Chemistry and Physics, 75 (2002) 39-44.
[171] C. Ge, C. Xie, S. Cai, Materials Science and Engineering: B, 137 (2007) 53-58.
[172] S. Yabe, T. Sato, Journal of Solid State Chemistry, 171 (2003) 7-11.
[173] S. Tsunekawa, J.-T. Wang, Y. Kawazoe, A. Kasuya, Journal of Applied Physics, 94 (2003) 3654-3656.
[174] M. Montemor, R. Pinto, M. Ferreira, Electrochimica Acta, 54 (2009) 5179-5189.
[175] C. Jagadish, S.J. Pearton, Zinc Oxide Bulk, Thin Films and Nanostructures: Processing, Properties, and Applications, Elsevier, 2011.
[176] A. Torres-Huerta, M. Dominguez-Crespo, S. Brachetti-Sibaja, H. Dorantes-Rosales, M. Hernandez-Perez, J. Lois-Correa, Journal of Solid State Chemistry, 183 (2010) 2205-2217.
[177] S. Nair, A. Sasidharan, V.D. Rani, D. Menon, S. Nair, K. Manzoor, S. Raina, Journal of Materials Science: Materials in Medicine, 20 (2009) 235-241.
[178] D. Kalpana, K. Omkumar, S.S. Kumar, N. Renganathan, Electrochimica Acta, 52 (2006) 1309-1315.
[179] D. Byrne, R. Fath Allah, T. Ben, D. Gonzalez Robledo, B. Twamley, M.O. Henry, E. McGlynn, Crystal Growth & Design, 11 (2011) 5378-5386.
[180] W.L. Hughes, Z.L. Wang, Applied Physics Letters, 86 (2005) 043106.
[181] Q. Wan, Q. Li, Y. Chen, T.-H. Wang, X. He, J. Li, C. Lin, Applied Physics Letters, 84 (2004) 3654-3656.

[182] X.Y. Kong, Z.L. Wang, Applied Physics Letters, 84 (2004) 975-977.

[183] X. Wang, M. Liao, Y. Zhong, J.Y. Zheng, W. Tian, T. Zhai, C. Zhi, Y. Ma, J. Yao, Y. Bando, Advanced Materials, 24 (2012) 3421-3425.

[184] C.X. He, B.X. Lei, Y.F. Wang, C.Y. Su, Y.P. Fang, D.B. Kuang, Chemistry-A European Journal, 16 (2010) 8757-8761.

[185] J.W. Rasmussen, E. Martinez, P. Louka, D.G. Wingett, Expert Opinion on Drug Delivery, 7 (2010) 1063-1077.

[186] Z. Zhang, X. Li, C. Wang, L. Wei, Y. Liu, C. Shao, The Journal of Physical Chemistry C, 113 (2009) 19397-19403.

[187] J. Liu, S.Z. Qiao, J.S. Chen, X.W.D. Lou, X. Xing, G.Q.M. Lu, Chemical Communications, 47 (2011) 12578-12591.

[188] Z. Dong, X. Lai, J.E. Halpert, N. Yang, L. Yi, J. Zhai, D. Wang, Z. Tang, L. Jiang, Advanced Materials, 24 (2012) 1046-1049.

[189] Z.Y. Jiang, Z.X. Xie, X.H. Zhang, S.C. Lin, T. Xu, S.Y. Xie, R.B. Huang, L.S. Zheng, Advanced Materials, 16 (2004) 904-907.

[190] J. Duan, X. Huang, E. Wang, H. Ai, Nanotechnology, 17 (2006) 1786.

[191] Q. Li, E. Wang, S. Li, C. Wang, C. Tian, G. Sun, J. Gu, R. Xu, Journal of Solid State Chemistry, 182 (2009) 1149-1155.

[192] G. Shen, Y. Bando, C.-J. Lee, The Journal of Physical Chemistry B, 109 (2005) 10578-10583.

[193] C. Deng, H. Hu, G. Shao, C. Han, Materials Letters, 64 (2010) 852-855.

[194] D. Byrne, E. McGlynn, J. Cullen, M.O. Henry, Nanoscale, 3 (2011) 1675-1682.

[195] L.E. Greene, M. Law, J. Goldberger, F. Kim, J.C. Johnson, Y. Zhang, R.J. Saykally, P. Yang, Angewandte Chemie International Edition, 42 (2003) 3031-3034.

[196] L.E. Greene, M. Law, D.H. Tan, M. Montano, J. Goldberger, G. Somorjai, P. Yang, Nano Letters, 5 (2005) 1231-1236.

[197] S. Garry, Growth of Spatially Ordered ZnO Nanowire Arrays for Field Emission Applications, Ph.D. Thesis, Dublin City University, 2013. Retrieved from http://doras.dcu.ie/17857/

[198] E. McCarthy, S. Garry, D. Byrne, E. McGlynn, J.-P. Mosnier, Journal of Applied Physics, 110 (2011) 124324.

[199] J. Tauc, F. Abeles, Optical Properties of Solids, North-Holland, Amsterdam, 1972.

[200] M. Losurdo, Thin Solid Films, 455 (2004) 301-312.

[201] S.A. Ansari, M.M. Khan, M.O. Ansari, S. Kalathil, J. Lee, M.H. Cho, RSC Advances, 4 (2014) 16782-16791.

[202] T. Masui, K. Fujiwara, K.-i. Machida, G.-y. Adachi, T. Sakata, H. Mori, Chemistry of Materials, 9 (1997) 2197-2204.

[203] A.A. Ansari, M. Khan, M.N. Khan, S.A. Alrokayan, M. Alhoshan, M. Alsalhi, Journal of Semiconductors, 32 (2011) 043001.

[204] S. Phokha, S. Pinitsoontorn, P. Chirawatkul, Y. Poo-arporn, S. Maensiri, Nanoscale Research Letters, 7 (2012) 1-13.

[205] W. Shan, W. Walukiewicz, J. Ager III, K. Yu, H. Yuan, H. Xin, G. Cantwell, J. Song, Lawrence Berkeley National Laboratory, (2004).

[206] G. Lee, Y. Yamamoto, M. Kourogi, M. Ohtsu, Thin Solid Films, 386 (2001) 117-120.

[207] F. Vratny, S. Kern, F. Gugliotta, Journal of Inorganic and Nuclear Chemistry, 17 (1961) 281-285.

[208] C. Strydom, C. Van Vuuren, Journal of Thermal Analysis, 32 (1987) 157-160.

[209] S.S. Lee, H. Zhu, E.Q. Contreras, A. Prakash, H.L. Puppala, V.L. Colvin, Chemistry of Materials, 24 (2012) 424-432.

[210] J.W. Gilman, D.L. VanderHart, T. Kashiwagi, ACS Sym. Ser, 599 (1994) 161-185.

[211] D. Wang, H. Möhwald, Advanced Materials, 16 (2004) 244-247.

[212] D. Bornside, C. Macosko, L. Scriven, Journal of Applied Physics, 66 (1989) 5185-5193.

[213] B.-H. Hwang, Journal of Physics D: Applied Physics, 34 (2001) 2469.

[214] S. Tsunekawa, T. Fukuda, A. Kasuya, Journal of Applied Physics, 87 (2000) 1318-1321.

[215] L. Zhang, J. Zhang, H. Jiu, X. Zhang, M. Xu, Journal of Materials Science, 50 (2015) 5228-5237.

[216] W. Deng, D. Chen, J. Hu, L. Chen, RSC Advances, 5 (2015) 80158-80169.

[217] N.C. Strandwitz, G.D. Stucky, Chemistry of Materials, 21 (2009) 4577-4582.

[218] I. Yamaguchi, M. Watanabe, T. Shinagawa, M. Chigane, M. Inaba, A. Tasaka, M. Izaki, ACS Applied Materials & Interfaces, 1 (2009) 1070-1075.

[219] S. Ijaz, M.F. Ehsan, M.N. Ashiq, N. Karamat, T. He, Applied Surface Science, 390 (2016) 550-559.